Large Eddy Simulations of the Arctic Boundary Layer around the MOSAiC drift track

vorgelegt von
Daniela-Christin Littmann

Dissertation

zur Erlangung des akademischen Grades
"doctor rerum naturalium"
(Dr. rer. nat.)
in der Wissenschaftsdisziplin "Klimaphysik"

eingereicht an der
Mathematisch-Naturwissenschaftlichen Fakultät
Institut für Physik
der
Universität Potsdam
und dem
Alfred-Wegener-Institut Potsdam

Vorgelegt: 31. Mai 2023
Disputation: 27. November 2023

1. Gutachter: Professor Markus Rex
2. Gutachter: Professor Roel Neggers
3. Gutachter: Professor Günther Heinemann

Daniela-Christin Littmann
Large Eddy Simulations of the Arctic Boundary Layer around the MOSAiC drift track,
©31 May 2023

https://doi.org/10.25932/publishup-62437
https://nbn-resolving.org/urn:nbn:de:kobv:517-opus4-624374

Abstract

The icosahedral non-hydrostatic large eddy model (ICON-LEM) was applied around the drift track of the Multidisciplinary Observatory Study of the Arctic (MOSAiC) in 2019 and 2020. The model was set up with horizontal grid-scales between 100 m and 800 m on areas with radii of 17.5 km and 140 km. At its lateral boundaries, the model was driven by analysis data from the German Weather Service (DWD), downscaled by ICON in limited area mode (ICON-LAM) with horizontal grid-scale of 3 km.

The aim of this thesis was the investigation of the atmospheric boundary layer near the surface in the central Arctic during polar winter with a high-resolution mesoscale model. The default settings in ICON-LEM prevent the model from representing the exchange processes in the Arctic boundary layer in accordance to the MOSAiC observations. The implemented sea-ice scheme in ICON does not include a snow layer on sea-ice, which causes a too slow response of the sea-ice surface temperature to atmospheric changes. To allow the sea-ice surface to respond faster to changes in the atmosphere, the implemented sea-ice parameterization in ICON was extended with an adapted heat capacity term.

The adapted sea-ice parameterization resulted in better agreement with the MOSAiC observations. However, the sea-ice surface temperature in the model is generally lower than observed due to biases in the downwelling long-wave radiation and the lack of complex surface structures, like leads. The large eddy resolving turbulence closure yielded a better representation of the lower boundary layer under strongly stable stratification than the non-eddy-resolving turbulence closure. Furthermore, the integration of leads into the sea-ice surface reduced the overestimation of the sensible heat flux for different weather conditions.

The results of this work help to better understand boundary layer processes in the central Arctic during the polar night. High-resolving mesoscale simulations are able to represent temporally and spatially small interactions and help to further develop parameterizations also for the application in regional and global models.

Zusammenfassung

Das icosahedral non-hydrostatische large eddy model (ICON-LEM) wurde entlang des Driftweges des Multidisciplinary Observatory Study of the Arctic (MOSAiC) in 2019 und 2020 angewendet. Das Modell nutzte horizontale Gitterauflösungen zwischen 100 m und 800 m auf Gebieten mit Durchmessern von 17.5 km und 140 km. An den seitlichen Rändern wurde das Modell mit Analysedaten des Deutschen Wetterdienstes (DWD) angetrieben, welche mit ICON im limited area mode (ICON-LAM) mit einer horizontalen Auflösung von 3 km herunterskaliert wurden.

Ziel dieser Arbeit war es, die flache atmosphärische Grenzschicht in der zentralen Arktis während des polaren Winters mit einem hochauflösenden mesoskaligen Modell zu untersuchen. Die standardmäßigen Einstellungen in ICON-LEM machen es dem Modell unmöglich, die wechselwirkenden Austauschprozesse in der arktischen Grenzschicht gemäß der MOSAiC Beobachtungen abzubilden. Das implementierte Meereis-Schema in ICON beinhaltet keine Schneeschicht auf dem Meereis, was eine zu große Verzögerung der Meereisoberflächentemperatur auf atmosphärische Veränderungen bewirkt. Um die Meereisfläche schneller auf Änderungen in der Atmosphäre reagieren lassen zu können, wurde die bestehende Meereisparameterisierung in ICON um einen angepassten Wärmekapazitätsterm erweitert.

Die angepasste Meereis-Parameterisierung stimmte besser mit den MOSAiC Beobachtungen überein. Allerdings ist die Meereisoberflächentemperatur im Modell aufgrund der fehlerbehafteten einfallenden, langwelligen Strahlung und dem Fehlen komplexer Oberflächenstrukturen im Meereis generell niedriger als beobachtet. Die groß-wirbellige Turbulenz-Schliessung wird der Darstellung der unteren Grenschicht während starker stabiler Schichtung besser gerecht als die Nicht-Wirbel-auflösende Turbulenz-Schließung. Desweiteren reduzierte die Integration der Risse in der Meereisoberfläche die Abweichung der sensiblen Wärme für verschiedene Wetterzustände.

Die Ergebnisse dieser Arbeit helfen die Grenzschicht-Prozesse in der zentralen Arktis während der polaren Nacht besser zu verstehen. Hochauflösende mesoskalige Simulationen ermöglichen die Repräsentation zeitlicher und räumlicher klein-skaliger Wechselwirkungen und bestehende Parametrisierungen auch für regionale und globale Modelle weiterzuentwickeln.

Contents

List of Figures

List of Tables

1. Introduction

The Arctic is warming two to four times faster than the global average due to increasing greenhouse gas emissions (IPCC, 2021; Serreze and Barry, 2011; Shupe et al., 2021). This so-called Arctic Amplification is strongest during polar night (Cohen et al., 2014). It is related to sea-ice surface, ocean and atmosphere interactions and their complicated feedback mechanisms and results in sea-ice decline (Dethloff et al., 2019; Heinemann et al., 2021). Feedback mechanisms are internal system reactions that amplify or dampen a climate perturbation. They play an important role in determining the sensitivity of the climate system and its future state. Different processes can amplify Arctic climate changes. Poleward moisture intrusions cause convective processes leading to cloud formation, whose water-vapor cloud-radiation effects can influence the surface heat exchange in the boundary layer, and sea-ice and snow-cover albedo effects of the young sea-ice (Bresson et al., 2022; IPCC, 2021; Middlemas et al., 2020; Nicolaus et al., 2022; Pithan et al., 2018; Shupe et al., 2022; Valkonen et al., 2014). A warming surface accelerates the snow and sea-ice decline (Serreze et al., 2009; Serreze and Barry, 2011).

Our understanding of Arctic atmospheric processes is based on observations over the last decades (Shupe et al., 2022). Due to the challenges of observations in polar environments, many uncertainties remain, in particular regarding the interaction between sea-ice surface and atmosphere. Numerical simulations provide the possibility of closing the gap between spatially and temporally separated measurements. The Multidisciplinary drifting Observatory for the Study of Arctic Climate (MOSAiC) was operational from October 2019 to September 2020 within the central Arctic (Shupe et al., 2022). During this one year comprehensive and sophisticated data sets were gathered on an area characteristic to the size of a model grid-box to determine the annual cycle of interactions between sea ice, ocean, atmosphere and biosphere through a variety of physical and biochemical processes (e.g Maturilli et al., 2021; Nicolaus et al., 2022; Rabe et al., 2022; Shupe et al., 2022).

Which interacting processes are resolved is determined by the choice of turbulence closure and the grid volume of the model. Processes that cannot be resolved are considered to be sub-grid scale processes and have to be parameterized in atmospheric models for regional scales, such as numerical weather prediction models (NWPs). However, models often use parametrizations of the sub-grid scale processes, which were developed on the basis of measurements in mid-latitudes where different atmospheric surface conditions prevail (Heinemann et al., 2021; Lüpkes et al., 2008b; Rinke et al., 2006; Valkonen et al., 2014). In the mid-latitudes convective processes occur more often, whereas over closed sea ice inner Arctic boundary layer is often stably stratified. This holds especially for the polar night when near the surface even strongly stable conditions occur with weak or almost no turbulent mixing. These days, the central Arctic ocean is mostly covered by first-year sea-ice (Heinemann et al., 2021; Nicolaus et al., 2022).

The relatively young sea-ice has a much shallower vertical depth than its perennial counterpart and is much less compact. Already small changes in the sea-ice fraction caused by cracks and leads have a strong impact on the thermodynamic profiles and especially on the near-surface temperature (Lüpkes et al., 2008a). Those leads amplify turbulent heat and moisture exchange in the Arctic atmospheric boundary layer (Michaelis and Lüpkes, 2022). The sea-ice surface temperature is affected by the net radiation fluxes of the atmosphere and is influencing the heat fluxes at the sea-ice surface. However, in atmospheric models the sea ice is traditionally described just by the surface boundary condition (Hunke et al., 2020) that does not include a sea ice layer with an own vertical temperature distribution. Thus, model calculations of, e.g., surface temperature, turbulent heat fluxes, and cloud formation tend to be biased. For this reason, a high-resolving model is needed to study small-scale processes in the Arctic boundary layer.

Large eddy simulations (LES) use high-resolution horizontal gird-scales and therefore require fewer parametrizations than other typical NWPs, e.g. such as for convection, and resolve a larger part of the turbulent transport. How much energy supporting turbulence is resolved depends on the grid volume of the model. Due to their spatial and temporal resolution, results of LES are expected to agree better with reality than results from coarse resolution models. Many LES studies have been conducted to investigate the impact of large scale advection on the Arctic mixed boundary layer (e.g. Dimitrelos et al., 2020; Gryschka et al., 2014; Neggers et al., 2019; Sotiropoulou et al., 2020; Weinbrecht and Raasch, 2001). For example, the vertical transport between two layer mixed-phase clouds has been studied in the context of strong moisture intrusions in polar summer (e.g. Egerer et al., 2021; Zhang et al., 2022) and the effect of entrained aerosol concentrations on the dynamic of stratocumulus clouds (Bulatovic et al., 2022; Sotiropoulou et al., 2020). During the polar winter, strong large scale wind speeds due to high pressure gradients between the poles and the mid-latitudes have the potential to erode shallow clouds (Neggers et al., 2019), (Zhang et al., 2022). Another study showed that LES can be a useful tool to investigate surface shear stress and surface fluxes, and improve the model performance under neutral to stable conditions (Maronga et al., 2020). More recently, LES experiments have been performed in the context of the MOSAiC expedition to study convection over leads (Schnierstein et al., 2021), the impact of the Polarstern vessel on the measurement sites (Rauterkus and Maronga, 2023), and the vertical exchange between the atmosphere and the sea ice surface under extreme stability (van der Linden and Ansorge, 2022). But also general circulation models (GCMs) start to include the LES physics package (Dipankar et al., 2015; Mirocha et al., 2010). This setup combines the capability of high-resolving small-scale interactions in the atmospheric boundary layer (ABL) on a spatially broader heterogeneous domain using forcing from global forecasts.

The icosahedral non-hydrostatic large eddy model used in this thesis was developed to model shallow convection using an adequate turbulence parametrization (ICON-LEM, Dipankar et al. (2015); Heinze et al. (2017)). Because of its complexity, ICON-LEM cannot be considered as a classical large eddy model. ICON-LEM is a high-resolving mesoscale model with horizontal grid-scales of several hundreds of meters and domain sizes in the kilometer range. The model is driven at the lateral boundaries by global forecasts. The common feature with a classical large eddy model is the turbulence scheme by Smagorinsky (1963), where large eddies are resolved according to the grid-box volume. The application of ICON-LEM in Arctic research is still quite new, with only two other studies carried out in the Arctic so far by Schemann et al. (2020) and Kiszler et al. (2023) with focus on mixed-phase cloud processes around the complex terrain around Ny-Ålesund.

In this thesis, the model is applied for the first time over sea-ice in the central Arctic. The aim of this study is to investigate the strength and weaknesses of the model and, if necessary, to adapt the implemented parameterizations to Arctic conditions and to evaluate the model performance. An overview of the closure problem and the methods used in the parameterizations to close them is described in Chapter 3. Two turbulence parameterizations are used to quantify their difference in presenting near-surface exchange processes. The general model setup of ICON and the detailed description of the parameterizations used in this study are outlined in the model description of Chapter 4. The first examined weather period is a clear sky winter night in February 2020, with a very calm wind situation, low temperatures, weak turbulence and a very stable stratified atmosphere. The second weather condition is a heavy storm series during the middle of November 2019, with very strong wind velocities and strong turbulent mixing. The applied methods and used model setup are explained in Chapter 5. The simulation results of the different model runs are compared to the comprehensive MOSAiC data. The description of the used observational data is treated in Chapter 6 and the model evaluation of the different experiments are presented in Chapter 7. Finally, a discussion of the results and a final summary is addressed in Chapter 8.

2. Boundary Layers Types of the Atmosphere

This chapter is a brief summary and is based on (Stull, 1988). It serves for understanding the different structures of the atmospheric boundary layer.

The Earth's atmosphere is divided into several layers, each characterized by different conditions. The lowest layer, known as the troposphere, extends about 12 km above the Earth's surface. The part within the troposphere that is directly influenced by the presence of the Earth's surface is called the Planetary Boundary Layer (PBL) (Stull, 1988). The surface absorbs solar radiation and then emits long-wave radiation into the PBL. The response to the surface forcing is manifested in turbulence and vertical transport of e.g. momentum, heat, moisture and tracers from near the surface into the upper atmosphere. Over the ocean, the PBL changes relatively slowly due to the large heat capacity of the ocean, resulting in a gradual response to surface temperature variations. Over land, the boundary layer has a well-defined structure that is influenced by several driving factors, including surface properties, wind conditions, atmospheric stability, and others (Stull, 1988).

The boundary layers are usually classified into three types on the basis of their different characteristics and vertical structure. This includes the Convective Boundary Layer (CBL), the Neutral Boundary Layer (NBL), and the Stable Boundary Layer (SBL). Although each type has its own characteristics, they all have a surface layer at the bottom of the boundary layer. This layer is characterized by turbulence and shear processes, just before molecular dissipation becomes significant in the lowest few centimeters above the surface. In the following subsections, these three types are briefly described.

2.1 The Convective Boundary Layer (CBL)

The CBL is characterized by heat transfer from the underlying surface, such as absorption of solar radiation or by advection of cold air over a warm surface (Stull, 1988). On cloudless days, the heating of the ground by the sun leads to strong heat fluxes, resulting in vigorous mixing throughout the CBL. As a result, large eddies can develop, reaching down to depths of the CBL.

The surface layer within the CBL is characterized by the formation of thermals originating from a heated surface. With increasing height, the virtual temperature and humidity decrease, while the wind speed increases approximately logarithmically. Intense convective mixing in the overlying layer introduces high momentum flux into the surface layer, where surface drag acts as a sink (Stull, 1988).

Above the surface layer is the mixing layer, which is influenced by the buoyancy-driven heat and moisture exchange under statically unstable conditions within the CBL. In this

layer, the potential temperature and humidity change minimally with height. Due to radiative heating, the surface has the warmest temperature, with a slight temperature increase in the entrainment zone. The moisture content decreases slightly with height.
Within the entrainment zone, the air becomes statically stable and is characterized by inflows of air from the atmosphere above and overshooting of thermals from below. Here the wind speed and potential temperature increase sharply, while the moisture content decreases. The CBL reaches depths of up to 2000 m.

2.2 The Neutral Boundary Layer (NBL)

The NBL is often used as a reference state for studying the boundary layer dynamics, although in reality it rarely exist. However, it can be observed in the form of a residual layer that remains in the upper atmosphere after sunset, where remnants of the mixed layer persist and turbulence is almost isotropic throughout the layer. The NBL occurs typically during periods of increased cloud cover and strong winds (Stull, 1988).
In cases where temperature difference between the surface and the upper air is small, the boundary layer can be considered to be approximately neutrally stratified. Within the NBL, turbulent heat and moisture exchange at the surface is relatively limited, and buoyancy effects are close to zero. Convection does not occur within the NBL, and the layer is predominantly influenced by adiabatic mixing processes. As a result, the potential temperature remains relatively constant throughout the NBL. Therefore, while there may be small-scale temperature variations within the NBL, the overall temperature profile does not show a significant warming or cooling trend from the surface to the upper atmospheric layer. Turbulence within the NBL is only generated by wind shear and the NBL can reach depths of up to 1000 m.

2.3 The Stable Boundary Layer (SBL)

The SBL forms when the surface temperature is colder than the air aloft, typically due to long-wave cooling at the surface or due to advection of warm air over cold surface. In the SBL, the air near the ground is denser than the air above, leading to the suppression of vertical exchange processes. The stability of the SBL inhibits turbulent mixing, and turbulence can only be sustained by TKE production by wind shear. Over land, the SBL develops during nighttime (Stull, 1988).
Due to the sporadic occurrence of turbulence, the SBL can decouple the upper atmospheric layers from surface forcing, making it difficult to provide a consistent description of its characteristics (Stull, 1988). The depth of the SBL typically ranges from about 100 m to 500 m.
In the surface layer near the ground, the strongest stability can be observed, and the stability gradually decreases towards neutrality with increasing height. When the temperature starts to increase with height under strong stability conditions, it is called a temperature inversion (Stull, 1988).
The SBL is influenced by various factors such as topography, mesoscale and synoptic forcing, which can affect wind speed and direction. Close to the surface, winds may be calm, but generally increase with height. The moisture distribution in the SBL can be complex, with the potential for evaporation or condensation near the surface. Horizontal advection can introduce pollutants and other tracers into the SBL. Turbulence is rare and

gradually decreases with height. Vertical transport is suppressed, but buoyant oscillations can occur in the form of gravity waves.
At a certain height above the surface, turbulence in the SBL is dominated by shear and stability rather than the surface forcing. This transition can lead to decoupling between the near-surface atmospheric layer and the overall flow regime.

In the Arctic region, the atmosphere is almost permanently stably stratified throughout the year (e.g. Mauritsen (2007)). Due to the low solar energy received, the surface of the sea ice is frozen and warm air masses from the mid-latitudes move into the Arctic region, driven by low pressure systems (Mauritsen, 2007). Radiative processes play a predominant role in the formation of the SBL over sea ice and ice sheets, but also warm air masses advected over the cold air at the surface, causing a temperature inversion.

3. The Closure problem

Numerical (climate) models are using a large number of parameterizations to reproduce the reality into a simple form. To clarify the differences between the turbulence schemes used in this study, but also to point out the limitations of parameterizations in general, this chapter provides a theoretical background of turbulent parameterizations as an example. This is to serve as an introduction to the following model description in Section 4.

The content of this chapter is a brief summary and is based on (Stull, 1988) and (Wilcox, 2006). It serves for understanding the parametrizations used in this study.

The motion of a fluid is described by physical properties, such as the the velocity, pressure, temperature and density. Depending on the physical phenomena that occurs, e.g. mass transport or turbulence, these properties can vary considerably. In the 19th century, Claude-Louis Navier and George Gabriel Stokes independently developed a set of differential equations describing the motion of a viscous fluid, the so called Navier-Stokes equations. Depending on the physical problem and technical computer capability, the Navier-Stokes equations can be derived for compressible or incompressible flows. In the case of the latter, the change in density with change in pressure is assumed to be negligible, while for compressible flows the density is not a constant. Considering this study, we will limit ourselves only to the description of the compressible Navier-Stokes equations. The equation system can be derived through Newtons second axiom and represents an extension of the compressible Euler equation system including the conservation of mass, momentum and energy and an additional added term for viscosity (Zdunkowski and Bott, 2003). Altogether the Navier-Stokes equations form a full system of equations with five differential equations, including five unknowns with three velocity components, pressure, density and temperature. In the solution of the Navier-Stokes equations, turbulent transport terms appear, which remains one of the greatest unsolved problems in physics (Stull, 1988). Considering that the system needs to be energetic conservative, it can be assumed that small fluctuations are averaged out in time. Regarding this, all instantaneous variables are represented as a sum of a mean and turbulent contribution. In the Navier-Stokes equations the parts that are affected by the averaging are fluctuations in the velocity and pressure components. For simplicity reasons, the following description of temporal averaging is only addressed as the mean.
In 1965, Favre introduced a general **density-weighted averaging** method that separates fluctuations from the mean flow. The unfiltered velocity component u_i is split into the density-weighted velocity component $\hat{u}_i$ and the perturbation component v_i''

$$\hat{v}_i = \frac{\overline{\rho v_i}}{\overline{\rho}}, v_i'' = v_i - \hat{v}_i. \tag{3.0.1}$$

The overbar on $\overline{\rho}$ correspondents to the classical Reynolds-averaging (Appendix 8). For eq. 3.0.1 also follows the relationship

$$\overline{\rho}\hat{v}_i = \overline{\rho v_i} = \overline{\rho} v_i + \overline{\rho' v_i'}. \tag{3.0.2}$$

Consequently, the Favre-averaged perturbation vanishes

$$\overline{\rho v_i''} = 0. \tag{3.0.3}$$

However, when applying the Reynolds-averaging on the perturbation v_i'', it does not disappear

$$\overline{v_i''} = -\frac{\overline{\rho' v_i'}}{\overline{\rho}} \neq 0. \tag{3.0.4}$$

Even though the Favre-averaging eliminates the density fluctuations from the general equations, they are not disappearing for turbulence. The advantage of the Favre-averaging method compared to the Reynolds-averaging method is that many correlation terms vanish in the convection term of the Navier-Stokes equation:

$$\overline{\rho v_i v_j} = \overline{\rho}\hat{v}_i\hat{v}_j + \overline{\rho v_i'' v_j''}. \tag{3.0.5}$$

To close the turbulent equation system with more unknowns than equations, approximations are needed for the unknown. The closures are denoted after the solution of their prognostic equations of highest order. E.g. a first-order closure solves first-order momentum equations and parametrizes second-order moments (Stull, 1988). The higher the order of the equation system the more accurate the solution. An overview for the described closure orders is summarized in Table 3.1. The turbulent kinetic energy $\overline{e}$ is a measure of the intensity of turbulence through the atmospheric boundary layer (Stull, 1988). It is the sum of velocity variances

Order	**Prognostic equation**	**Approximation equation**	**No. of equations**	**Unknown**
1.	$\overline{v_i}$	$\overline{v_i' v_j'}$	3	6
2.	$\overline{v_i' v_j'}$	$\overline{v_i' v_j' v_k'}$	6	10
3.	$\overline{v_i' v_j' v_k'}$	$\overline{v_i' v_j' v_k' v_l'}$	10	15

Table 3.1: Simplified representation for unknown momentum of different orders to describe the closure problem in turbulent flow. Example after Stull (1988) and Foken and Napo (2008).

$$\overline{e} = \frac{1}{2}(\overline{u'^2} + \overline{v'^2} + \overline{w'^2}) = \frac{1}{2}\overline{v_i'^2} \tag{3.0.6}$$

The TKE budget is derived by multiplying the momentum equation by a fluctuating velocity component with conducting the Favre averaging (e.g. Stull (1988)). After Wilcox (2006) the Favre-averaged TKE budget follows

$$\begin{aligned}\overline{\rho}\frac{\partial \overline{e}}{\partial t} + \overline{\rho}\hat{v}_j\frac{\partial \overline{e}}{\partial x_j} &= \overline{\rho}\tau_{ij}\frac{\partial \hat{v}_i}{\partial x_j} - \overline{\rho}\epsilon \\ &+ \frac{\partial}{\partial x_j}[\overline{t_{ji} v_i''} - \overline{\rho v_j'' e} - \overline{p' v_j''}] \\ &+ v_i''\frac{\partial \hat{p}}{\partial x_i} + \overline{p'\frac{\partial v_i''}{\partial x_i}}\end{aligned} \tag{3.0.7}$$

$\hat{v}$ is the mean wind speed, p the pressure, and ρ the density of air, τ_{ij} is the Favre-averaged stress tensor, t_{ji} the stress strain rate, and ϵ the dissipation. On the left hand side are the tendency and advection with the mean flow. On the right hand side follows the rate of turbulence production, the dissipation rate, the molecular diffusion, the turbulent transport, the pressure diffusion, the pressure work, and the pressure correlation.
The contribution of molecular diffusion is comparably small. For this reason, this term often is neglected in climate models. The production term and the pressure diffusion transform mean kinetic energy to turbulent kinetic energy. On the other hand, the dissipation rate transfers turbulent kinetic energy to internal energy. As these terms only redirect energy, they must cancel in the overall energy-conservation equation (Wilcox, 2006). Compared to TKE budget equation for incompressible fluids, two additional pressure correlations are derived in eq. 3.0.7 due to density fluctuations, the pressure work $\overline{v}_i''\partial_i p$ and the pressure dilatation $p'\partial_i v_i''$. The number of unknowns in the equation system depends on the order of the derived equation. Those unknown nonlinear tensors need to be parametrizised in order to close the problem. An appropriate parameterization contains the physical properties of the approximated quantity (Stull, 1988).

4. Model description

This chapter provides a basic description of the ICOsahedral Non-hydrostatic (ICON) model and the used setup. A license of the actual model version can be received from the German Weather Service (DWD) at `contacticon@dwd.de`, or from the Max Planck Institute for Meteorology (MPI-M) via `https://code.mpimet.mpg.de/projects/iconpublic/wiki/How_to_obtain_the_model_code`. Most of the content is based on the Prill et al. (2020). The actual tutorial can be found in the following path of the model version: `/docs/icon_tutorial`, or online via `https://www.dwd.de/DE/leistungen/nwv_icon_tutorial/pdf_einzelbaende/icon_tutorial2020.html`.

ICON has been developed in collaboration between the DWD and the MPI-M (Zängl et al., 2015). It is a unified modeling system used for climate prediction and numerical weather prediction between coarse global (Giorgetta et al., 2018) and high-resolution local scales (Dipankar et al., 2015). While the numerical components for global and mesoscale simulations were implemented from the beginning, the large eddy package was deployed during the High Definition Clouds and Precipitation for advancing Climate Prediction (HP(CP)^2) project that started in 2015 to model shallow convection with an adequate turbulence parametrization (see, e.g. Dipankar et al., 2015; Heinze et al., 2017). The high-performance of this model is realized by a parallel computation. ICON possesses a fully compressible non-hydrostatic core. This is due to the fact that the total air density ρ is one of the prognostic variables, while the pressure p is diagnosed and needed as an input variable for the parameterizations (Prill et al., 2020; Zängl et al., 2015). A detailed description of the dynamical core can be found in Zängl et al. (2015).

This chapter is structured as follows: The development of the ICON model during the recent years are described in Section 4.1. The governing equations are described in Section 4.2, followed by a specification of the three dimensional grid used in ICON in Section 4.3 and Section 4.4. The necessary boundary conditions are described in section 4.5. The important parametrizations are addressed in Section 4.6, with insights into the turbulence schemes in Section 4.6.3 and Section 4.6.4, as well as the sea ice scheme in Section 4.6.5.

4.1 Applied model versions

The ICON license used in this work was purchased from DWD. The global and regional simulations are basically run in the numerical weather prediction mode (NWP). Since the main focus from DWD remain on weather forecasts in Germany, the pre-configured settings of the parameters in the different physical modules have been mainly adapted to the European environment.

Climate models are in a permanent state of development. However, when the ICON license was purchased by the Alfred-Wegener-Institute (AWI), the model was still in an early stage of development compared to other well established climate models.

Major changes have been conducted on ICON during the recent years. In 14 April 2021, the model code was upgraded to model version 2.6.2-nwp2, which is described in the notification of changes by Zängl (2021a). This version included several crucial bug-fixes. In 8 September 2021, ICON was upgraded further to model version 2.6.3-nwp1, which is described in the notification of changes by Zängl (2021b) and is the current version used for the study. In the following paragraphs, the most important changes will be briefly summarized based on the notifications of changes. A detailed description of all the changes is beyond the scope of this work and should be taken from the referenced documents.

In model version 2.6.2-nwp2, an important change concerned the radiation scheme switch from the RRTM by Mlawer et al. (1997) scheme to ecRad by Hogan and Bozzo (2018); Rieger et al. (2019). Among other things, the latter included a modification of the solving methods, which improved the representation of low-level clouds. Another major bug-fix was related to a correction in the model physics. The turbulence scheme was originally developed for a coupling at constant pressure. The coupling of the turbulence scheme was missing the adjustment at constant density, i.e. the factor $c_\mathrm{p}/c_\mathrm{v}(= 1.4)$ in the conversion of the turbulent heat flux divergence into the resulting temperature difference (Zängl, 2021a). This caused major discrepancies in the energy budget of the system. Further fixes included for example, the replacement of an empirical data collection on long-wave radiation emissivity at the surfaces by a climatological data collection based on satellite images (see CAMEL from Feltz et al. (2018)). As a result, several surface-related parameters had to be adjusted, such as for the sea ice. Several more adjustments and parameter tunings were carried out throughout the NWP namelists.

In model version 2.6.3-nwp1, more namelist parameters were tuned in the model, that were based on the changes that were done on the previous model version 2.6.2-nwp2. Additionally, the numerical equations of the prognostic variables in the dynamical core were adapted for the vertical nest interface so that they were consistent with the vertical solution methods (Zängl, 2021b). This affected all model simulations with reduced vertical nests, such as ICON-LAM and ICON-LEM.

The configuration of ICON-LEM presented some difficulties, as several modules were not updated for over a decade. Therefore, some of the routines were adjusted to maintain consistency. For example, when calling the GME Surface-Transfer scheme (GME STS), which is coupled to the turbulence scheme, a pointer for the storage of the tile-based momentum fluxes has been replaced by a pointer that stores the mean values of the momentum fluxes. The GME STS does not support the tile approach, i.e. the appropriate calculation of the averaged surface fluxes of a grid cell, according to its sub-grid-scale topography (see Prill et al. (2020) for more details about the tile approach). Therefore, a pointer directing to the tile-based storage was obsolete.

In particular, the application of ICON-LEM in the central Arctic entailed many additional challenges. The climatic conditions of the Arctic are completely different compared to the mid-latitudes, e.g. in the landscape, the seasons and the weather conditions. Thus, several parameters working for the mid-latitude (land) area had to be adjusted for the Arctic conditions. This concerned setup configurations of the internal interpolation methods, the non-hydrostatic core, the turbulence scheme, the vertical level specification and the tracer transport.

4.2 Governing equations

The heterogeneous flow regime in ICON is described by the Navier-Stokes equations that consists the three time-dependent conservation equations for momentum, the time-dependent continuity equation of mass and the time-dependent conservation equation of energy. The prognostic variables are suggested by Gassmann and Herzog (2008) and describe an atmosphere consisting of dry air and water in three phases (gaseous, liquid and solid). To avoid that interpolated values of the density ρ enter the solution of the continuity equation in the dynamical core, a temporal average of the mass flux over the dynamic substeps $\langle F_m \rangle = \langle \rho v_n \rangle$ is used (Prill et al., 2020). In order to solve the compressible non-hydrostatic equation system, the hydrostatic flow regime ϕ gets separated into a density weighted mean flow $\hat{\phi}$ and a perturbation ϕ''. Thus, it follows

$$\hat{\phi} = \frac{\overline{\rho\phi}}{\overline{\rho}}, \phi'' = \phi - \hat{\phi}. \tag{4.2.1}$$

The density weighted averaging (Favre, 1969; Hesselberg, 1926) is applied on the barycentric mean $\hat{\phi}$ and the overbar on $\overline{\phi}$ correspondents the classical Reynolds averaging (as described in Chapter 3).

The equation system is solved by a shallow-atmosphere approximation (Gassmann and Herzog, 2008). For reasons of simplicity, ICON solves the prognostic equation for the virtual potential temperature $\hat{\theta}_\mathrm{v}$ instead of the virtual Temperature $\hat{T}_\mathrm{v}$ and pressure $\hat{p}$:

$$\hat{\theta}_v = \hat{T}_\mathrm{v} \left(\frac{p_0}{\overline{p}}\right)^{\frac{R_\mathrm{d}}{c_{p\mathrm{d}}}} = \frac{\hat{T}_\mathrm{v}}{\overline{\pi}}. \tag{4.2.2}$$

$p_0 = 1000hPa$ is the reference pressure, R_d is the ideal gas constant of dry air, $c_{p\mathrm{d}}$ is the isobaric specific heat capacity of dry air and $\overline{\pi}$ is the Exner function.

The prognostic variables are the horizontal velocity component normal to the triangle v_n, the vertical wind component $\hat{w}$, the virtual potential temperature $\hat{\theta}_\mathrm{v}$ and the total density of air $\overline{\rho}$, including liquid and solid hydrometers. The Lamb transformation is applied on the advection term in the momentum equation $v \cdot \nabla v = w \times v + \nabla 1/2v^2$. The budget equation set reads following (Dipankar et al., 2015; Zängl et al., 2015)

$$\frac{\partial \hat{v}_\mathrm{n}}{\partial t} + \frac{\partial \hat{v}_\mathrm{n}^2 \hat{v}_\mathrm{t}^2/2}{\partial n} - (\overline{\xi} + f)\hat{v}_\mathrm{t} + \hat{w}\frac{\partial \hat{v}_\mathrm{n}}{\partial z} = -c_{p\mathrm{d}}\hat{\theta}_\mathrm{v}\frac{\partial \overline{\pi}}{\partial n} - Q(v_n), \tag{4.2.3}$$

$$\frac{\partial \hat{w}}{\partial t} + \mathbf{\hat{v}_h} \cdot \nabla_h \hat{w} + \hat{w}\frac{\partial \hat{w}}{\partial z} = -c_{pd}\hat{\theta}_\mathrm{v}\frac{\partial \overline{\pi}}{\partial z} - g + Q(w), \tag{4.2.4}$$

$$\frac{\partial \overline{\rho}\hat{\theta}_v}{\partial t} + \nabla \cdot (\mathbf{\hat{v}}\overline{\rho}\hat{\theta}_v) = Q(\overline{\rho}\hat{\theta}_v), \tag{4.2.5}$$

$$\frac{\partial \overline{\rho}\hat{q}_i}{\partial t} + \nabla \cdot (\mathbf{\hat{v}}\overline{\rho}\hat{q}_i) = Q(\overline{\rho}\hat{q}_i), \tag{4.2.6}$$

$$\frac{\partial \overline{\rho}}{\partial t} + \nabla \cdot (\mathbf{\hat{v}}\overline{\rho}) = 0, \tag{4.2.7}$$

The budget equations include the tangential velocity component $\hat{v}_\mathrm{t}$, vertical vorticity $\overline{\xi}$, the Coriolis parameter f, the gravitational acceleration g, the tracer for specific humidity and liquid water $\hat{q}_i \in (\hat{q}_v, \hat{q}_l)$, the source term for horizontal momentum $Q(v_n)$, the source term for vertical momentum $Q(w)$ and the diabatic heat-source terms for the density potential temperature $Q(\overline{\rho}\hat{\theta}_v)$ and for the tracers $Q(\overline{\rho}\hat{q}_i)$. $\frac{\hat{v}_\mathrm{n}^2+\hat{v}_\mathrm{t}^2}{2}$ signifies the horizontal part of the kinetic energy. c_{pd} and c_{vd} are the specific heat capacity for dry air at constant pressure and volume, respectively. The terms on the left hand side of the momentum equations describe the convection terms, the terms on the right hand side describe the diffusion terms. A full description of the implemented equation system used in the model is beyond the scope here and can be found in the work of Gassmann (2013); Gassmann and Herzog (2008); Zängl et al. (2015).

4.3 Horizontal grid

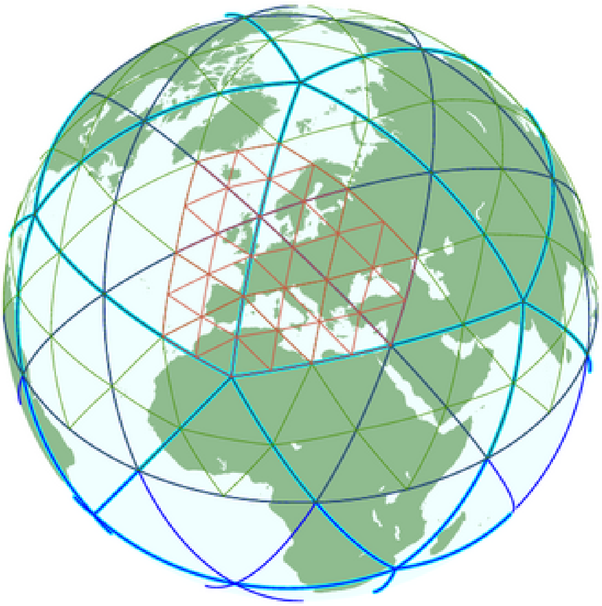

Figure 4.1: Illustration of the grid construction procedure. The original spherical icosahedron is shown in blue, denoted as R1B00 following the nomenclature described in the text. In this example, the initial division (n=2; dark blue), followed by one edge bisection (k=1) yields an R2B01 grid (red lines), (Prill et al., 2020).

One of the main features of the ICON model is the icosahedral grid that covers the globe nearly homogeneously, allowing for a more uniform grid (Giorgetta et al., 2018). These triangular grid cells avoid instabilities as in classical longitude-latitude grids (*pole-problem*) (Prill et al., 2020). The grid of the icosahedron is obtained by the Delaunay-Voronoi triangulation, where for a set of vertices three independent points get connected with straight-line edges that do not cross each other and form a triangle, see Figure 4.1. The original icosahedron is projected onto the sphere of the globe, where great circle arcs form the edges of the basic triangles (Prill et al., 2020). It is composed of 20 equilateral spherical triangles (light blue lines) that are refined by initial root division (bisecting each triangle) into n equal sections per edge (Rn) (blue lines) (Prill et al., 2020). Connecting the new set of vertices with straight-line edges yields n^2 spherical triangles within the original triangle (dark blue lines in Figure 4.1), followed by k recursive edge bisection steps (Bk) (red lines in Figure 4.1) (Prill et al., 2020). This procedure of grid refinement forming the grid type **R**n**B**k is suitable for very high horizontal grid resolutions. The total number of cells n_c is given by Zängl et al. (2015):

$$n_\mathrm{c} = 20n^2 4^k. \tag{4.3.1}$$

For the number of edges n_e and the number of vertices n_v follows

$$n_\mathrm{e} = 30n^2 4^k, n_\mathrm{v} = 10n^2 4^k + 2. \tag{4.3.2}$$

The effective grid resolution is calculated by the Earth surface S_Earth and the Earth radius R_Earth, respectively (Prill et al., 2020; Zängl et al., 2015)

$$\overline{\Delta x} = \sqrt{\frac{S_\mathrm{Earth}}{n_\mathrm{c}}} = \sqrt{\frac{4R^2_\mathrm{Earth}\pi}{n_\mathrm{c}}} = \frac{R_\mathrm{Earth}}{n2^k}\sqrt{\frac{\pi}{5}} \approx \frac{5050}{n2^k}[\mathrm{km}]. \tag{4.3.3}$$

The resolution refers to the square root of the mean cell area in the icosahedral grid of ICON (Heinze et al., 2017). In case of a one-way or two-way online nesting simulation mode, the child grid domain must fulfill the bisection of the original parent grid so that the gained smaller triangular grid of the child domain is inclosed into the triangular grid structure of the parent grid. The horizontal grid information is loaded as an input parameter, which is stored in the grid files, see also Section 2.1.1. of the Prill et al. (2020). Furthermore, each horizontal grid comes along with an additional file for the external parameters. These parameter include the aggregated topography for the target grid. The two available datasets available for the orography in ICON are the Global Land One-Kilometer Base Elevation (GLOBE) (Hastings and Dunbar, 1998), with a grid resolution of 1 km, and the Advanced Spaceborne Thermal Emission and Reflection Radiometer (ASTER) (Abrams, 2000; Abrams et al., 2015), with a grid resolution of 15 m. Horizontal grids with grid spacings below 3 km and with domain positions within the range of 60° S to 60° N are provided with the highly resolved, non-global topography from ASTER, while the other horizontal grids are provided with the topography from GLOBAL. Hence, the external parameter in ICON-LEM for the central Arctic include the aggregated topography from GLOBE.

4.4 Vertical grid

As a non-hydrostatic model, a vertical coordinate structure based on pressure levels makes no sense (Prill et al., 2020). Instead, the vertical grid structure in ICON is defined via height-based coordinates, where the influence of the surface coordinates decays linearly with height and surface features are removed rapidly (Leuenberger et al., 2010; Schär et al., 2002). Switches to control this configuration can be found in the namelist `sleve_nml`. A vertical stretching is applied on the vertical levels, which is schematically shown in Figure 4.2 for the lowermost vertical levels. The smallest vertical depth lies between bottom and the lowermost atmospheric half level and the thickest vertical depth is between model top and the next lower half level. The namelist parameter to influence the stretching is called `stretch_fac`. Each level on the vertical grid contains the horizontal grid (Section 4.3) with arranged spherical triangles with respect to the tangent plane on the ground. The total number of those vertical layers for each grid domain `num_lev` has to be configured in the namelist `run_nml`. The model top height `top_height` is customizable, but has a limit at 75 km. The vertical grid is divided into full and half levels (Figure 4.2). The first half level starts at the model top of the atmosphere and ends with the last half level `num_lev+1` at the bottom layer. The prognostic variables are located at the cell center or the cell edges (Prill et al., 2020). As is indicated in Figure 4.2, a Lorentz-type staggering is used in the vertical, so that the normal horizontal velocity v_n, the virtual potential temperature θ_v and the density ρ are defined at full levels, whereas the vertical velocity w is defined at half levels (Prill et al., 2020).

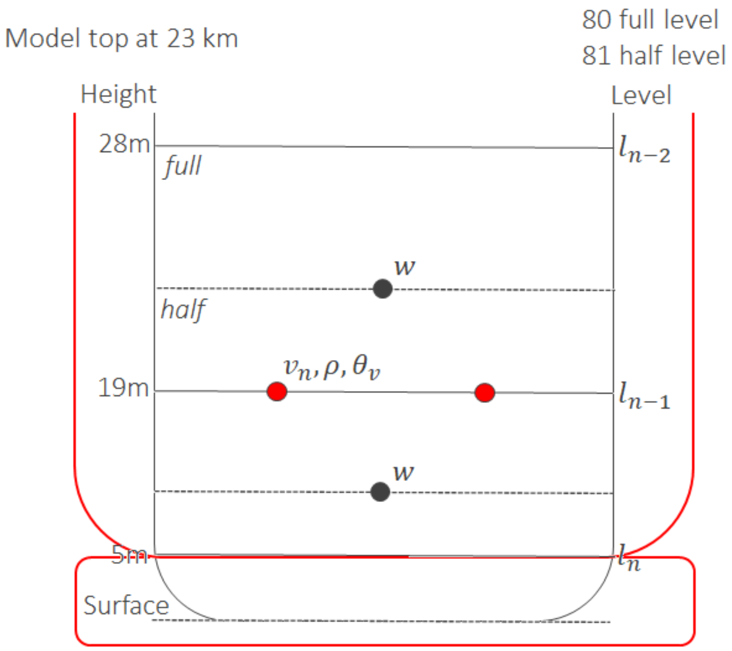

Figure 4.2: Schematic illustration of the vertical grid used in this setup for ICON-LEM. The half levels start at the model top at 23 km and end at the surface with 81 levels in total. In between are the 80 full levels. The lowermost full levels is at 5 m height.

4.5 Lateral boundaries

ICON Global analysis and weather forecast data for the area at 50° N from DWD were specifically provided to the Alfred-Wegener-Institut (AWI) and subsequently stored locally (e.g. Prill et al., 2020). The DWD itself deletes the files automatically after 18 months. ICON Global has a horizontal resolution of approximately 13 km and 90 vertical model levels up to a height of 75 km (Prill et al., 2020). Those forecasts constitute the initial and the lateral boundary data (forcing) for ICON in Limited-Area Mode (ICON-LAM), which has a horizontal resolution of approximately 3 km and 70 vertical levels with a model top at 23 km. The ICON-LAM simulations are forced by 3-hourly global ICON forecast data, including additional SIC and SST updates (Bresson et al., 2022). ICON-LAM then provides the forcing data to the parent grid used in ICON-LEM. In a preliminary stage, the forcing data needs to be remapped on the target parent grid. This is realized via DWD ICON Tools by interpolating the forcing variables onto the target grid through radial basis functions (RBF). The initial-file for the lower boundary conditions is read-in only once at the beginning of the simulation period, whereas the lateral boundaries are updated at hourly time intervals. In nested simulations, the ICON-LEM parent domain passes the prognostic variables over to the overlapping grid points at the boundaries of the child domain. Once the parent domain has been updated within a timestep Δt, the tendencies of the prognostic variables for the cells and edges are calculated for that timestep and downscaled to the cells and edges of the child's boundary zone (Prill et al., 2020). Since the timestep of the child domain is half of the parent domain, the child domain needs two timesteps Δt_c to be updated completely (Prill et al., 2020). In the domains, the two-dimensional gradients of the cell centers are reconstructed by RBFs from the gradients of the surrounding edge mid-points. When the tendencies of the prognostic variables are transferred from the parent domain edge grid points to the boundary zone of the child domain, a distinction is made between the inner and outer child edge grid points. At the grid points that overlap with the parent edge, the mass flow must be the same for the child and parent domain. This procedure is repeated until the lateral boundary condition of the last child domain is interpolated. The grid spacing between the parent domain and the child domain is fixed by a factor of 2 (Prill et al., 2020). I.e. the parent triangle inherits 4 smaller child triangles, see Figure 4.3, which is valid for every further nested domain. The timestep Δt is multiplied by a factor of 0.5 for each nesting levels (Prill et al., 2020). The one-way nesting mode also includes a sponge layer at the border of each model domain to prevent propagating waves of crossing the lateral boundary. In this layer the propagating wave is smoothed down to the value of the lateral boundary, which is called the *lateral boundary nudging*. An additional "forcing" term is added to the right hand side of the prognostic equations for v_n, θ_v, ρ and q_v (Prill et al., 2020):

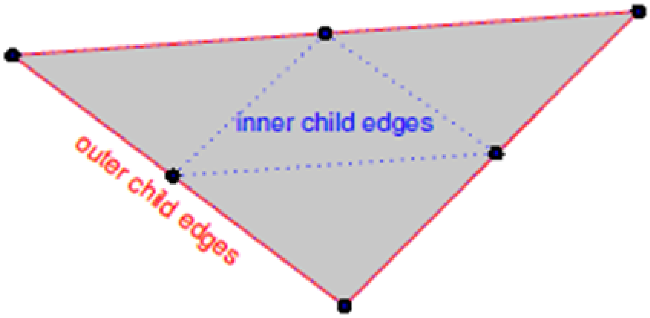

Figure 4.3: Nested grid example of a parent triangle consisting of four smaller child triangles. The outer edges of the outer child triangles overlap the edges of the parent triangle (red line), the inner child triangle is marked by blue dotted lines. The black dots mark the child triangle vertices. Graphic from the Prill et al. (2020).

$$\phi(t) = \phi^*(t) + \alpha_{nudge}\frac{\Delta t}{\Delta\tau}\delta\phi, \tag{4.5.1}$$

where $\phi(t)$ is the prognostic variable at time t, $\phi^*(t)$ is the state before the nudging and $\delta\phi$ is the nudging increment. This method is derived by Davies (1976, 1983). The nudging coefficient α_{nudge} decreases with increasing distance from the boundary. For the lateral boundary conditions α_{nudge} follows:

$$\alpha_{nudge} = A_0 \exp\left(-\frac{|r-r_0|}{\nu}\right), \text{ if } |r-r_0| \leq L. \tag{4.5.2}$$

$A_0 = 0.02$ (`nudge_max_coeff` in `interpol_nml`) describes the maximum relaxation coefficient in the lateral nudging zone, r is the actual cell row index, r_0 the starting cell row index, where the nudging zone begins, $\mu = 2.0$ (`nudge_efold_width` in `interpol_nml`) is the e-folding width given in units of cell rows and $L = 10$ (`nudge_zone_width` in `interpol_nml`) is the width of the lateral nudging zone, also given in units of cell rows (Prill et al., 2020). It is also possible to apply vertical nudging to the upper boundary if the necessary data is provided. For more details about that, make sure to read section 6.2 of the Prill et al. (2020).

4.6 Parametrizations

In this section, the important schemes used in this study of the lower boundary layer are explained. To investigate the performance of the model for arctic boundary layer studies, two different implemented turbulence schemes were tested. One is an adapted version of the Mellor-Yamada model based on Mellor and Yamada (1982), implemented by Raschendorfer (2001). The related surface transfer scheme is an extension of the turbulence model. The approaches are described in Section 4.6.3. The other one is the Smagorinsky turbulence scheme by Lilly (1962); Smagorinsky (1963), integrated by Dipankar et al. (2015). This turbulence scheme includes a surface transfer approach by Businger et al. (1971) following Louis (1979). They are described in Section 4.6.4.

The subgrid-scale orographic drag and the non-orographic gravity wave drag are switched off in the model, because the subgrid-scale-orographic effects are considered to be too small to impact a domain with high resolved mesoscale grid sizes.

The surface sea ice parametrization is described by a bulk-thermodynamic sea ice scheme, implemented by Mironov et al. (2012) and is described in section 4.6.5. Note that in all parametrizations of ICON the roughness length over sea ice is $z_0 = 0.001\,\mathrm{m}$.

4.6.1 Radiation scheme

Radiation plays a crucial role in driving the boundary layer forcing, and accurate treatment of radiation is essential for accurate near-surface temperature modeling (Hogan and Bozzo, 2018). The ecRad radiation scheme, developed by Hogan and Bozzo (2018) for the European Centre for Medium-Range Weather Forecasts (ECMWF), has been successfully integrated into the ICON model by Rieger et al. (2019) and became operational in April 2021 (Deutscher Wetterdienst, 2021). Compared to its predecessor, the Rapid Radiative Transfer Model (RRTM) from Mlawer et al. (1997), the ecRad scheme is more efficient and computationally faster. In addition, the ecRad solver produces less noise in the atmospheric heating rates (Hogan and Bozzo, 2018). The ecRad package offers three different solvers, namely, the Monte-Carlo Independent Column Approximation (McICA) solver by Pincus et al. (2003), the Triplecloud solver by Shonk and Hogan (2008), and the Speedy Algorithm for Radiative Transfer through Cloud Sides (SPARTACUS) solver by Hogan and Bozzo (2016) and Schäfer et al. (2016). Although the latter two solvers have some advantages, they are slower than the McICA solver. Therefore, only the McICA solver is currently used in ICON, as the other solvers have not yet been tested (Rieger et al., 2019). The McICA solver uses an advanced cloud generator, which generates cloud profiles in a stochastic manner and is able to represent three different cloud overlap scenarios (Hogan and Bozzo, 2018). ecRad provides the ability to treat long-wave scattering by clouds and/or aerosols. In ICON, long-wave scattering is only represented by clouds to reduce computational cost (Rieger et al., 2019). The upwelling and downwelling long-wave transport is calculated by a two-stream approximation, where the Planck function is assumed to vary linearly with the optical depth of the atmospheric layer (Wiscombe, 1976). In the non-scattering (clear sky) the upwelling and downwelling long-wave radiation are functions of transmittance, reflectivity, upward emission from the top of the layer, and downward emission from the bottom of the layer (Clough et al., 1992). A full scattering calculation is more complex and extensive and also depends on the inclusion of the surface albedo (see Meador and Weaver (1980) and Stackhouse Jr and Stephens (1991)). Both cases are combined in ecRad to solve the long-wave irradiance more efficiently. The non-scattering calculation is used first to solve the long-wave irradiance for the entire vertical column, and the more expensive cloud layer formulas are used only when necessary by overwriting the clear sky values.

4.6.2 Microphysics

Two microphysical approaches are implemented in ICON (Prill et al., 2020). The single-moment scheme from Seifert (2008) and the double-momentum scheme from Seifert and Beheng (2006). High resolving mesoscale climate models demand a more sophisticated approach to reduce the model biases and to simulate more complex interactions between cloud droplets, raindrops, cloud ice, snow and graupel (Seifert and Beheng, 2006), because cloud processes have a significant impact on precipitation and radiation and thus, the atmospheric dynamics (e.g. Lee and Donner (2011)). The double-momentum scheme calculates explicitly the evolution of mass and number concentrations of all hygrometers in terms of rate equations, including a full treatment of cloud droplet number concentrations (Seifert and Beheng, 2006). In warm phase clouds the microphysical variables are described by the partial power law by Seifert and Beheng (2006)

$$M_{\mathrm{i}}^{k} = \int_{0}^{\inf} x^{k} f_{\mathrm{i}}(x) dx, \tag{4.6.1}$$

where $M_{\mathrm{i}}^{k} = M_{\mathrm{i}}^{k}(\mathbf{r}, t)$ describes the partial moments with indexes of number densities $k = 0$, of mass densities $k = 1$, of cloud droplets $i = c$, and of rain drops $i = r$. x is the drop mass, which under the threshold of $x^{*} = 2.6 \times 10^{-10}$ kg are considered to be of clouds droplets and above that threshold considered rain drops. The partial size distributions $f_{\mathrm{i}}(x)$ are described by generalized Γ-distributions. The budget equations for the partial moments follows

$$\frac{\partial M_{\mathrm{i}}^{k}}{\partial t} + \nabla \cdot (\mathbf{v} M_{\mathrm{i}}^{k}) - \nabla \cdot (K_{\mathrm{h}} \nabla M_{\mathrm{i}}^{k}) + \frac{\partial}{\partial z}(\hat{v}_{\mathrm{i,k}} M_{\mathrm{i}}^{k}) = S_{\mathrm{i}}^{k}. \tag{4.6.2}$$

K_{h} is the turbulent diffusion coefficient for heat, $\mathbf{v}$ the total wind speed, $\hat{v}_{\mathrm{i,k}}$ the mean sedimentation velocities, and S_{i}^{k} the source terms of nucleation, condensation, evaporation, collision, and breakup.

In ice phase clouds the power laws describe the diameter-mass and velocity-mass-relations as follows

$$D(x) \cong a x^{b}, \tag{4.6.3}$$

$$v(x) \cong \alpha x^{\beta} \left(\frac{\rho_0}{\rho}\right). \tag{4.6.4}$$

The values of the constant coefficients a, b, α, β vary with hygrometer type. Equations 4.6.3 and 4.6.4 describe particles formed by nucleation, water freezing, collection, conversion, and melting processes. However, a detailed description of hail formation is not included (Seifert and Beheng, 2006).

4.6.3 Mellor-Yamada scheme

By default the 2nd-order closure on Level 2.5 of anisotropy according to Mellor and Yamada (1982) is used, which calculates the prognostic turbulent kinetic energy equation

(TKE) (Raschendorfer, 2001). This equation includes third-order momentum terms that need to be closed, as well as pressure-correlation terms and dissipation terms. Considering a quasi-isotropic state of stress, the co-variances, such as dissipation and pressure correlation, are closed according to Kolmogorov and Tikhomirov (1959); Rotta (1951). Only the trace among the 2nd-order momentum terms in the Favre-averaged Reynolds stress-tensor τ_{ij}, that are proportional to the TKE, are described by a prognostic equation (Raschendorfer, 2001). The other 2nd-order terms $\overline{v_i''v_k''}, \overline{v_j''v_k''}$ and $\overline{v_k''\theta''}$ are described as linear diagnostics that can be expressed by two turbulent diffusion coefficients, proportional to the square root of the TKE and an integral turbulent mixing length scale l (Raschendorfer, 2001):

$$K_{\mathrm{m}} = lS_{\mathrm{m}}\sqrt{2e}, \tag{4.6.5}$$

$$K_{\mathrm{h}} = lS_{\mathrm{h}}\sqrt{2e}, \tag{4.6.6}$$

where K_m is the turbulent diffusion coefficient for the horizontal wind components and K_h is the turbulent diffusion coefficient for the scalars. S_m and S_h are stability corrections calculated by two sets of linear equations. This single master length scale is specific for each location and is increasing monotonically with height according to Blackadar (1962)

$$l = \frac{\kappa z}{1 + \frac{\kappa z}{l_0}}. \tag{4.6.7}$$

l_0 describes the asymptotic length scale of the Prandtl-layer and is proportional to the horizontal grid spacing $l_0 \propto 1/2\Delta_x$. The turbulent fluxes are then described by a set of second-order flux-gradient equations (Doms et al., 2021)

$$Q_{\mathrm{m_{i,j}}} = \overline{v_{i,j}''v_k''} = -K_{\mathrm{m}}\frac{\partial \hat{v}_{i,j}}{\partial z}, \tag{4.6.8}$$

$$Q_{\mathrm{s}} = \overline{v_k''\theta''} = -K_{\mathrm{h}}\frac{\partial \hat{\theta}}{\partial z}, \tag{4.6.9}$$

$$Q_{\mathrm{l}} = \overline{v_k''q_{\mathrm{v}}''} = -K_{\mathrm{h}}\frac{\partial \hat{q}_{\mathrm{v}}}{\partial z}. \tag{4.6.10}$$

$Q_{\mathrm{m_{i,j}}}$ describes the momentum fluxes, Q_{s} and Q_{l} are describing the sensible heat fluxes and latent heat fluxes, respectively. The TKE is characterized by the turbulent velocity scale $q := \sqrt{2e}$. Assuming horizontal equilibrium and neglecting subsidence in the atmospheric boundary layer, the one dimensional TKE follows from Raschendorfer (2001) in

$$\frac{\partial}{\partial t}\frac{q^2}{2} = -K_{\mathrm{h}}\frac{g}{\theta}\frac{\partial \hat{\theta}}{\partial z} + K_{\mathrm{m}}\left[\left(\frac{\partial \hat{v}_i}{\partial z}\right)^2 + \left(\frac{\partial \hat{v}_j}{\partial z}\right)^2\right] + \frac{1}{\bar{\rho}}\frac{\partial}{\partial z}\left[\alpha\bar{\rho}lq\frac{\partial}{\partial z}\left(\frac{q^2}{2}\right)\right] - \frac{q^3}{B_1 l} + q_{\mathrm{sh}}. \tag{4.6.11}$$

θ is the potential temperature, α is a tunable parameter, $B_1 = 16.6$ is a model constant after Mellor and Yamada (1982). All empirical constants were obtained from neutral flows and were directly related to data for the special case where turbulent energy production is in balance with dissipation (Mellor and Yamada, 1982). The first term on the left hand side describes the tendency of the TKE. On the right hand side follows, in order from left to right, the buoyancy (production/consumption) term, the vertical shear production term, the vertical turbulent transport term, the dissipation term, and the last one is describing the horizontal shear production term.

Additionally, the turbulence parametrization includes a statistical cloud-scheme from (Sommeria and Deardorff, 1977) to consider subgrid-scale condensation effects.

The surface fluxes are described by the Mellor-Yamada Level 2 scheme, which is a simplification of the Level 2.5 scheme (Mellor and Yamada, 1982). The surface transfer scheme (STS) used here differs from other classical approaches, where a linear function characterizes the exchange coefficient within the surface layer. Here, the STS calculates the surface fluxes of the prognostic variables by applying a constant flux approximation to the sum of the turbulent and laminar vertical fluxes (Raschendorfer, 2001). The turbulence scheme is applied to the top of the lowest atmospheric layer (the lowest full level) and the roughness layer. In the roughness layer, an additional so-called "transfer layer resistance term" is added to the profile function of the gradients that is described by a specific transfer layer resistance length scale between roughness layer and lowest atmospheric layer. To estimate the turbulent diffusion coefficient, a vertical interpolation function is developed based on the TKE between the lowermost atmospheric layer and the roughness layer, and then extrapolated to the rigid surface. It follows

$$C_\mathrm{d} = \frac{K_\mathrm{m}}{r^M_\mathrm{SA}|v_\mathrm{ij}(\Delta z)|}, \tag{4.6.12}$$

$$C_\mathrm{h} = \frac{K_\mathrm{h}}{r^H_\mathrm{SA}|v_\mathrm{ij}(\Delta z)|}. \tag{4.6.13}$$

The dimensionless transfer coefficients for momentum, heat and moisture are denoted by C_d, and C_h, respectively. $v_\mathrm{ij} \equiv \sqrt{\hat{v}_i^2 + \hat{v}_j^2}$ is the absolute wind speed at the lowermost atmospheric level. For the laminar and roughness layer transfer, the effective transfer layer resistances for momentum and scalar are denoted by r^M_SA and r^H_SA, respectively. Presumably, these functions incorporate an empirical stability criterion related to the critical Richardson number. On this way, the STS does not make use of the Monin-Obukhov stability functions, but generates these functions through extrapolation of the turbulent diffusion coefficients and a formulation of a resistance length scale. In this way the desired vertical transport of the flux gradient between surface layer and atmospheric layers are enabled. The TERRA land model calculates the final surface fluxes of water vapor and sensible heat as a function of updated specific humidity and potential temperature. These surface fluxes are then used to solve an implicit vertical diffusion equation within the turbulence scheme.

4.6.4 Smagorinsky scheme

Compared to classical NWP forecasts some of the parametrizations of the DWD and MPI are invalid for ICON-LEM and must be turned off (Dipankar et al., 2015). This includes i.e. the convection scheme. On the other hand, different parametrizations have to be switched on for ICON-LEM, such as the radiation scheme ecRad by Hogan and Bozzo (2018) and the double-momentum cloud microphysics by Seifert and Beheng (2006). Lilly (1962) assumed that the sub-grid scale eddy fluxes for momentum and heat are proportional to the eddy exchange coefficients and the velocity and velocity-temperature mean gradients, respectively. He further assumed, that these sub-grid scale eddies are constant and isotropic within a space-time grid square Δ. Smagorinsky (1963) developed a specific 1st-order approximation unlike the usual turbulence parametrizations. In the Smagorinsky scheme, larger eddies of a minimum size Δ are triggered directly and the smaller ($< \Delta$) sub-grid scale eddies are parametrizised via K-theory according to Lilly (1962). The underlying statement is that the larger eddies carrying the main part of the Reynolds stress and are directly influenced by the boundary conditions, whereas the sub-grid scale eddies are much weaker and thus, contributing less to the Reynolds stresses (Wilcox, 2006). The smallest scales are assumed to have a more universal character. Especially near the surface, where all eddies are small, their length (and energy transportation) range along the stress-bearing and dissipation. The turbulent transfer terms $Q(v_n)$ and $Q(w)$ are described by the gradient approximation, which is calculated as the divergence of the sub-grid scale stress tensor τ_{ij} (Dipankar et al., 2015),

$$Q(v_i) = \left(\frac{\partial \hat{v}_i}{\partial t}\right)_{\text{turb}} = \frac{1}{\bar{\rho}}\frac{\partial \tau_{ij}}{\partial x_j}. \tag{4.6.14}$$

The sub-grid scale stress tensor τ_{ij} is parametrized as follows

$$\tau_{ij} = K_\text{m}\left(\hat{S}_{ij} - \frac{1}{3}\hat{S}_{kk}\delta_{ij}\right), \tag{4.6.15}$$

with the strain rate tensor

$$\hat{S}_{ij} = \frac{1}{2}\left(\frac{\partial v_i}{\partial x_j} + \frac{\partial v_j}{\partial x_i}\right), \tag{4.6.16}$$

and its norm $|S| = (\hat{S}_{kl}\hat{S}_{kl})^{1/2}$. The eddy exchange coefficient for momentum K_m is related to the eddy exchange coefficient for heat K_h as

$$K_\text{m} = K_\text{h} Pr_t, \tag{4.6.17}$$

with the Prandtl number Pr_t. K_h is calculated following Lilly (1962)

$$K_\text{h} = \begin{cases} 2 l_s Pr_t \bar{\rho} |S| \cdot \sqrt{1 - \frac{R_i}{Pr_t}}, & 1 - \frac{R_i}{Pr_t} > 0 \\ 0.001\, m^2\, s^{-1}, & 1 - \frac{R_i}{Pr_t} <= 0. \end{cases} \tag{4.6.18}$$

The sub-grid length scale l_s increases proportional to the grid volume $\Delta = (\Delta_x \Delta_y \Delta_z)^{1/3}$

$$l_s = \frac{(c_s \Delta)^2}{1 + \left(\frac{c_s \Delta}{\kappa \cdot z_g(h)}\right)}. \tag{4.6.19}$$

The Smagorinsky coefficient can be calibrated depending on the flow, but has a typical value of around $c_s \approx 0.23$. $c_s\Delta$ is similar to the mixing-length formula, which is in harmony with the assumption by Lilly (1962), but should not be confused with it, as Δ is not universal. If so, the physical assumption behind the mixing-length theory were valid for 1st-order closures and eddies would behave like molecules, which is simply not true (Wilcox, 2006). It assumes that turbulence spread isotropically and that there exist a local equilibrium between stress and strain. R_i is the Richardson number for stabilization reasons

$$R_i = \begin{cases} \frac{N_m^2}{|S|^2}, & \text{for saturated air} \\ \frac{N^2}{|S|^2}, & \text{for unsaturated air.} \end{cases} \tag{4.6.20}$$

N and N_m describe the dry and moist Brunt Väisala frequency (Dipankar et al., 2015),

$$N^2 = \frac{g}{\theta}\frac{\partial \theta}{\partial z}, \tag{4.6.21}$$

$$N_\text{m}^2 = [N^2 + \frac{g}{T}(\Gamma_\text{m} - \Gamma_\text{d})]\left(1 + \frac{L_\text{v} q_\text{sat}}{R_\text{d} T}\right). \tag{4.6.22}$$

Γ_m and Γ_d are the moist and dry adiabatic lapsrate and L_v is the latent heat of evaporation.
$Q(\overline{\rho}\hat{\theta}_\mathrm{v})$ and $Q(\overline{\rho}\hat{q}_i)$ represent the the effects of sub-grid turbulent diffusion and condensation (Dipankar et al., 2015). The condensation terms for each of the thermodynamic equations are calculated by the standard adjustment scheme by Sommeria (1976) and their turbulent terms are expressed through prognostic variables that read

$$\frac{\partial \hat{\theta}_v}{\partial t}_{turb} = \left[1 + \frac{R_\mathrm{d}}{R_\mathrm{v} - 1}\hat{q}_\mathrm{v} - \hat{q}_\mathrm{l}\right] \frac{\partial}{\partial z}\left(K_\mathrm{h}\frac{\partial \hat{\theta}}{\partial z}\right) + \hat{\theta}\left[\frac{R_\mathrm{d}}{R_\mathrm{v} - 1}\left(\frac{\partial \hat{q}_\mathrm{v}}{\partial t}\right)_{turb} - \left(\frac{\partial \hat{q}_\mathrm{l}}{\partial t}\right)_{turb}\right], \tag{4.6.23}$$

$$\frac{\partial \hat{q}_i}{\partial t}_{turb} = \frac{\partial}{\partial z}\left(K_\mathrm{h}\frac{\partial \hat{q}_i}{\partial z}\right), \tag{4.6.24}$$

with $\hat{\theta}$ the potential temperature, $\hat{q}_\mathrm{l}$ the tracer of liquid water, and R_d and R_v are the gas constants for dry air and water vapor, respectively.

The surface transfer scheme used by the Smagorinsky turbulence is a simple GME scheme, based on the approach by Businger et al. (1971) following Louis (1979). Similar to the turbulence scheme described in 4.6.3, the turbulent exchange coefficients are extrapolated to the surface. The surface momentum fluxes Q_m and surface heat fluxes Q_s, Q_l are described in the surface transfer scheme in context of the Monin-Obukhov similarity theory (MOST, (Monin and Obukhov, 1954)) through the wind and temperature gradients

$$Q_{\mathrm{m}_{\mathrm{i,j}}} = -\overline{\rho}C_\mathrm{d}|v_\mathrm{ij}(\Delta z)|\frac{\partial \hat{v}_\mathrm{i,j}}{\partial z}, \tag{4.6.25}$$

$$Q_\mathrm{s} = -\overline{\rho}C_\mathrm{h}|v_\mathrm{ij}(\Delta z)|\left(c_p\frac{\partial \hat{\theta}}{\partial z} + \Phi(\Delta z)\right), \tag{4.6.26}$$

$$Q_\mathrm{l} = -\overline{\rho}C_\mathrm{h}|v_\mathrm{ij}(\Delta z)|\frac{\partial \hat{q}_\mathrm{v}}{\partial z}L. \tag{4.6.27}$$

$\Phi(\Delta z)$ has the unit $m^2\, s^{-2}$ and describes the geopotential thickness of the surface layer $v_\mathrm{ij}(\Delta z)$ the absolute wind speed at the lowest model level, and L being either the latent heat of sublimation $L = L_\mathrm{s}$ over sea ice, or the latent heat of vaporization $L = L_\mathrm{v}$. Q_s is the surface sensible heat flux and Q_l the surface latent heat flux. C_d is the dimensionless transfer coefficient for momentum, C_h the one for heat and moisture

$$C_\mathrm{d} = C_\mathrm{dn}f_\mathrm{m}(Ri), \tag{4.6.28}$$

$$C_\mathrm{h} = C_\mathrm{hn}f_\mathrm{h}(Ri). \tag{4.6.29}$$

$f_m(Ri)$ and $f_h(Ri)$ are stability functions, which take the thermal stratification into account. C_dn and C_hn are neutral transfer coefficients for momentum and heat, respectively. They follow the gradient approach as

$$C_\mathrm{dn} = \left(\frac{\kappa}{\log\left(\frac{\Phi(\Delta z)}{z_m}\right)}\right)^2, \tag{4.6.30}$$

$$C_\mathrm{hn} = \frac{\kappa^2}{\log\left(\frac{\Phi(\Delta z)}{z_m}\right)\log\left(\frac{\Phi(\Delta z)}{z_h}\right)}. \tag{4.6.31}$$

z_m and z_h are the roughness length for momentum and heat, respectively. κ is the von Karman constant.

4.6.5 Sea ice scheme

The sea ice scheme implemented in ICON uses a bulk-thermodynamical approach developed by Mironov et al. (2012). The horizontal sea ice coverage, i.e., sea ice fraction, is given by the data assimilation scheme during the initialization of the model (Prill et al., 2020). If the sea ice fraction is at least greater than 0.5 the grid box is considered to be ice covered (Mironov et al., 2012). Otherwise, the grid cell is defined as ice-free and remains in this state throughout the whole simulation period. During the model run the sea ice cover and the surface sea ice temperature are getting updated 3-hourly with global ICON forecast data (Section 4.5). The rate of change of the sea ice surface temperature and the sea ice thickness are determined by means of an integral heat budget by assuming a parametric temperature profile within the ice slab. The equations for the evolution of the sea ice thickness H_i and surface sea ice temperature θ_i are based on Baldauf et al. (2020); Mironov et al. (2012) read

$$\rho_i L_f \frac{dH_i}{dt} = -\kappa_i \Phi_i'(0) \frac{\theta_i - \theta_f}{H_i}, \tag{4.6.32}$$

$$C_{*i} H_i \frac{d\theta_i}{dt} = \frac{Q_\mathrm{a}}{\rho_i c_i} - \Phi_i'(0) \frac{\kappa_i}{\rho_i c_i} \frac{\theta_i - \theta_\mathrm{f}}{H_i} \times \left[1 + \left(\frac{3}{2} - 2C_{*i}\right) R_{\theta_i}\right], \tag{4.6.33}$$

with the dimensionless parameter $R_{\theta_i} = \frac{c_i}{L_\mathrm{f}}(\theta_i - \theta_\mathrm{f})$. The variables θ_f is the salt-water freezing point. Q_a is the total atmospheric heat flux for the ice slab. ρ_i is the density of ice, L_f the latent heat of fusion, c_i the specific heat of the ice and κ_i the molar heat conductivity of ice for heat transfer from water through ice. $\Phi_i'(0)$ is the derivative at $\zeta = 0$ of the non-linear shape factor for the temperature profile C_{*i}. The term on the left-hand side of eq. (4.6.33) describes the heat capacity of the ice slab, where C_{*i} is expressed as

$$C_{*i} = \frac{1}{2} - \frac{(1 + \phi_*)}{12} \left(\frac{H_i}{H_{max}}\right), \tag{4.6.34}$$

with the dimensionless derived disposable parameter $\phi_* = 2$. The equations (4.6.32) and (4.6.33) represent the mass heat balance for freezing conditions. The melting from below (heat transfer from water to ice) is neglected, as well as the penetrating solar radiation into the ice slab. For melting from above the time rate of change for the sea ice thickness is mainly depending on the relationship between the atmospheric heat fluxes and the conductive heat fluxes of the ice slab. The surface temperature is then set equal to fresh water freezing point $\theta_i = \theta_{\mathrm{f}0}$. If the sea ice thickness falls below a threshold value $H_i < H_\mathrm{cr}$, a quasi-steady regime is assumed for the heat transfer through the ice, where the ice boundaries are balanced by the conductive heat fluxes (Baldauf et al., 2020). In this case, the rate of temperature change is set to zero $d\theta_i/dt = 0$.

The effect of snow is not considered explicitly, but implicitly by the temperature dependency of the sea ice surface albedo. However, this leads to difficulties in the sea-ice surface temperature response to atmospheric forcing. A simplified solution is addressed in section 5, where a new parametrization of the temperature profile shape factor C_{*i} for the uppermost surface sea ice layer is presented, which makes the ice surface react faster to atmospheric changes.

4.7 Difference to classical LES Models

Over the last 15 years ICON-LEM has been applied to study the atmospheric boundary layer with grid-scales around several hundreds of meters to resolve convective cloud processes (e.g. (Rybka, 2020), (Ori et al., 2020), and others) down to 50 m horizontal grid-resolution on a semi-idealized setup (e.g. (Schemann et al., 2020)).

ICON-LEM employs coarser horizontal grid-scales (>50 m) and larger domain sizes, in contrast to the fine-scale resolution (<10 m) and smaller domains typically used in standard LES models. This choice of grid scale and domain size in ICON-LEM allows the simulation of larger scale atmospheric phenomena while still capturing large scale turbulent processes.

In addition to the differences in grid scale and domain size, ICON-LEM contains physical packages that are different from conventional LES models. Conventional LES models tend to use higher order parameterizations than ICON-LEM, which also includes NWP packages. This integration allows ICON-LEM to take advantage of both the advanced turbulence representations of LES models and the comprehensive physical processes considered in NWP models.

To provide a clearer comparison between ICON-LEM and a conventional LES model, an overview of the modules used in ICON-LEM and the Parallelized Large-eddy Simulation Model (PALM) (see Hellsten et al. (2020) and Maronga et al. (2015) for more details) are presented in Table 4.1. In particular, ICON-LEM uses the 1st-order Smagorinsky scheme to describe turbulence, while PALM uses the 1.5-order Deardorff scheme, which includes a prognostic equation for the subgrid-scale turbulent kinetic energy.

Furthermore, ICON-LEM uses the Flux-Form Semi-Lagrangian (FFSL) scheme for horizontal advection and the Parabolic Spline Method (PSM) for vertical advection. In contrast, PALM uses a one-dimensional advection scheme by employing a 5th-order upwind discretisation method.

Setup	**ICON-LEM**	**PALM**
Dynamic	compressible	incompressible
Turbulence	Smagorinsky	Deardorff TKE
Horizontal advection	FFSL	-
Vertical advection	2nd-order PSM	5th-order
Microphysics	2nd momentum	2nd momentum
Radiation	ecRad	-
Time integration	Euler forward	3rd order Runge-Kutta
Lateral boundary	forecast	Semi-idealized

Table 4.1: Comparison between ICON-LEM and as an example for a classical LES model the model PALM.

5. Experimental Setup

In this study, ICON-LEM is set up in one-way online nesting mode, which implies that boundary conditions are updated in one direction from the outer (coarser) parent grid to the inner (finer) child grid. For instance, the horizontal grid size with 800 m resolution is the parent grid, the horizontal grid size with 400 m resolution is the first child grid, but also the parent grid for the horizontal grid size of 200 m and so forth. An overview of the four generated horizontal grid sizes used in this study for the experiments for a calm period in February 2020 can be found in Table 5.1 and is schematically demonstrated in Figure 5.1, with center points at 87.653° N and 93.882° E. The overview for an additional experiment for a storm event in November 2019 can be found in Table 5.2 and also in Figure 5.1, with center points at 86.1597° N and 120.9327° E. The centers of each domain were located to fit the drift track of the Polarstern vessel. The netCDF files of the ICON grid were generated online and downloaded with the ICON grid tool from the DWD: `https://webservice.dwd.de`, including additional external parameter files for each grid. A circular grid domain is chosen as it works better with the triangular grid (Neske, 2017). At its lateral boundaries, the model is driven by analysis data from DWD, downscaled with ICON-LAM (see Section 4.5). The lower boundary condition was set up only at the beginning of the model run. The forcing files have a temporal resolution of one hour.

Each weather scenario is tested with two different turbulence schemes. The simulation results of the 2nd-order turbulence closure described in Section 4.6.3 is addressed as "NWP". The 1st-order subgrid scale turbulence closure described in Section 4.6.4 is addressed as "LES". ICON output variables of a local position are compared to ground-based measurements and radiosonde profiles to evaluate the model performance. To obtain a reasonable estimate of the ship's position, the modeled mean of a variable from the five grid points closest to the Polarstern is used.

Surface variables simulated by ICON-LAM are also provided for comparison. These include, for example, sea-ice surface temperature, surface latent heat flux and surface sensible heat flux. The vertical nesting differs between the experiments performed with

Horizontal grid	**Number of cells**	**Number of edges**	**Grid resolution (m)**	**Radius (km)**	**Vertical levels**	**Time step (s)**
R3B11	25852	38985	800	140	80	0.5
R3B12	25892	39045	400	70	80	0.25
R3B13	25888	39040	200	35	80	0.125
R3B14	25896	39052	100	17.5	80	0.0625

Table 5.1: Number of cells and edges, effective horizontal grid resolution, vertical levels and timesteps used for the simulation in February 2020.

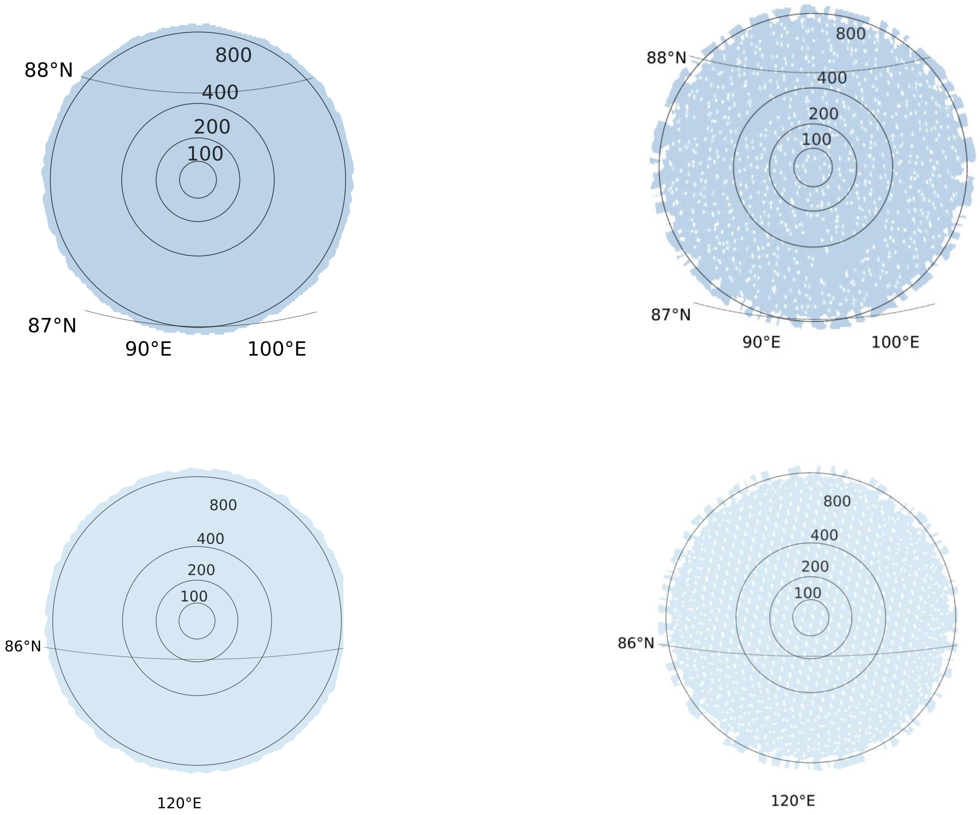

Figure 5.1: Sea ice thickness maps for the different effective horizontal resolutions (circles and numbers) in February 2020 (upper row) and in November 2019 (lower row). Left: Default sea-ice surface structure with a sea ice concentration of 100% in ICON. Right: Sea ice concentration with area-averaged open water fraction of 4% in February 2020 (upper panel) and 6% in November 2019 (lower panel). The sea ice thickness is about 1.5 m thick in February 2020 and about 1 m thick in November 2019.

ICON-LAM and those performed with ICON-LEM. Therefore, only the direct surface variables at grid points closest to the Polarstern position can be compared. From now on the simulation results of ICON-LAM will be named "NWP_Cice-3km".
Experiments without one-way online nesting were also carried out, but showed stronger biases than the nested simulations (not shown here). Therefore, the decision was made to run the experiments in ICON with the recommended setting.

The absence of the tile approach may be negligible for ICON-LEM simulations in the mid-latitudes, but it can deteriorate the performance of ICON-LEM in the central Arctic. The dominating surface type is considered for averaging the surface fluxes, in this case the sea-ice coverage, and the impact of small structures like leads are getting suppressed. With increasing horizontal resolution the surface structure of the lower boundary plays a more important role for the surface energy budget. The downscaling of the analysis data includes the sea-ice concentrations provided by ICON Global analysis and weather forecast data from Prill et al. (2020) (see also Section 4.5). As a result, the provided sea-ice concentration leaves a plain sea-ice structure shown in Figure 5.1, without any leads, rifts, or other uneven surfaces, as the satellites are not able to resolve those complex structures. To investigate the influence of open leads on the near-surface temperature and the vertical wind, a more complex sea-ice surface structure is tested by implementing open-water cracks into the sea-ice surface for both weather situations as was observed during MOSAiC. Four percent of the grid-points of the 800 m grid were set to open-water for the calm weather condition in February 2020 and six percent for the storm event in November 2019 (Figure 5.1). The values are estimated against the sea-ice concentrations observed visually for the two periods during the expedition (Treffeisen et al., 2015), (Spreen et al., 2008). However, the values are set a bit higher to enable a stronger impact on the atmospheric boundary layer. The simulations of the different sea-ice surfaces are done with the LES_Cice. Instead of comparing the mean value at the position near the Polarstern location, the mean value over the whole domain is taken for the comparison of the quantities. On this way, the overall influence of the sea-ice structure gets included properly.

Eight simulations with different physical parametrizations and initial conditions are performed with five different model setups, listed in Table 5.3. The first experiment is made with the default settings in ICON (LES_Ctrl) to investigate the general behavior of the model. This setting includes the original sea-ice scheme (Section 4.6.5) and LES turbulence scheme from Smagorinsky (Section 4.6.4). The simulation results of LES_Ctrl are used for comparison to experiments with adapted sea ice scheme and different turbulence scheme. One experiment includes the LES turbulence from Smagorinsky (LES_Cice) and the other the NWP turbulence scheme from Mellor and Yamada (NWP_Cice, Section 4.6.3). In all three experiments is the surface entirely covered by sea ice and they are

Horizontal grid	Number of cells	Number of edges	Grid resolution (m)	Radius (km)	Vertical levels	Timestep (s)
R3B11	24856	37488	800	140	80	0.5
R3B12	24800	37402	400	70	80	0.25
R3B13	24808	37414	200	35	80	0.125
R3B14	24832	37450	100	17.5	80	0.0625

Table 5.2: Number of cells and edges, effective horizontal grid resolution, vertical levels and timesteps used for the simulation in November 2019.

Experiment	**Sea-ice**	**Turbulence**	**OW**	**Period**
LES_Ctrl (control)	default	1st-order Smagorinsky	-	Feb20, Nov19
LES_Cice	adapted	1st-order Smagorinsky	-	Feb20, Nov19
NWP_Cice	adapted	2nd-order Mellor-Yamada	-	Feb20, Nov19
LES_Cice-4%lead	adapted	1st-order Smagorinsky	4%	Feb20
LES_Cice-6%lead	adapted	1st-order Smagorinsky	6%	Nov19

Table 5.3: Sea-ice schemes and turbulence schemes used in ICON with different sea-ice concentration (SIC).

performed for both periods in February 2020 and November 2019. The two experiments including the adapted sea ice scheme and LES turbulence are performed with open water grid-points of four percent and six percent for the period in February 2020 and November 2019, respectively (Section 7.3).

6. MOSAiC Measurements

The Multidisciplinary Drifting Observatory for the Study of Arctic Climate (MOSAiC) expedition was conducted from 4 October 2019 to 22 September 2020 (Shupe et al., 2022). The icebreaker RV Polarstern has been frozen to an ice floe to collect comprehensive data on the Arctic climate system for a whole year. The ship left the harbor at Trømsø and headed for the Laptev Sea to find a suitable ice floe. After finding an ice floe at 85°N, 137°E, the ship drifted up to 3400 km in total during the expedition (Knust, 2017; Shupe et al., 2020) (Figure 6.1). During the expedition, 21 cyclones were observed, which transported warm air masses and strong winds into the central Arctic and led to strong sea ice deformation (Krumpen et al., 2021; Nicolaus et al., 2022; Rabe et al., 2022; Rinke et al., 2021; Shupe et al., 2022). In addition, there were very cold, windless periods with surface temperatures below $-30°$C. However, the high number of storms during winter and spring dominated this rather atypical year (Shupe et al., 2022). For a spatially limited area, continuous measurements have been collected for all seasons, especially during the polar winter, providing opportunities to determine, for example, the surface energy budget of the Arctic. These measurements allow the assessment of model biases and the development of new model parametrizations. The velocity of the underlying sea ice/ocean ranged from $5cm/s$ for rather calm weather situations up to $25cm/s$ for turbulent events (Rabe et al., 2022). The ship drifted passively with the transpolar drift towards Fram straight between Svalbard and Greenland and experienced a break-up in spring 2020 due to COVID-19, between leg 3 and leg 4, when the next team had to be picked up from Svalbard. Another transition occurred between leg 4 and leg 5, when the ship moved to a completely new floe near the North Pole (Shupe et al., 2022). Along the drift, the ship was surrounded by one-year old sea ice with thickness of approximately 1 to 2 m and an estimated annual snow depth of 25 cm (Krumpen et al., 2021). Operations were performed on board of the ship and on the ice floe. The MOSAiC distributed network was built around the drifting ship, which is shown in Figure 6.2 with a red star marking the position of Polarstern. The measurement instruments were spatially distributed in such a way as to allow the detection of fluctuations, but also to allow the area to correspond to the typical size of a model grid cell (Shupe et al., 2022). For the comparison of the model performance, the preliminary radiosonde data and the near-surface observations of the MET city, mainly the 10 m tower level 2 data sets and the atmospheric surface flux station ASFS40 level 2 data sets were used for this study. It should be noted, that the level 2 data sets are not the final product of the processed observational data. Furthermore, not all of the observed variables used for the comparison were measured at exactly same height as the model output variables. Because some datasets were missing, or the measurement discrepancies were too large, other close variables had to be used (for more details, see also Appendix 8).

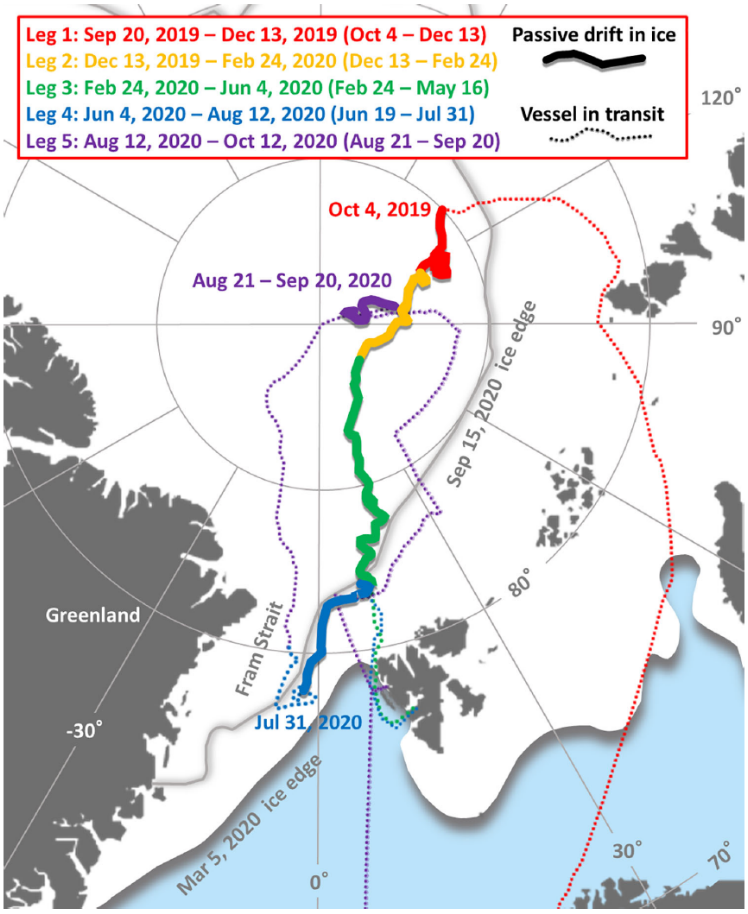

Figure 6.1: Expedition track of the drifting Polarstern (solid lines). Each color corresponds to a leg, dotted lines indicate transfer periods. Including the approximate ice edge maximum (5th of March, 2020) and minimum (15th of September 2020). Figure from Shupe et al. (2022).

6.1 ARM Meteorological tower

The so-called *Central Observatory (CO)* included a network of roads, power lines, and scientific installations, which was built within a radius of 2 km around Polarstern (Shupe et al., 2020, 2022). About 400 to 500 m away from the ship was the MET City Camp, which provided all kinds of atmospheric observations of the Arctic. The measurement system included the ARM skyradiometer (SKYRAD) for downwelling diffusive radiation and the ARM ground radiometers on stand (GNDRAD) for upwelling irradiation (Andreas et al., 2018). The SKYRAD consists of a pyrgeometer (PIR) that was deployed on the sea ice to measure the sky infrared temperature and a sky viewing variable-precision spectral pyranometer (PSP), which is a multifilter rotating broadband radiometer suite to measure diffuse short-wave and long-wave irrandiance. The measurement system also included a Solar Infrared Radiation Station (SIRS). The downwelling long-wave radiation measurements also included the cloud fraction. Similar to the SKYRAD, the GNDRAD consits of a surface-looking PIR to measure the sea-ice surface temperature and a PSP to measure short-wave reflected solar radiation and surface emitted long-wave radiation. Another meteorological station in the MET City Camp was the combined Eddy Correlation Flux Measurement System (ECOR) and the Surface Energy Balance System (SEBS) (Cook and Sullivan, 2020). The SEBS includes infrared and net radiometers and a wetness sensor to measure the heat flux, the temperature and ground moisture. The ECOR consists of a 3D wind sensor (sonic anemometer), to measure wind speed and direction as well as temperature. In addition, the ECOR includes an open path infrared gas analyzer (IRGA) to measure the carbon dioxide concentration. The ECOR thus provides the horizontal and vertical wind speed, the air temperature and specific humidity product, the water vapor and carbon dioxide density product, and the surface momentum, latent and sensible heat flux products. All these measurement systems were mounted together on the 10 m tower (Cox et al., 2021d). The Atmospheric Surface Flux Station (ASFS) was deployed at very dynamic locations on the ice floe (L1-3 in Fig. 6.2) to measure the moving ice and open water cracks within the ice (Cox et al., 2021a,b,c). For this reason, it was sometimes challenging to use the ASFS during severe weather events such as winter storms. There were times during the expedition when the instruments broke down and needed srvicing due to the high winds and the fast drifting ice floe. For this reason, some of the data are not available for certain time periods, including some days in the selected period of the simulation experiments in November 2019, when a severe storm hit the MOSAiC research area. The ASFS is equipped with the ECOR and the SEBS and the SKYRAD and GNDRAD were placed between 3 and 6 m away from the flux station. Note that the tower and the ASFS were installed at different locations of the distributed network, where the positions L, M and P are marked by different colored symbols (Figure 6.2). The tower was deployed for all legs in the CO around the ship for all legs, the ASFS30 was deployed during legs 1 and 4 at position L2 and measured during legs 3 and 5. The ASFS40 was deployed at position L1 and the ASFS50 was deployed at position L3 during legs 1 and 2 and measured between legs 3 and 5.

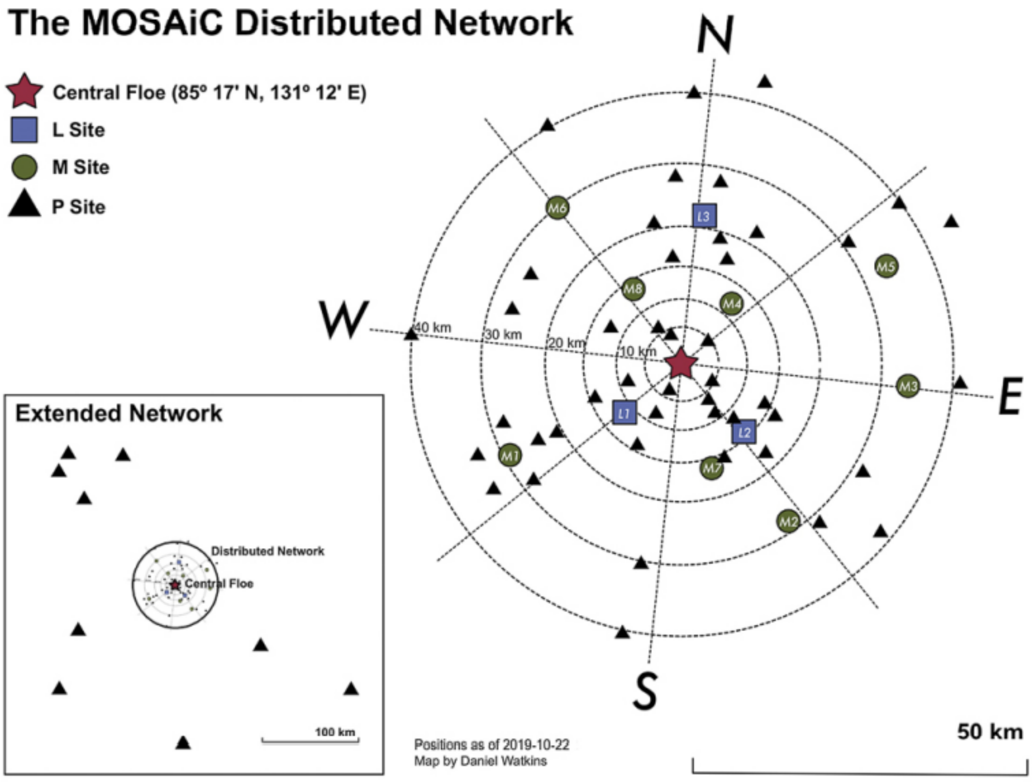

Figure 6.2: The Distributed Network setup for positions around the 22th of October 2019. Shown are the positions of the individual L- (blue squares), M- (green circles), and P-site (black triangles) sites relative to the MOSAiC Central Observatory (red star in the center). Graphic courtesy of Daniel Watkins.

Table 6.1: Atmospheric quantities of MOSAiC measurements used for comparison in this study

Tower	**Instrument**	**Description**	**Height (m)**
Temperature	Vaisala HMT330	Thermometer	1.65, 5.44, 9.34, 30.76
Wind	Metek sonic 3D wind sensor	Anemometer	1.65, 5.44, 9.34, 30.76
Relative humidity	Vaisala PTU300 Vaisala HMT330	Humidity sensor	1.45, 5.24, 9.14, 30.76
Water vapor density	Licor open path IRGA	Gas molar density	1.65, 5.44, 9.34, 30.76
Longwave radiation	Variable	Net flux PSP and PIR	1.5, 3.0
Radiosonde			
Temperature	Vaisala	Platinum Resistor	12 - 1000
Wind	Vaisala	GPS Receiver	12 - 1000
Relative humidity	Vaisala	Thin-Film capacitor	12 - 1000

6.2 Radiosondes

The radiosondes were the backbone of the atmospheric structure measurements (Shupe et al., 2022) and were regularly launched at least four times a day every six hours throughout the expedition, providing the basic thermodynamic structure of the atmosphere. Additional radiosondes were launched in the rhythm of every three hours during special events of interest, or during intensive measurement periods coordinated with the "Year Of Polar Prediction" (YOPP) project (Goessling et al., 2016), e.g. to capture warm air intrusion in mid-April (Shupe et al., 2022). The radiosonde measurements provide vertical profiles of various physical quantities such as temperature, relative humidity, wind speed and direction and pressure. The radiosonde ballons were launched from the 10-11 m high helideck of the Polarstern and were able to reach an altitude of about 30 km, covering the entire troposphere and lower stratosphere (Shupe et al., 2022). The lower radiosonde measurements were affected by the ship's own presence and are not representative for comparison with the low-level model simulations. However, they were the first ones available and the comparison of the preliminary radiosonde data with the model's ability to resolve different weather conditions is sufficient. The data are available in the PANGEA archive (Maturilli et al., 2021).

7. Model evaluation for the central Arctic

Given that ICON-LEM was applied for the first time in the central Arctic region, the adequacy of its horizontal resolution was not immediately clear, in particular the potential benefits of higher resolution over a uniform sea-ice surface. In case of stable stratification eddies have very small scales and LES would need at least 5 m grid sizes to resolve these non-convective eddies. In models, e.g. climate models, with coarser resolution, the effect of eddies has to be parametrized applying generally accepted turbulence closures (e.g. Zonato et al. (2022), Chow et al. (2019), Goger et al. (2019), Goger et al. (2018), Prein et al. (2015), and others).

In order to investigate small-scale interactions within the Arctic boundary layer, a well-validated and Arctic-specific parametrized model is required, whose output is compared with observations to determine its accuracy. Accordingly, the application of ICON-LEM over sea ice in the central Arctic is conducted to explore the added value of higher mesoscale resolution when compared to the standard coarser regional resolution. The horizontal grid sizes of the model range between 100 m and 800 m, between the a grid size of classical large eddy simulations (<10 meters) and of regional simulations (>1 kilometer).

To determine the most suitable turbulence parametrization in this study the model output is compared with observations. Two implemented turbulence parametrizations in ICON are evaluated: The 2nd-order turbulence closure (Section 4.6.3) and the 1st-order sub-grid scale turbulence closure (Section 4.6.4).

The simulation results from ICON-LAM with a grid-resolution of 3 km (NWP_Cice-3km) are also shown for the surface variables, to compare the effect of the lateral boundary conditions on the different experiments.

Only the variables in the lowest grid level are compared to observational data, as the focus of this study lies on the interaction between surface and the lower atmosphere.

The impact of different horizontal resolutions is analyzed in Section 7.1 by introducing a statistical test and investigating the coarsest and finest grid sizes in two different case studies. The results with the adapted sea-ice scheme is analyzed in Section 7.2 and in Section 7.3, the sea-ice surface condition is studied with focus on the vertical structure on a specific day. The impact of the two turbulence parametrization schemes are shown in Section 7.4 for cold, light wind conditions and in Section 7.5 for stormy conditions.

7.1 Impact of the horizontal resolution

The evaluation of the coarsest used horizontal grid scale of 800 m and the finest used horizontal grid-scale of 100 m are addressed for two different weather periods. Since the focus is only on comparing the differences between the simulations for the two grid scales used, the observational data are not included in the following comparisons. The case study for February 2020 is examined in Subsection 7.1.1, followed by the case study for November 2019 in Subsection 7.1.2.

7.1.1 Under cold, light wind conditions

During polar night, the Arctic atmosphere near the surface is mostly stably stratified. For the investigations of the boundary layer near the surface, an observed period of clear skies and very cold weather from 6 to 10 February 2020 is selected and results are compared with observational data. In this way, small-scale processes can be clearly identified.
Figure 7.1 shows the temporal evolution of the sea-ice surface temperature, air temperature at 5 m, specific humidity, and wind speed from LES_Cice with 800 m grid size (LES_Cice-800) and 100 m grid size (LES_Cice-100) for the cold period mentioned above. At first glance, the simulation results of the meteorological variables from the two different horizontal grid size do not seem to differ much from each other. However, the course of the curves show small differences. The variables from the LES_Cice-800 have slightly higher values than from the LES_Cice-100. The largest variations are seen during the very cold period from 7-8 February 2020, with the lowest sea-ice surface temperature at around 234 K and air temperature at 5 m at around 238 K. While for the sea-ice surface temperature the differences are comparably small between LES_Cice-800 and LES_Cice-100, for the air temperature at 5 m the curves differ more from each other. The same applies to the specific humidity at 5 m. Similar variations between the two horizontal grid-scales can be observed for NWP_Cice-800 and NWP_Cice-100 (see Appendix, Figure 3). The wind speed for LES_Cice-800 and LES_Cice-100 shows small variations from 6-8 February 2020, whereas wind speed slightly varies between LES_Cice-800 and LES_Cice-100 in 8-10 February 2020.
An additional simulation result for the sea-ice surface temperature from NWP_Cice-3km is shown in Figure 7.1. The course of the curve from NWP_Cice-3km is lower at the beginning of the simulation period from 6-7 February 2020 than for LES_Cice-800 and LES_Cice-100. However, during the very cold period from 7-8 February, NWP_Cice-3km shows around 6 K higher values compared to LES_Cice-800 and LES_Cice-100. In the period from 8-10 February, the curves of all horizontal resolutions show similar sea-ice surface temperatures, even though NWP_Cice-3km has slightly lower values than the higher grid-resolutions.

Under the assumption that the difference distribution follows a normal distribution, in which the norm of two standard deviations encompass roughly 95% of the distribution, for each variable the mean value of the difference distribution from LES_Cice-800 and minus LES_Cice-100, as well as their mean values

$$\mu_j = \frac{\sum_i^{n_j} x_i}{n_j}. \tag{7.1.1}$$

x_i is the value of the variable at index i and n_j is the sample size of the individual sample with j referring as index for each sample group and their difference. Their corresponding sample standard deviation s_j is given as

$$s_j = \sqrt{\frac{\sum_i^{n_j} (x_i - \mu_j)^2}{n_j - 1}}. \tag{7.1.2}$$

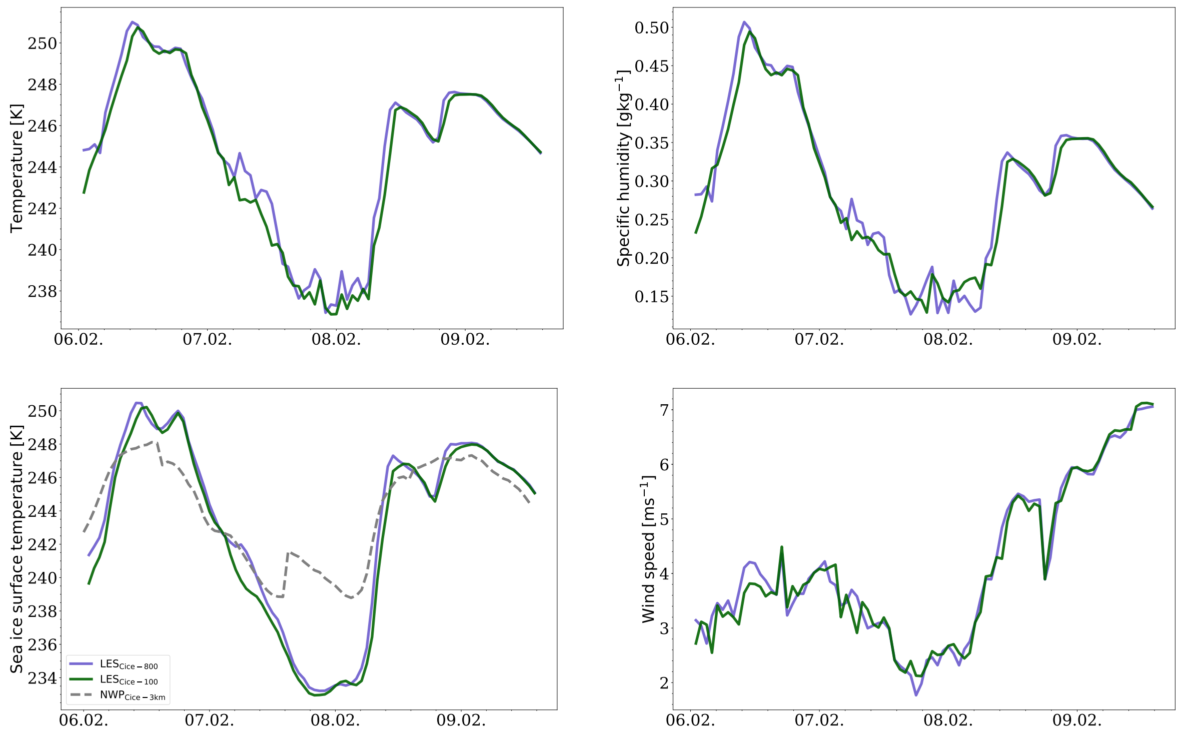

Figure 7.1: Temporal evolution of 5-m temperature (upper left), sea-ice surface temperature (lower left), specific humidity (upper right), and wind speed (lower right) averaged over the whole domain from LES_Cice-800 (blue) and LES_Cice-100 (green) in the period 6-10 February 2020.

To determine whether the difference between the means of LES_Cice-800 and from LES_Cice-100 is statistically significant, an application of a hypothesis test is required. One hypothesis would be that the means of both sample groups are the same $H_0 : \mu_{800} = \mu_{100}$, where H_0 refers to the description of the null hypothesis. This hypothesis states that there is no statistically significant difference between the results obtained from LES_Cice-800 and from LES_Cice-100. On the other hand, the refutation states that there is a statistically significant difference between the results of the two experiments $H_1 : \mu_{800} \neq \mu_{100}$. When a result is described as statistically significant then it is rather unlikely that the hypothesis H_0 is true.

There are several statistical tests with different advantages. For this reason, the choice of test should be made carefully based on the characteristics of the sample. For example, the Student's t-test from Student (1908) is usually used when the distribution of a sample group follows a normal distribution and the variances of two sample groups can be assumed to be equal. On the other hand, the Wilcoxon-Mann-Whitney U-test from Mann and Whitney (1947) and Wilcoxon (1945) is applied to a sample that does not have to be (approximately) normally distributed, or when the data sample is described as rank data.

In this study, Welch's t-test from Welch (1947) is chosen because it assumes that the sample variances s_j^2 from two compared sample groups are unequal (e.g. Ruxton (2006)). The modified formula for the critical values of the test statistic, or t-distribution, t' is calculated by

$$t' = \frac{\mu_1 - \mu_2}{\sqrt{\frac{s_1^2}{n_1} + \frac{s_2^2}{n_2}}}. \tag{7.1.3}$$

Variable	μ_{800}	s_{800}	μ_{100}	s_{100}	ν	t'	p	μ_D
Surface temperature [K]	243.06	5.31	242.55	5.42	167.93	0.6613	0.51	0.5149
5 m temperature [K]	244.62	3.79	244.22	3.94	167.75	0.7185	0.47	0.4031
specific humidity [$\mathrm{g\,kg^{-1}}$]	0.289	0.09	0.284	0.09	168	0.2873	0.77	0.004
wind speed [$\mathrm{m\,s^{-1}}$]	4.09	1.41	4.07	1.41	168	0.1261	0.89	0.0258

Table 7.1: Statistical values of the meteorological variables on 6-10 February 2020. Shown are the mean μ_{800} and the standard deviation s_{800} from LES_Cice-800, the mean μ_{100} and the standard deviation s_{100} from LES_Cice-100, as well as their mean value of the differences μ_D with sample sizes $n_1 = n_2 = 85$. The results of the statistical t-test include the degree of freedom ν, the t-value t', and the p-value p (probability that the null hypothesis is correct).

The degrees of freedom ν is given by (e.g. Ahad and Yahaya (2014))

$$\nu = \frac{\left(\frac{s_1^2}{n_1} + \frac{s_2^2}{n_2}\right)^2}{\frac{\left(\frac{s_1^2}{n_1}\right)^2}{(n_1-1)} + \frac{\left(\frac{s_2^2}{n_2}\right)^2}{(n_2-1)}}. \tag{7.1.4}$$

The degrees of freedom and the t-distribution in a Welch's t-test are important because they are used to determine the significance value, or p-value, of the difference distribution, which shows how strong the evidence is for the sample difference. The higher the degrees of freedom, the more accurate the t-distribution and the more accurate the p-value will be. Therefore, having a high degree of freedom is desirable because it provides greater power and accuracy in hypothesis testing.

The power depends on the selected significance level α. It indicates the probability that the test will produce a statistically significant result if the null hypothesis is true. Usually, the significance level is set to 5% (i.e., α=0.05). Assuming the null hypothesis is true, there is only a 5% chance that a statistically significant result will be obtained. The value of the p-value can then be taken from a look-up t-table (e.g. Fahrmeir et al. (2016)). If the value is below α, i.e. $\alpha > p$, the difference between LES_Cice-800 and LES_Cice-100 of each variable is considered to be significant and the null hypothesis can be rejected. In this case, the mean value of differences would be highlighted in the Table 7.1. However, if the significance value of the distribution of differences is much higher than $\alpha < p$, the differences between the variables from LES_Cice-800 and from LES_Cice-100 are not significant and the null hypothesis must remain valid. For each variable the values μ_{800}, μ_{100}, s_{800}, s_{100}, t', p, ν, and μ_D are listed in Table 7.1.

In addition, the mean value of the differences and the confidence interval for $\alpha = 0.05$ are plotted in the probability density distribution of the differences of Figure 7.2. The corresponding confidence interval for the upper limit and lower limit can be approximated as follows

$$KI\_\alpha = \Delta\mu \pm t_\alpha * \sqrt{\frac{s_1^2}{n_1} + \frac{s_2^2}{n_2}}. \tag{7.1.5}$$

The sample α-value t_α is again be taken from the t-table.

The probability density distribution of different meteorological variables from above from LES_Cice-800 and from LES_Cice-100, and corresponding probability density distribution of the differences between the simulations from LES_Cice-800 and LES_Cice-100 in 6-10 February 2020 are shown in Figure 7.2 (and for NWP_Cice-800 and NWP_Cice-100 in the Appendix, see Figure 4).

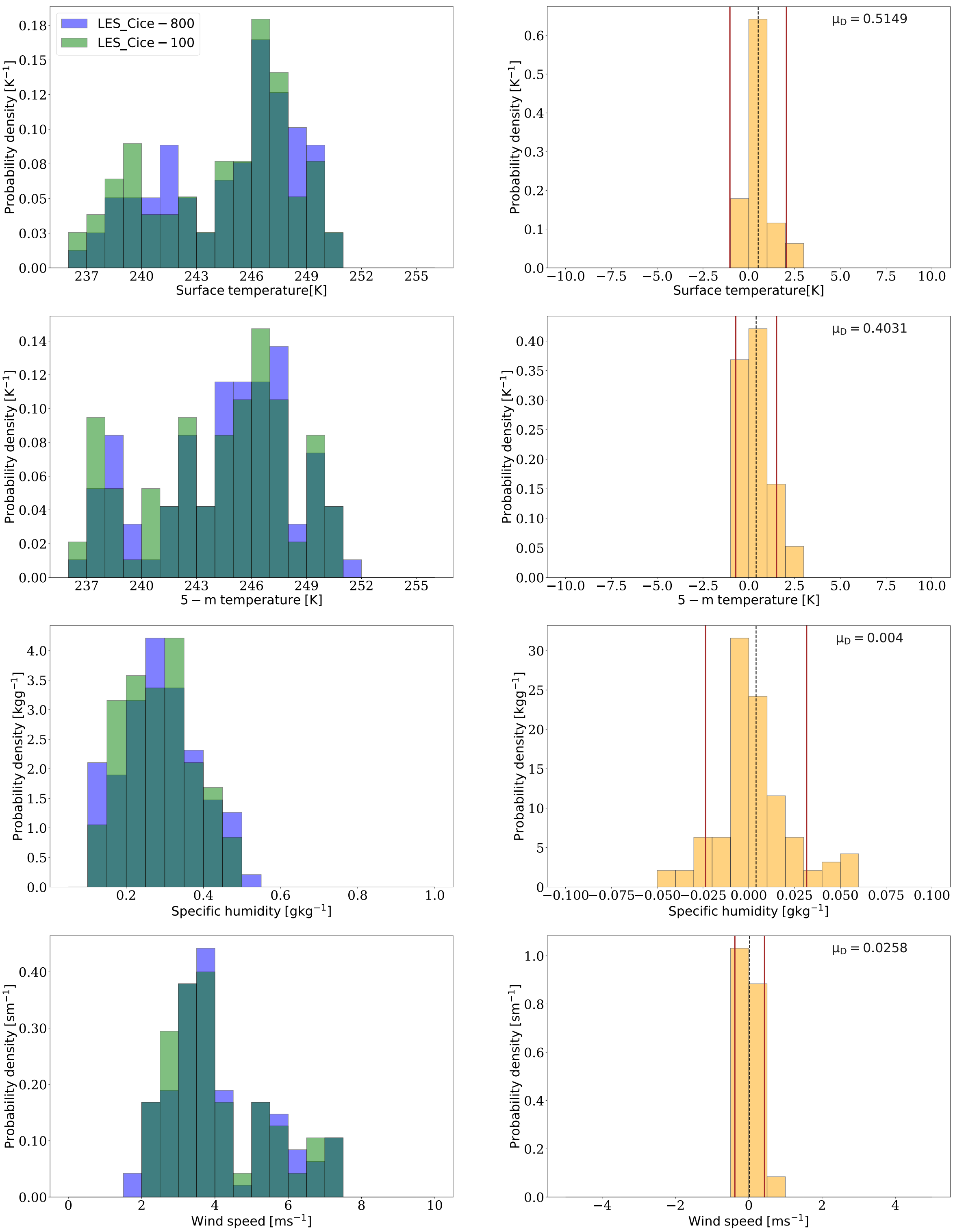

Figure 7.2: Probability density distribution (left) of sea-ice surface temperature, air temperature at 5 m, specific humidity at 5 m, and wind speed at 5 m (from top to bottom) from the simulations with LES_Cice-800 (blue) and LES_Cice-100 (green), and corresponding probability density distribution of the differences between the simulations with LES_Cice-800 and LES_Cice-100 (right) based on hourly data of the period 6-10 February 2020 at the mean Polarstern position. The dashed lines show the mean of the differences for each variable. The red lines show the 95% confidence interval.

With few exceptions, the variables from LES_Cice-800 and from LES_Cice-100 are distributed over the same range of values. The corresponding probability density distribution of the differences of each variable are shown in the right column of Figure 7.2. For all variables, the averages of all differences are obviously close to zero but sometimes larger differences occur, e.g. up to 3 K in case of temperatures, which can be seen in Figure 7.2 more clearly than in Figure 7.1.

However, the differences are not significant and vary on average for all variables around zero.

The probability density distribution for sea-ice surface temperature from LES_Cice-100 ranges on the same values as the probability density distribution from LES_Cice-800. For the lower sea-ice surface temperatures the distribution from LES_Cice-100 shows a shift to colder values compared to the distribution from LES_Cice-800. But also for the warmer sea-ice surface temperatures, the values from LES_Cice-800 are distributed at higher values than the ones from LES_Cice-100.

The probability density distribution for air temperature at 5 m from LES_Cice-800 and LES_Cice-100 show a similar range of values. But the distribution from LES_Cice-800 is slightly shifted towards higher values and the distribution from LES_Cice-100 is slightly shifted towards lower values.

Similar to the temperature variables, the values for specific humidity from LES_Cice-800 and from LES_Cice-100 are distributed over a similar range of values. The distribution of the differences from both models show that their differences are spread evenly and that the difference between both models do not exceed values over $0.05\,\mathrm{g\,kg^{-1}}$.

Also wind speed distributions from both model runs are very similar so that the differences are small with the largest difference of about $1\,\mathrm{m\,s^{-1}}$.

The comparison of the meteorological variables from LES_Cice-800 and LES_Cice-100 for a very cold weather period from 6-10 February 2020 show that with increasing horizontal grid-resolution the temperatures and specific humidity shift towards lower values. However, the differences between the results obtained with two horizontal resolutions are too small to make a significant difference in the overall representation of the atmospheric boundary layer. The results show that the used grid sizes are not fine enough to resolve eddies during stable atmospheric stratification over a plain sea-ice surface. It can be speculated that in case of resolved eddies the resulting wind and temperature development would be less smooth and more irregular. Also distributions of meteorological variables would show more variability in case of resolved turbulence.

7.1.2 Under stormy conditions

In order to evaluate the changes in ICON-LEM for various weather conditions during Arctic winter, a stormy period in November 2019 is chosen for the second investigation. The influence of strong turbulence on near-surface variables is studied with the same model setup mentioned above and compared to the observations.

Figure 7.3 shows the temporal evolution of the meteorological variables from LES_Cice-800 and from LES_Cice-100 for a stormy weather period in 15-21 November 2019. The shaded area in the figures mark periods with unrealistic model results, which resulted from numerical problems caused by disturbances at the boundary of the parent domain and which are propagating through the inner domain, and eventually dissipate at the opposite end of the domain (not shown here). This anomalous behavior at the lateral boundary can be attributed to a numerical problem resulting from an incorrect transition of the

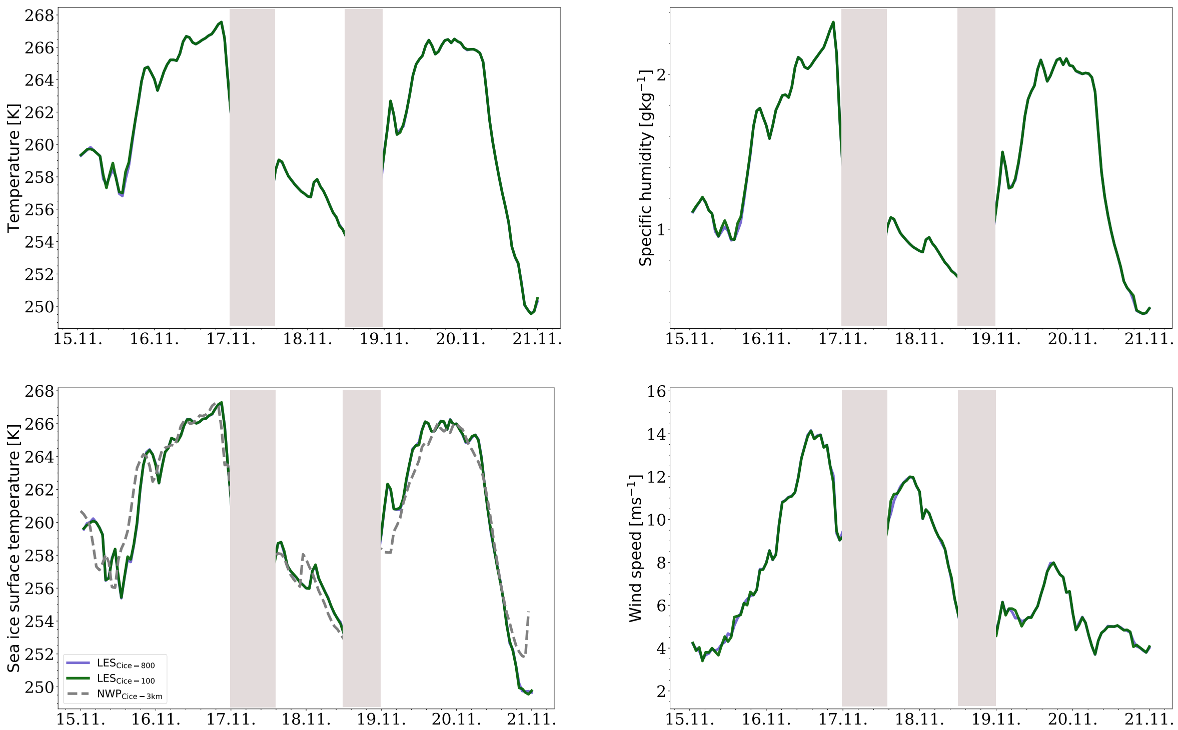

Figure 7.3: Temporal evolution of 5-m temperature (upper left), sea-ice surface temperature (lower left), specific humidity (upper right), and wind speed (lower right) averaged over the whole domain from LES_Cice-800 (blue) and LES_Cice-100 (green) in the period 15-21 November 2019.

atmospheric/lateral boundary condition from the coarser model to the finer grid domain (e.g. during the downscaling process), rather than a physical problem. The coarser model configuration differs in various aspects from the finer setup in several aspects, including physical parametrizations. No other inconsistencies were detected in a test phase during other simulation periods (not shown here), and changes in time steps, sponge-layer width, and nudging-zone width did not prevent the occurrence of this phenomenon.

The increasing values for sea-ice surface and air temperature at 5 m as well as specific humidity at 5 m are indicating that two storms are passing during the two periods between 16 and 17 and between 19 and 20 November 2019. The course of the curves for sea-ice surface temperature, the air temperature at 5 m, and the specific humidity are very similar. A similar development for the meteorological variables is observed for NWP_Cice-800 and NWP_Cice-100 (see Appendix, Figure 5). The maximum temperatures at the sea-ice surface and in the atmosphere near the surface are at around 267 K and the maximum for specific humidity is at around 2.4 g kg^{-1}. During the first storm, the wind speed at 5 m also increased with a maximum at around 14 m s^{-1}, while for the second storm the wind speed dropped to a somewhat lower value at around 8 m s^{-1}. The additional sea-ice surface temperature from NWP_Cice-3km shows less fluctuations compared to LES_Cice-800 and from LES_Cice-100 and differs slightly from the higher resolved model runs.

Table 7.2 shows the statistical values of Welch's t-test (calculated by Equations 7.1.1-7.1.5) for each meteorological variable from LES_Cice-800 and LES_Cice-100 on 15-21 November 2019. Due to the missing data between 17 November 2019 0 h and 14 h and 18 November 2019 12 h 2019 and 19 November 2019 0 h, the sample size for both sample groups decreases. The size of all grid-point samples is the same from LES_Cice-800 and from LES_Cice-100 and therefore the sample sizes are $n_1 = n_2 = 118$.

Variable	μ_{800}	s_{800}	μ_{100}	s_{100}	ν	t'	p	μ_D
Surface temperature [K]	260.72	4.83	260.73	4.83	230	>0.0	0.99	-0.005
5 m temperature [K]	261.09	4.79	261.11	4.78	230	-0.028	0.98	-0.0176
specific humidity [$\mathrm{g\,kg^{-1}}$]	1.41	0.54	1.41	0.54	230	-0.04	0.97	-0.0028
wind speed [$\mathrm{m\,s^{-1}}$]	7.57	2.97	7.60	3.0	230	-0.1	0.92	-0.0009

Table 7.2: Statistical values of the meteorological variables on 15-21 November 2019. Shown are the mean μ_{800} and the standard deviation s_{800} from LES_Cice-800, the mean μ_{100} and the standard deviation s_{100} from LES_Cice-100, as well as their mean value of the differences μ_D with sample sizes $n_1 = n_2 = 116$. The results of the statistical t-test include the degree of freedom ν, the t-value t', and the p-value p.

The probability density distribution of the meteorological variables from above from LES_Cice-800 and from LES_Cice-100, and their corresponding probability density distributions of the differences on 15-21 November 2019 are shown in Figure 7.4 (and for NWP_Cice-800 and NWP_Cice-100 in the Appendix, see Figure 6). As in the case discussed already, the mean value of the differences, calculated by eq. 7.1.1, and the 95% confidence interval, calculated by eq. 7.1.5, are also shown in the difference distributions for each variable. The probability density distributions from LES_Cice-800 and LES_Cice-100 have the same range of values for each variable. Within the range, the distributions alternate for some values between the two model runs. Just as before, the corresponding probability density distribution of the differences of each variable is calculated by the subtraction of LES_Cice-100 from LES_Cice-800. The results show that the deviations between both horizontal grid-resolutions are close to zero and the variables do no differ significantly from each other.

The results of the two model runs show no significant differences from each other in the probability density distribution of the differences. The differences between the values are relatively small, with maximum difference of $1\,\mathrm{m\,s^{-1}}$ between LES_Cice-800 and LES_Cice-100. Furthermore, the mean value of the differences is negligibly small, with values close to zero.

The meteorological variables from LES_Cice-800 and LES_Cice-100 for a very stormy weather period developing from 15-21 November 2019 show less variations between the two different horizontal resolutions than in the case of February 2020. The differences between the model runs are very small and the increasing resolution seem to have a lower impact on the low atmospheric boundary layer than in the case study before. Especially the sea-ice surface temperature does not change much with increasing resolution (Figure 7.3). Only wind speed shows a somewhat stronger variation between the simulation results from LES_Cice-800 and LES_Cice-100. No accountable benefit can be gained out of increasing grid-resolution. The reason is that for strong given turbulence that storms bring, the sub-grid scale turbulence plays a rather minor role for the differences between different resolutions. In the following, only the simulation results of LES_Cice-100 are used for the comparison and will be referenced as LES_Cice from now on.

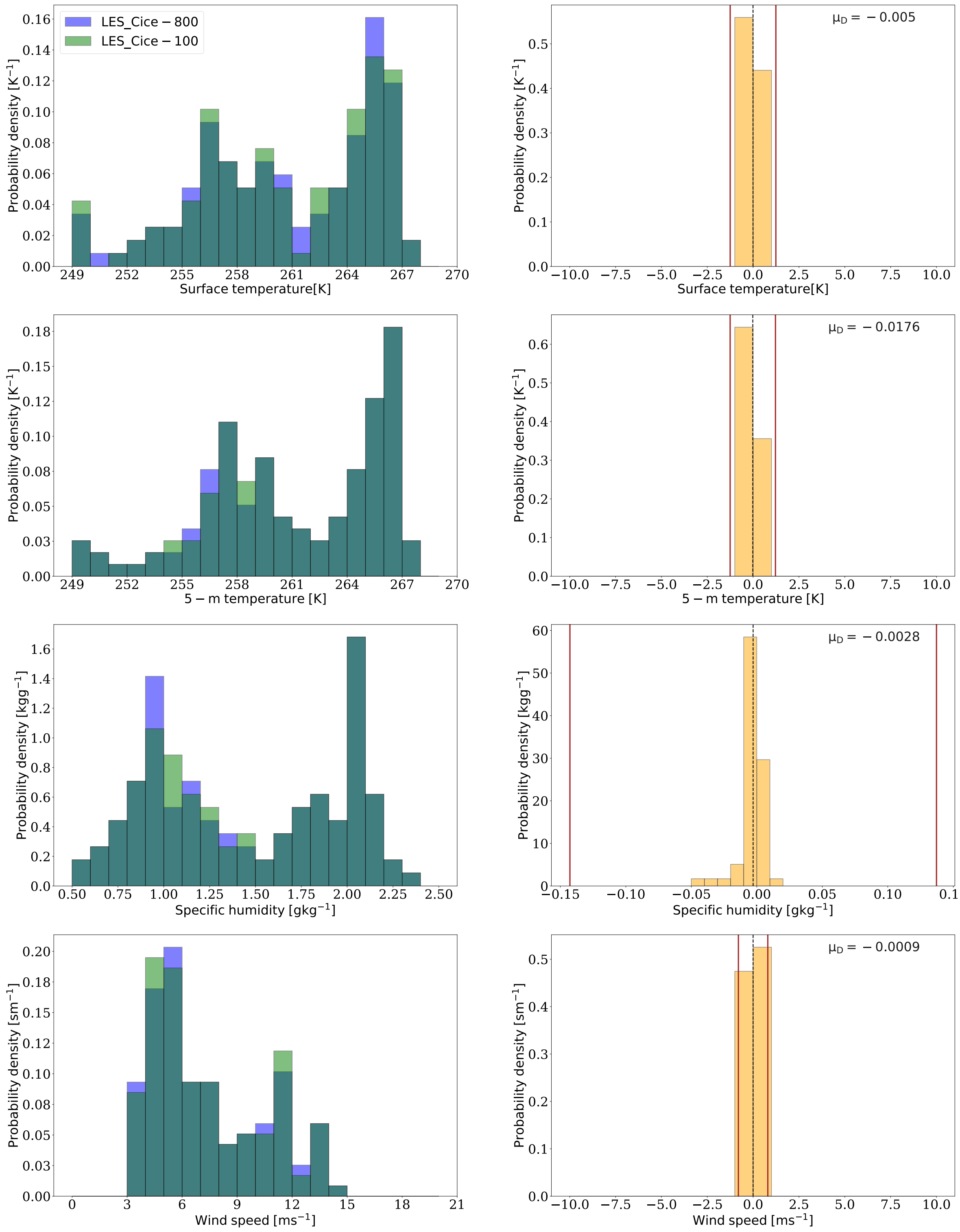

Figure 7.4: Probability density distribution (left) of sea-ice surface temperature, 5 m temperature, 5 m specific humidity, and 5 m wind speed (from top to bottom) from the simulations with LES_Cice-800 (blue) and LES_Cice-100 (green), and corresponding probability density distribution of the differences between the simulations LES_Cice-800 and LES_Cice-100 (right), based on hourly data of the period 15-21 November 2019 at the mean position of Polarstern. The dashed lines show the mean of the differences of each variable. The red lines show the 95% confidence interval.

7.2 Impact of the sea-ice scheme

During polar night the sea-ice surface is covered by snow due to cyclone events in autumn and winter (Webster et al., 2018). At MET station of the MOSAiC expedition, a snow height of around 11 cm was measured in middle of November 2019 and a snow height between 14 and 17 cm at the beginning of February 2020 (Shupe et al., 2022). The presence of snow on the sea ice is directly linked to the correlation between the sea ice and the atmosphere (Webster et al., 2018). Snow and sea ice differ by several properties, e.g. depth, density, thermal conductivity, reflectivity and albedo (Nicolaus et al., 2022). Snow is a very heterogeneous medium and one of the best insulation materials in the world (Webster et al., 2018). The average density value of sea ice varies depending on factors like temperature, salinity, and age. The mean density is $\rho_{ice} = 915\,\mathrm{kg\,m^{-3}}$ (e.g. Petty et al. (2020)). The density of snow also varies depending on factors like snow type, temperature, and compaction. On average, the mean density of freshly fallen snow ranges up to $\rho_{snow} = 300\,\mathrm{kg\,m^{-3}}$ (e.g. King et al. (2020)).

As stated in Section 4.6.5, in ICON only the reflective property of snow in terms of the albedo is accounted for but the insulating property is neglected in the calculation of the surface heat balance, leading to biases in the sea-ice surface temperature.

Lohmann (2020) showed that the response of earth's climate system to temporal variations depends on its effective heat capacity. In a coupled atmosphere-land-ocean model, the effective heat capacity of the atmosphere is described by a function of specific heat of air at constant pressure, surface pressure, and gravity acceleration. In order to account for long-term variability, like seasonality, the effective heat capacity is enhanced by a vertical mixing-layer depth dependency of the ocean. On this way, the effective heat capacity is connected to the perturbation on the timescale of the perturbation (Lohmann, 2020). In climate models, the response of the sea-ice surface temperature to changes in the atmosphere depends on the heat storage capacity of the entire ice slab. The rate of change of the sea-ice surface temperature is determined by the integral heat budget of the ice slab (see eq. 4.6.33). For a high-resolution model with very small time steps of a few seconds, the response of the sea-ice surface temperature to atmospheric changes is comparably slow by using an integral heat budget (see Section 4.6.5). Figure 7.5 shows the temporal evolution of the sea-ice surface temperature during the period 6-10 February 2020. The observations are shown together with results from the standard configuration of ICON (LES_Ctrl). Similarly, Figure 7.6 shows the corresponding comparison for the period 15-21 November 2019. In both figures, LES_Ctrl does not show the same temperature variability at the surface as was observed. The sea-ice surface temperature changes are delayed and less pronounced in the period of February 2020. Here, the modeled sea-ice surface temperature remains relatively constant throughout the considered time periods. For the period in November 2019, the temperature variability is larger. However, observed short-lived variations are not reflected by the model. One can speculate that the large differences between model and observations result from the too simple sea ice scheme consisting only one layer. A multi-layer ice model would probably improve the results. However, to date, such a model is not implemented in ICON. To overcome this limitation, a pragmatic approach is considered in the following, namely the heat capacity term in eq. 4.6.33 is modified by applying

$$C_{*i} = \frac{1}{2} - \frac{(1+\phi_*)}{12}\left(\frac{H_i}{H_{max}}\right)^{\eta_*}, \tag{7.2.1}$$

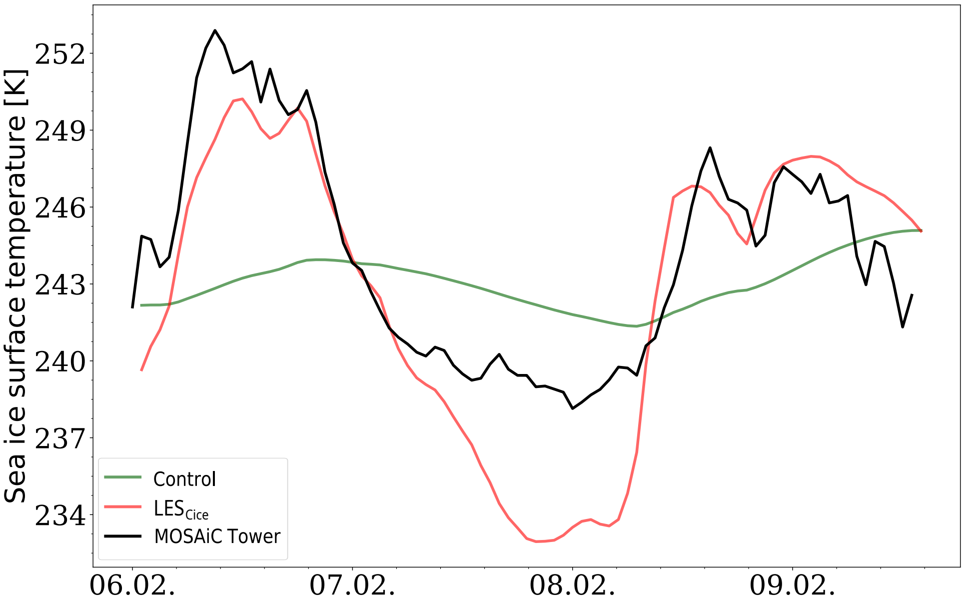

Figure 7.5: Temporal evolution of sea-ice surface temperature from LES_Ctrl (Control, green), LES_Cice (red), and MOSAiC data (black) in the period 6-10 February 2020.

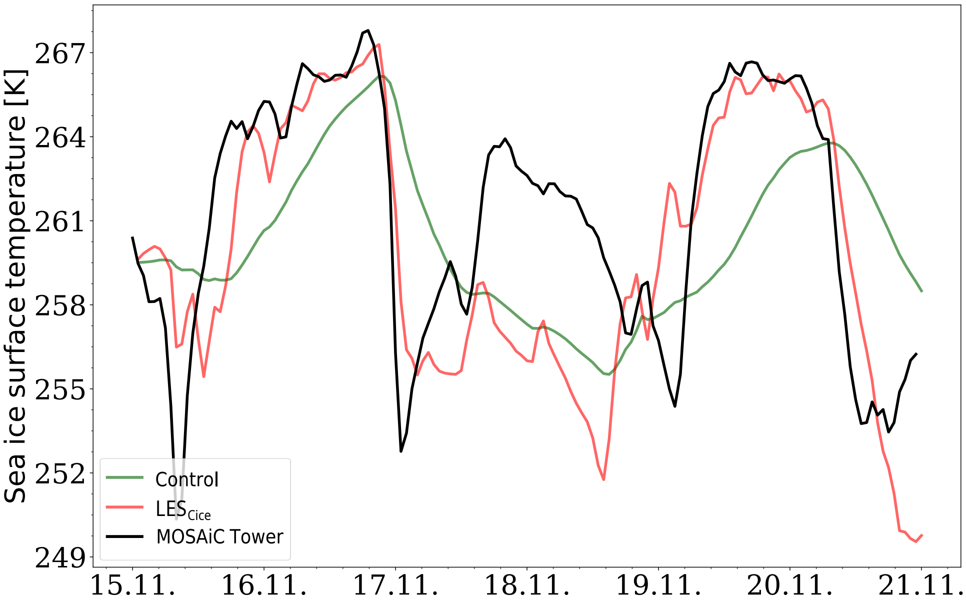

Figure 7.6: Temporal evolution of sea-ice surface temperature from LES_Ctrl (Control, green), LES_Cice (red), and MOSAiC data (black) in the period 15-22 November 2019.

with a new value for the dimensionless derived disposable parameter $\phi_* = 4.9$ and the additional exponent $\eta_* = 0.02$. Since the sea-ice shape factor parametrizes the temperature profile within the ice, a change in this factor adjusts the heat capacity indirectly. The adjustments in eq. 7.2.1 allow an increased temperature response to atmospheric variations at the sea-ice surface, while concurrently reducing the temperature response at the bottom side of the sea ice.

In Figure 7.7, the two heat capacity terms for the default implementation of the sea ice scheme and the adapted sea ice scheme are plotted against sea ice thickness. The heat capacity term from the default parametrization first increases linearly and then the growth slows down towards the maximum sea ice thickness $H_i = 3\,\mathrm{m}$. Compared to the new parameterization, the heat capacity term of the default parameterization is larger for the same sea ice thickness. The heat capacity term for the new parametrization grows slower with increasing sea ice thickness, indicating that the shape factor reaches comparably small values.

Figure 7.5 and Figure 7.6 also show the simulated sea-ice surface temperature using the modified model configuration (LES_Cice). Compared to LES_Ctrl, the impact of the adapted heat capacity term dramatically improved the model performance in LES_Cice. In particular, the sea-ice surface temperature obtained by LES_Cice shows more pronounced fluctuations in contrast to LES_Ctrl. Furthermore, the temporal evolution of the curve shows a similar behavior. Thus, LES_Cice is in better agreement with the observation.

The results show that by adjusting the sea-ice shape factor, a simple approximation can be found to more accurately reproduce temperature fluctuations that would otherwise not be represented. The solution found here is purely pragmatic in order to be able to use the simplified sea ice model for studies in the central Arctic. It does not replace the general need for a multi-layer snow cover to obtain more realistic simulation results.

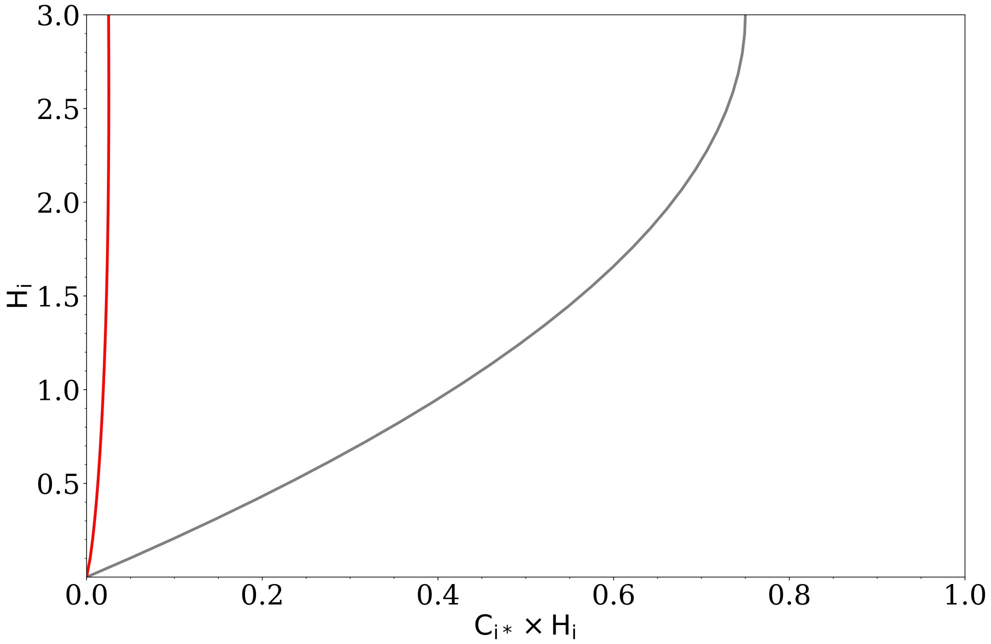

Figure 7.7: The heat capacity term $C_{*i} \times H_i$, as a function of sea-ice shape factor C_{*i} and sea ice thickness H_i, is plotted against sea-ice thickness for the default sea-ice scheme (grey) and the adapted sea-ice scheme (red) in ICON.

7.3 Impact of the lower boundary conditions

In the central Arctic, open water channels within the sea ice have a strong impact on the atmospheric boundary layer. Depending on their size, heat and moisture fluxes are induced between the ocean and the colder atmosphere which reduce the stability of the near surface atmosphere (e.g. Andreas et al., 1998; Lüpkes et al., 2008a,b; Michaelis and Lüpkes, 2022; Michaelis et al., 2021; Tetzlaff et al., 2015).

As was already described in the Experimental setup (see also Section 5), the influence of a more complex sea-ice surface structure on the near-surface temperature and vertical wind component is investigated in the following for the two weather periods in February 2020 and November 2019.

Figure 7.8 shows the modeled temporal evolution of the temperature differences $\Delta T = T(z_*) - T_s$ where $z_* = 5\,\mathrm{m}$ and index s refers to the sea-ice surface for the very cold weather condition from 6-10 February 2020. The simulation result from LES_Cice with a sea ice concentration of 100% and LES_Cice-4%lead with an area-averaged open water fraction of 4% in the sea-ice surface. Both model runs produced large values of ΔT, which points to a strongly stable stratification near the surface even in case with leads. However, as can be expected the stability is during most of the considered period reduced in the run with leads. This reduction is especially large around 8th February with more than 1 K difference. But there are also some periods with almost no change or even increase of thermal stability. During the course of the simulation period, LES_Cice shows slightly larger temperature differences than LES_Cice-4%lead for the lowest atmospheric levels. For most of the period, the temperature differences from LES_Cice and from LES_Cice-4%lead do not differ by more than about 0.5 K.

Figure 7.9 shows the temporal evolution of the vertical temperature difference ΔT from

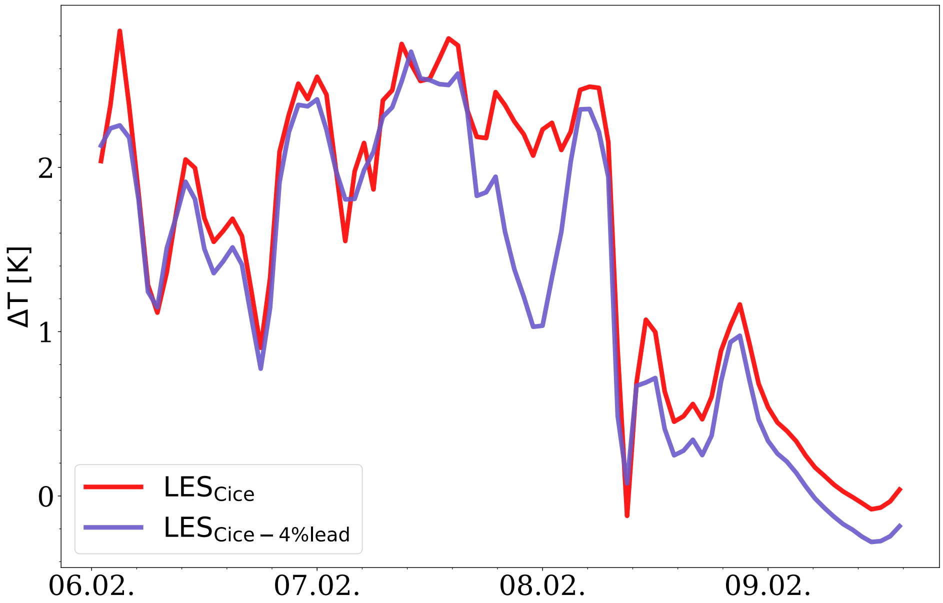

Figure 7.8: Temporal evolution of the temperature difference ΔT from 6-10 February 2020 with values averaged over the whole domain. The simulation results of LES_Cice (red) with a sea ice concentration of 100% are compared to the simulation results with an area-averaged open water fraction of 4% imitating leads in LES_Cice-4%lead (blue).

LES_Cice with a sea ice concentration of 100% and LES_Cice-6%lead with an area-averaged open water fraction of 6% obtained during the storm period from 15-21 November 2019. Both simulation results show positive temperature differences during the days were the storms passed the area and negative temperature differences between those weather periods. The temperature differences near the surface from LES_Cice are a bit larger than from LES_Cice-6%lead. The largest difference between LES_Cice and LES_Cice-6%lead is shown between 17 and 19 November. However, for the rest of the weather period, the difference between LES_Cice and LES_Cice-6%lead are comparably small.

The analysis of the temperature difference shows how the presence of leads, or open water channels, affects the simulated temperature near the surface for two different weather periods during the Arctic winter. The stable stratification of the atmosphere can be weakened on certain simulated days. The results also show that the effect of leads may not be consistently substantial and may be limited in magnitude during different periods, depending on the simulated weather condition. Nevertheless, the inclusion of open water channels leads to an increase in the variability of the near-surface temperature for the stably stratified atmosphere. Especially the comparison for November 2019 shows that the temperature differences change considerably with slightly higher open water concentration. Furthermore, the extent to which the leads affect the simulated atmospheric boundary layer also depends on a large number of other factors such as the size distribution of the channel, or wind speed and direction height of the boundary layer and its stratification in the inflow region.

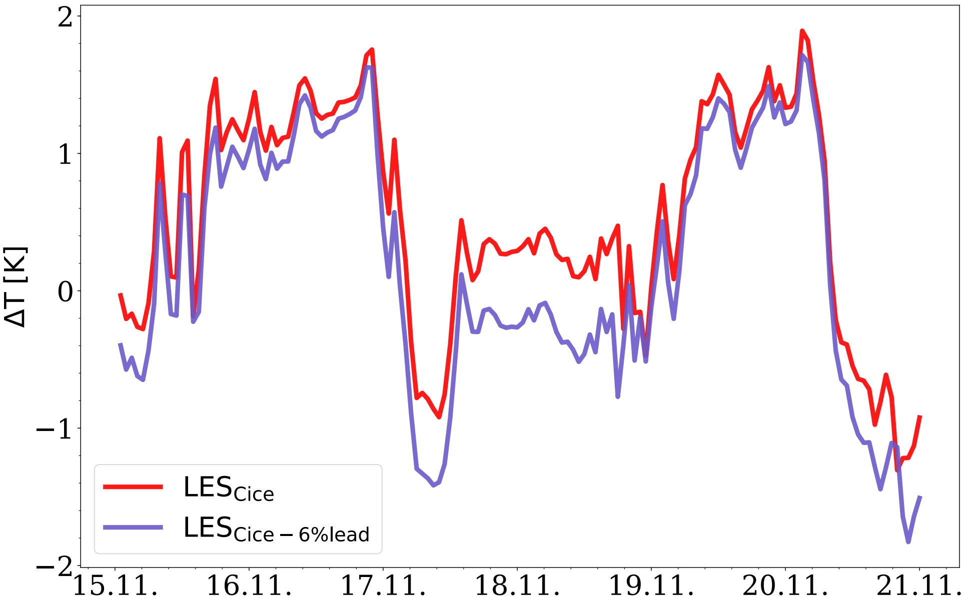

Figure 7.9: Temporal evolution of the temperature difference ΔT from 15-21 November 2019 with values averaged over the whole domain. The simulation results of LES_Cice (red) are compared to the simulation results with an open water fraction of 6% imitating leads in LES_Cice-6%lead (blue).

In the following, the effect of the different surface boundary conditions and the used grid size is studied in more detail. The focus is on the modeled boundary layer structure with respect to temperature, wind and circulations in the inner model domain. To demonstrate the differences in vertical circulation, a time period with continuous horizontal wind speed and direction is selected. The 17th of November 2019, 29 h, is chosen, because the timing falls within an interesting period where the differences between LES_Cice-100 and LES_Cice-800-6%lead (Figure 7.9) were the largest. Figure 7.10 shows the modeled temperature and wind vectors at 5 m height for the selected time, when cold air advection near the surface in the nested areas was directed from north to south (left panel). In the following, results of different model runs are compared differing by the prescribed open water fraction (in percent). Cases with closed sea cover are considered, LES_Cice-800 and LES_Cice-100 (100% sea ice cover), as well as cases with 6% open water (domain average), LES_Cice-800-6%lead and LES_Cice-100-6%lead. The surface boundary condition for the latter case is shown in Figure 7.10 (right panel). A vertical cross-section is taken through the innermost model domain in both panels of Figure 7.10. The intersection line is along the wind direction of the horizontal wind from 86.2318°N to 86.0818°N, corresponding to the domain with a diameter of 17.5 km (see Table 5.2 for horizontal grid size of 100 m).

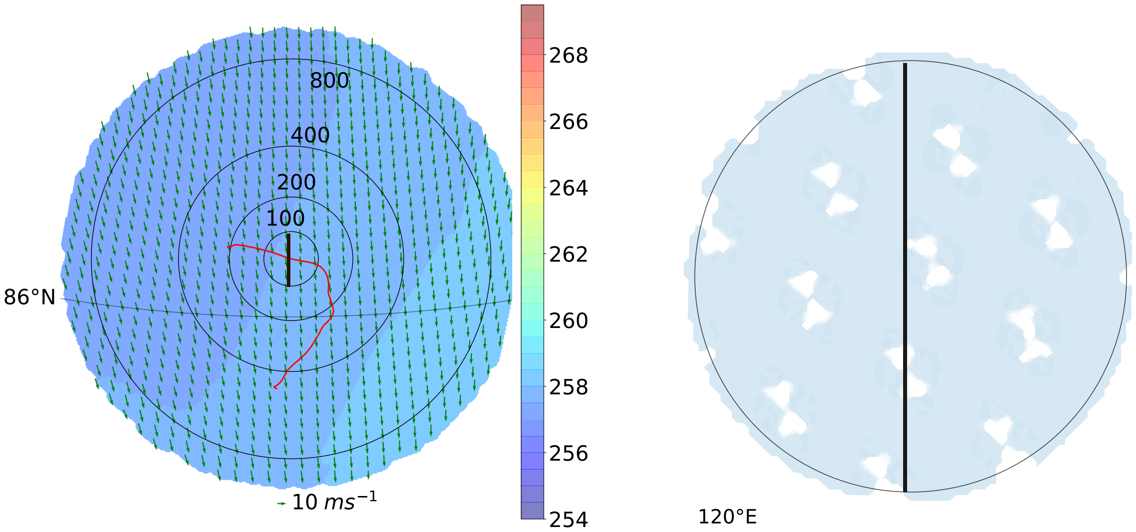

Figure 7.10: Horizontal cross-sections showing temperature (left panel) at 5 m above the surface on 17 November 2019, 20 h. The circles illustrate schematically the model domains with horizontal grid sizes of 800 m, 400 m, 200 m, and 100 m, respectively. The red line marks the drift track of RV Polarstern from 15 to 17 November 2019. The green vectors show wind speed and wind direction. The light-blue area refers to 100% sea ice cover whereas white means 100% open water. The thick black line through the center of the LES domain (in both panels) marks the position of the vertical cross-sections shown in Figures 7.12-7.14. The section is taken from 86.0818°N and 86.2318°N (in flow direction of the meridional wind v).

A north-south vertical cross-section of the temperature as a function of altitude to 400 m above ground level is presented in Figure 7.11. The results are obtained from LES_Cice-100-6%lead on 17 November, 20 h. The values of temperature decrease with increasing height until a capping inversion is reached between 300 m and 400 m.

In order to further understand the changes in the vertical circulation patterns of the wind within the boundary layer, differences of the results between model runs using horizontal grid sizes of 100 m and 800 m, and between model runs with 100% sea ice cover and with open water fraction of 6% on the sea-ice surface are evaluated. Horizontal and vertical cross-sections of the vertical wind minus their mean values (horizontal and vertical boundary layer mean), and of the temperature are shown in Figures 7.12-7.14. These figures provide additional insights into the impact of these different conditions on

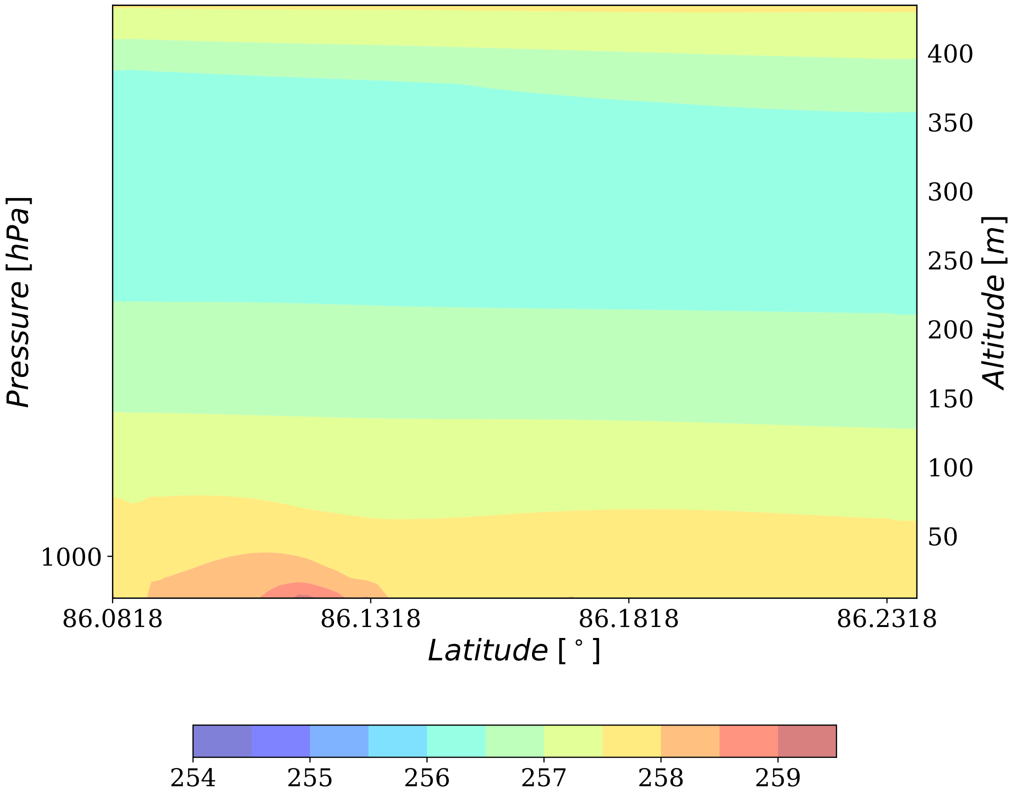

Figure 7.11: Vertical cross-section of temperature for the lowermost 400 m along the black line of Figure 7.10 on 17 November, 20 h from LES_Cice-100-6%lead.

wind and temperature distributions within the boundary layer.

Figure 7.12 shows the vertical cross-section of the temperature as a function of altitude up to 100 m above ground level from LES_Cice-800, LES_Cice-100, LES_Cice-800-6%lead, and LES_Cice-100-6%lead on 17 November, 20 h. In each experiment, the temperature exhibits a decrease with height in the lowest 100 m. However, in the results from LES_Cice-800-6%lead and LES_Cice-100-6%lead the atmosphere over the surface is warming where the considered cross-section is passing an open water channel that is located between 86.0818°N and 86.1318°N. The water channel affects the near-surface temperature. However, the plumes do not reach the capping inversion layer, because the effect of the plume is small on the temperature due to the small size of the lead. The warming effect is larger for LES_Cice-100-6%lead than for LES_Cice-800-6%lead. Both plumes reach heights between 30 m and 40 m above ground (see also Figure 7.11).

The influence of plumes is reflected by the overall circulations, as documented by the vertical cross-section of wind speed from LES_Cice-800, LES_Cice-100, LES_Cice-800-6%lead, and LES_Cice-100-6%lead for the above mentioned period in Figure 7.13. To investigate changes in the wind field for a relatively small domain, the difference between the total wind and the mean wind is shown for each model layer. The residual

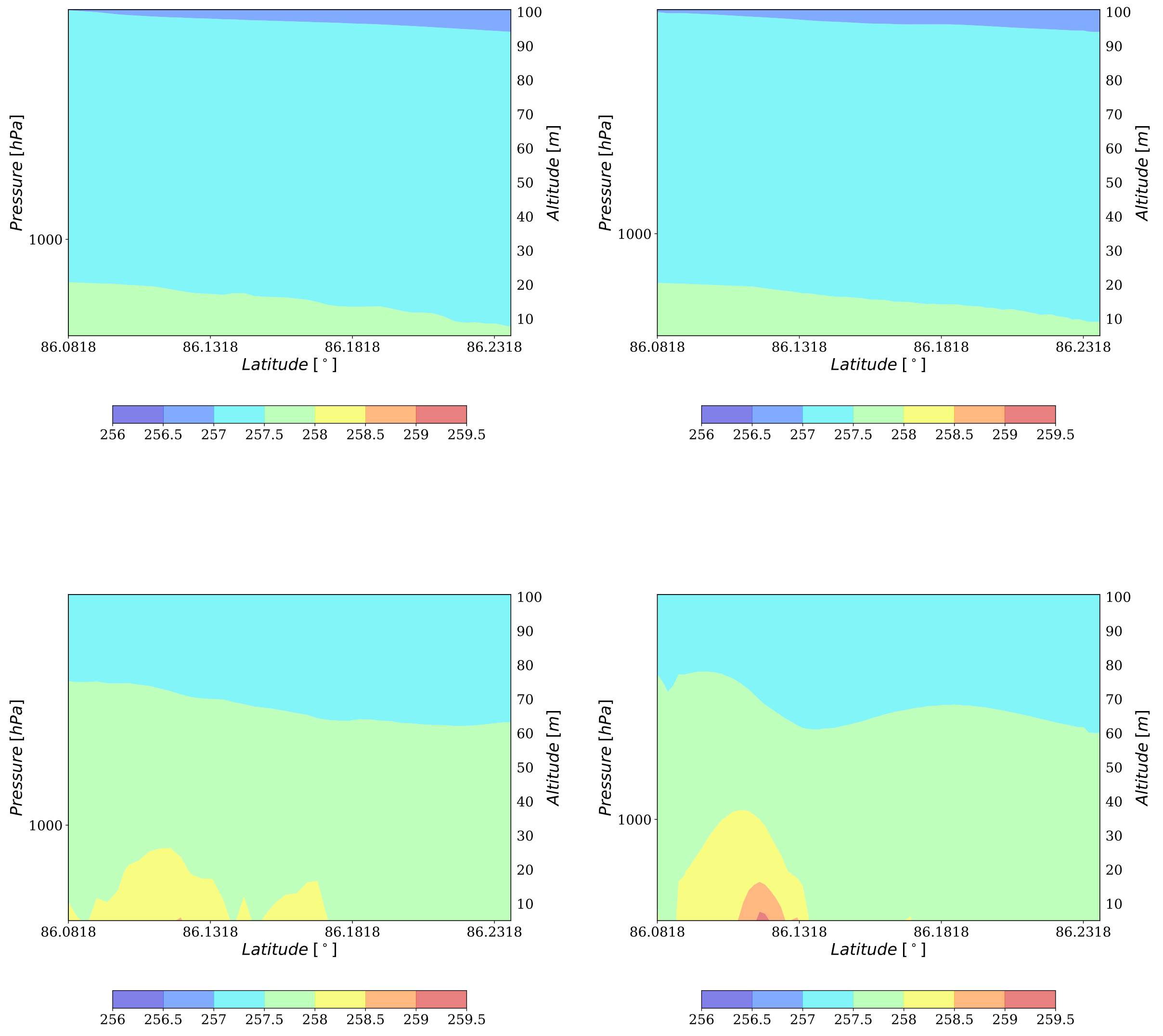

Figure 7.12: Vertical cross-section of temperature for the lowermost 100 m along the black line of Figure 7.10 in 17 November, 20 h. Shown are experiments with 100,% covered sea-ice concentration LES_Cice-800 (left top), and LES_Cice-100 (right top), as well es experiments with an averaged open water concentration amount of 6% LES_Cice-800-6%lead (left bottom), and LES_Cice-100-6%lead (right bottom).

circulation over the mean wind, which does not correspondent to a physical circulation, is thereby obtained. All experiments exhibit similar values for the difference between total wind and mean wind. However, a slight change in the wind circulation near the surface is observed in LES_Cice-800-6%lead and in LES_Cice-100-6%lead, as revealed by the difference between the total wind and the mean wind. Moreover, as the horizontal resolution increases, the circulation pattern of the vertical wind becomes more complex in experiments with an averaged open water fraction of 6%.
Note that in Figure 7.13 vertical wind is directed upward in some regions and downward in other regions but not all labels of contour lines are given for technical reasons.

Figure 7.14 shows the horizontal cross-sectional view of the temperature at 100 m above

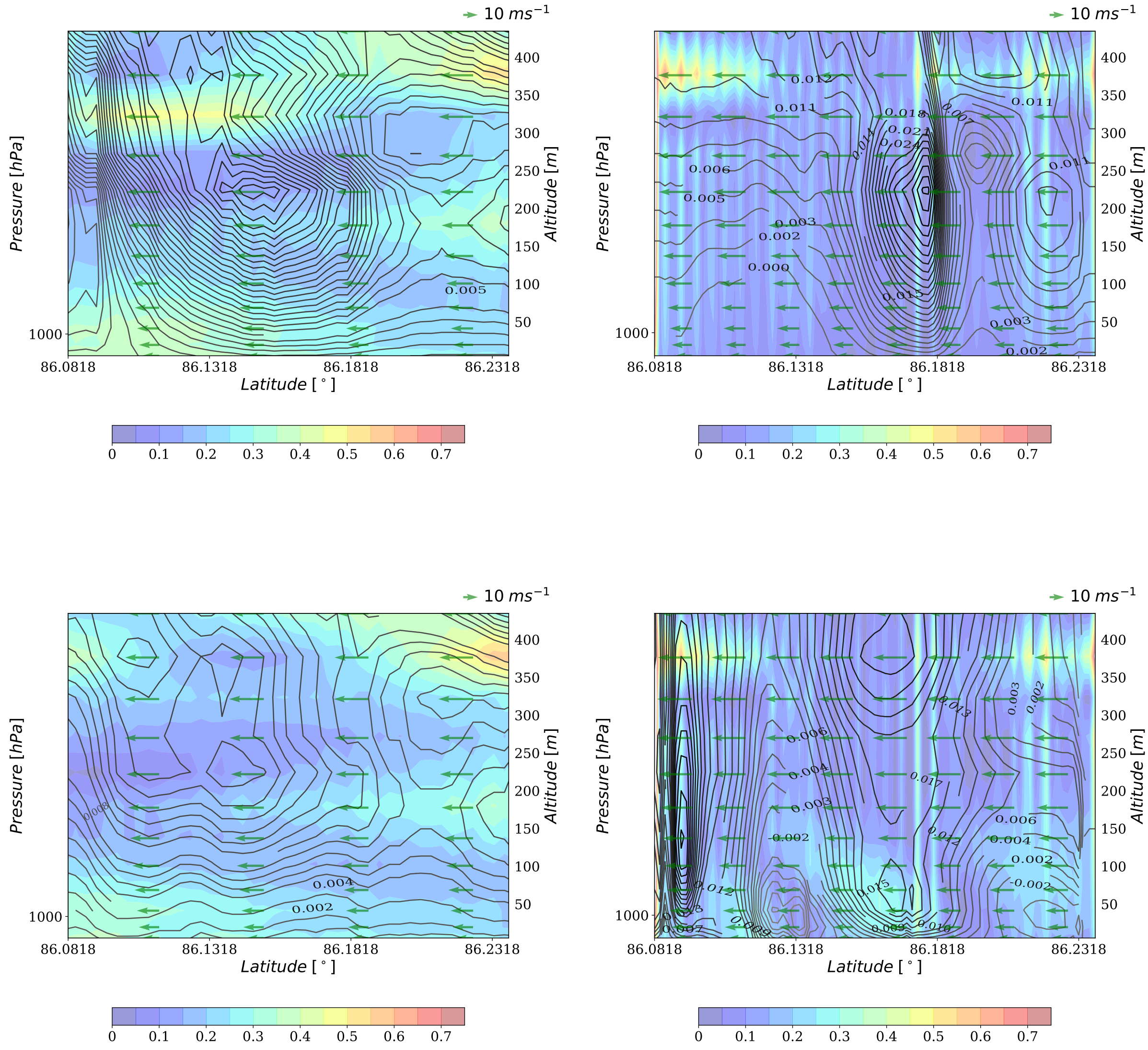

Figure 7.13: Vertical cross-section along the black line shown in Figure 7.10 from LES_Cice-800, LES_Cice-100, LES_Cice-800-6%lead, and LES_Cice-100-6%lead. Black contour lines represent vertical wind. Colored horizontal areas show the mesoscale wind (total wind minus mean wind in ms^{-1}). Vectors refer to horizontal wind (again the difference between total wind and mean wind).

ground level for LES_Cice-800, LES_Cice-100, LES_Cice-800-6%lead, and LES_Cice-100-6%lead. In addition, the contour lines represent the vertical wind speed, while the green vector dots show the difference between horizontal wind speed and horizontal mean wind speed. At 100 m height above ground, the temperature from LES_Cice-800 and LES_Cice-100 is around 1 K colder compared to LES_Cice-800-6%lead and LES_Cice-100-6%lead, except for a region located south-east of each domain. Regions with down- and upward winds on the left side of the domain are present in all cases, with a more pronounced circulation observed in simulations with 100% sea ice cover. In LES_Cice-800, an additional upward wind is visible in the center of the domain that is less pronounced for the other experiments. Due to the open water channels, the vertical wind differs for LES_Cice-800-6%lead and LES_Cice-100-6%lead, with noticeable increase in the amount of the up- and downward winds in LES_Cice-100-6%lead. To determine whether this pattern indeed corresponds to reality, and weather it is located in the lee of the open water channels, a higher horizontal resolution is required.

Studies comparing mesoscale model results to those from typical LES models have shown that temperature changes over open water channels can be very small dependent, e.g. on lead width and boundary layer height (see e.g. Lüpkes et al. (2008a), Vihma et al. (2014)). However, the presence of leads has a strong impact on the surrounding turbulent fluxes and thus, on the wind field. Especially, the integrated effect of a series of leads should not be neglected, particularly in a stably stratified atmospheric boundary layer. To model the impact of leads in larger details a much smaller grid size than the one used here would be required. Increasing resolution would reveal even more complex circulation structures. Alternatively, turbulence parametrizations especially adjusted to leads would be required. But runs with higher resolution are beyond the present investigation and the addressed turbulence parametrization exist up to now only for leads with simplified geometry. However, the addressed studies by (Lüpkes et al., 2008a,b; Michaelis and Lüpkes, 2022; Michaelis et al., 2021) show that the overall development of atmospheric processes over leads and first order effects can be reproduced also by coarser resolution models applying more simple parameterizations like those used here.

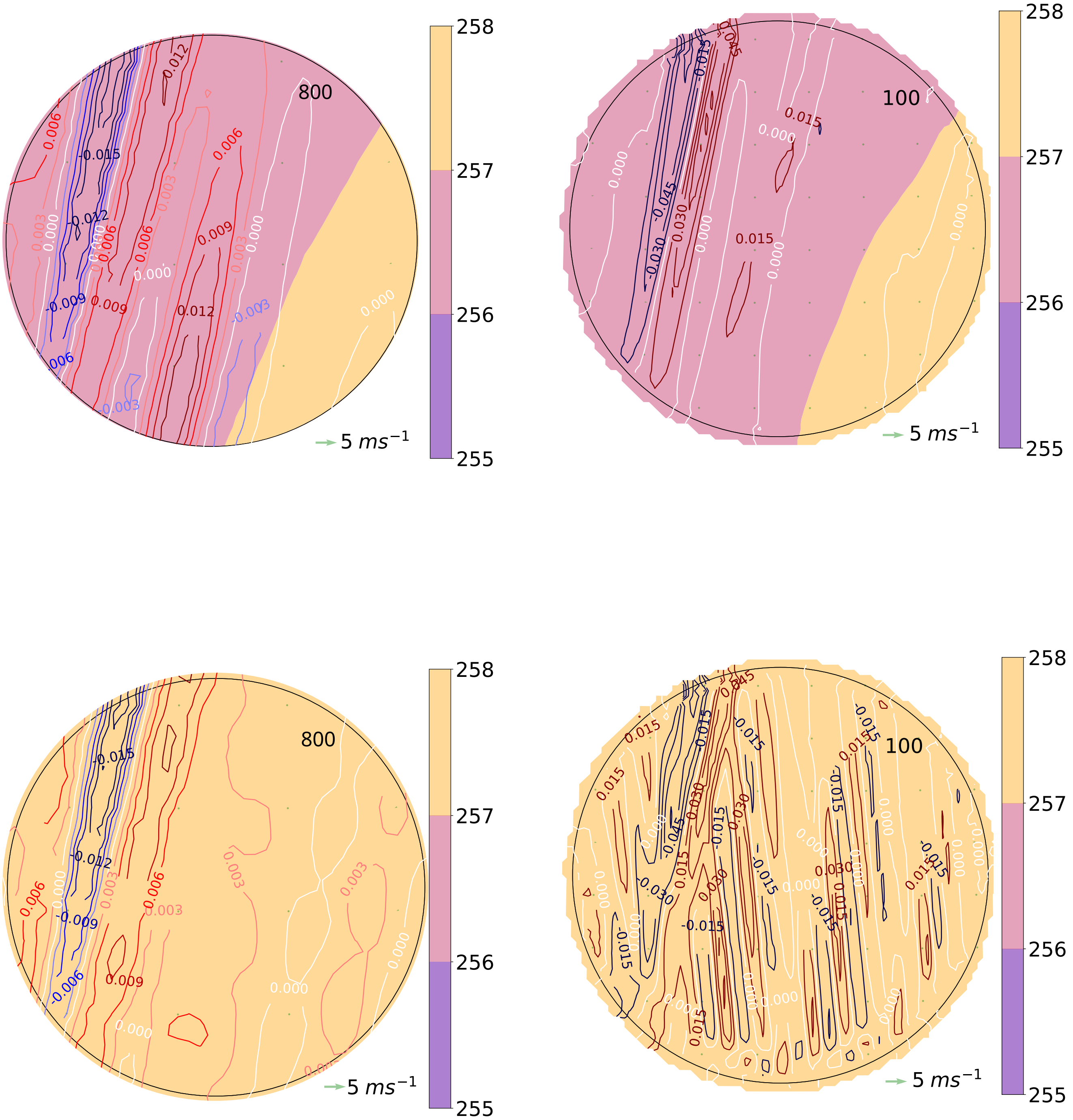

Figure 7.14: Horizontal cross-section of temperature at 100 m above ground level from LES_Cice-800, LES_Cice-100, LES_Cice-800-6%lead, and LES_Cice-100-6%lead. Colored lines indicate vertical wind speed, vectors refer to the horizontal wind speed and direction (total horizontal wind minus mean wind).

7.4 Impact of the parametrization schemes under cold, light wind conditions

During polar night, the Arctic atmosphere near the surface is mostly stably stratified. For the investigations of the atmospheric boundary layer near the surface, a clear sky, very cold weather period in February 2020 is chosen and compared to observational data. The simulation results of three different experiments are presented in this section.

7.4.1 Near-surface variables

To evaluate the model performances in the lower atmospheric boundary layer in the central Arctic during polar night, the basic meteorological variables, i.e. temperature at sea-ice surface and air temperature at 5 m, specific humidity and wind speed, are compared against MOSAiC observations. Figure 7.15 shows the temporal evolution of the observed and the simulated temperature in the lowermost 500 m for the clear-sky period. The comparison shows that the model reproduces the observed temporal evolution of relatively warm and cold temperatures. The observed stably stratified atmospheric layer near the surface between 7-10 February 2020 is captured by the simulation, with very low temperatures near the surface and increasing temperatures with height. However, the values for the simulation are colder compared to the observations, except for the end of the period. The observed warmer phase at the beginning of the period between 6-7 February is less pronounced in the simulation. Instead, a colder layer is taken shape in 6 February.

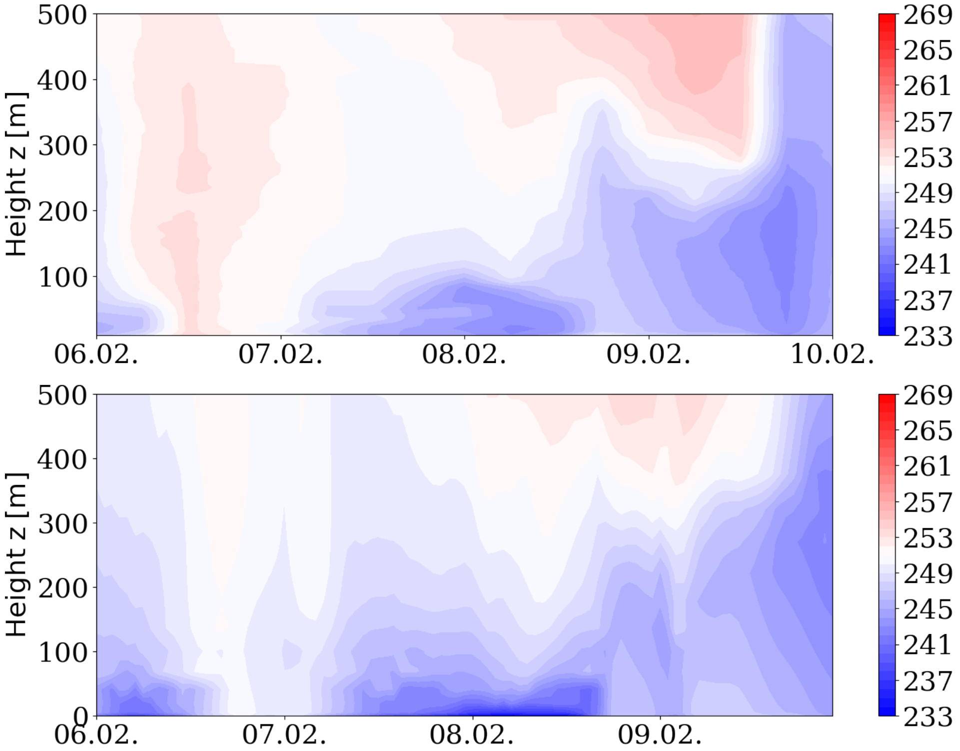

Figure 7.15: Height-time cross section of the temperature in the lowermost 500 m from 6-hourly radiosonde data (above) and from LES_Ctrl (below) for the period 6-10 February 2020.

Figure 7.16 shows the temporal evolution of the sea-ice surface temperature, air temperature at 5 m, specific humidity and wind speed from LES_Ctrl, LES_Cice, NWP_Cice, and MOSAiC data during the clear-sky period in 6-10 February 2020. The observations show a phase of a relatively warm temperature between 6-7 February, where the observed temperatures near the surface increase up to 10 K and the observed specific humidity rises almost around 0.5 $\mathrm{g\,kg^{-1}}$. Observed wind speed is between 4 and 6 $\mathrm{m\,s^{-1}}$. Between 7-9 February the temperatures close to the surface decrease rapidly by more than 10 K to values around 240 K for sea-ice surface temperature and around 242 K for air temperature at 5 m. A similar decrease is observed for specific humidity and wind speed. Between 8-9 February the variables near the surface increase again until the end of the simulation period.

The sea-ice surface temperature, the air temperature at 5 m and the specific humidity at 5 m show only little variation in LES_Ctrl. As was discussed in Section 7.2, the response to changes in the atmosphere background state appears to be slow compared to the observations. The response is clearly faster in LES_Cice and in NWP_Cice and in reasonable agreement with the observations. However, during the very cold period with stable stratification between 7-9 February, temperatures are too cold in LES_Cice. The sea-ice surface temperature is up to 6 K and the air temperature up to 4 K lower than the observations. The sea-ice surface temperature in NWP_Cice is closer to the observation and differs only around 1 K to 2 K. Additionally, the sea-ice surface temperature in NWP_Cice-3km is shown in Figure 7.16. Compared to the other simulations with new sea-ice surface parameterization, the coarser model result shows lower temperatures at the beginning of the simulation period in 6-7 February 2020, but similar temperatures as NWP_Cice on 7-10 February 2020.

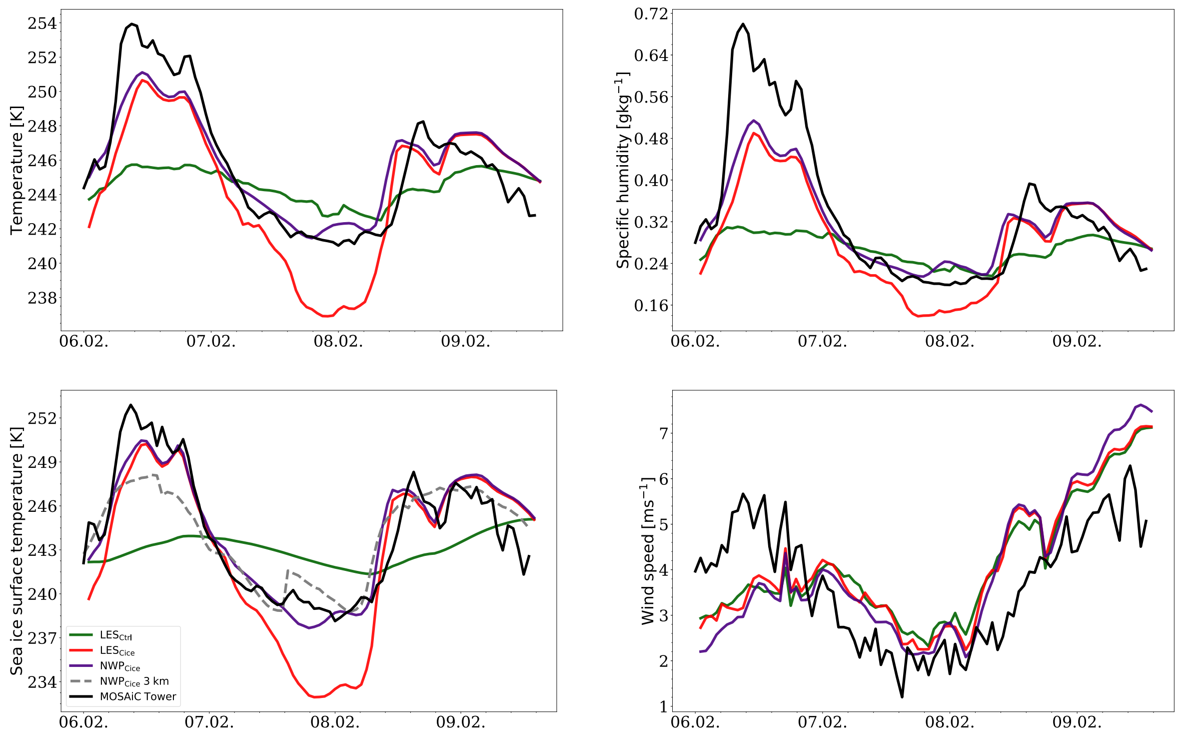

Figure 7.16: Temporal evolution of air temperature at 5 m (upper left), sea-ice surface temperature (lower left), specific humidity at 5 m (upper right), and wind speed at 5 m (lower right) from LES_Ctrl (green), LES_Cice (red), NWP_Cice (violet), NWP_Cice-3km (dashed grey), and MOSAiC data (black) in the period 6-10 February 2020.

The temporal evolution of specific humidity at 5 m also shows stronger fluctuations in

Variable	μ_{obs}	s_{obs}	μ_{ctrl}	s_{ctrl}	ν	t'	p	μ_D
Surface temperature [K]	244.26	4.23	243.09	1.02	93.73	2.59	0.01	**1.16**
5 m temperature [K]	245.52	3.68	244.66	0.99	96.09	2.18	0.03	**0.86**
specific humidity [$\mathrm{g\,kg^{-1}}$]	0.327	0.136	0.272	0.03	92.15	3.83	0.0	**0.06**
wind speed [$\mathrm{m\,s^{-1}}$]	3.84	1.35	4.18	1.35	168	-1.65	0.10	0.33

Table 7.3: Statistical values of different meteorological variables on 6-10 February 2020. Listed are the mean value μ_{obs} and the standard deviation s_{obs} from the observation, the mean value μ_{ctrl} and the standard deviation s_{ctrl} from LES_Ctrl, as well as their mean value of the differences μ_D. Bold values highlight the difference between model and observation. The results of the statistical t-test include the number of degrees of freedom ν, the t-value t', and the p (probability that the null hypothesis is correct). The sample sizes are $n_1 = n_2 = 85$.

LES_Cice and in NWP_Cice than in LES_Ctrl. The values of both experiments fairly agree with the observations for the last three days of the period. However, during the very cold period between 7-8 February, the values are underestimated in LES_Cice by around $0.08\,\mathrm{g\,kg^{-1}}$. On the relatively warm day on 6 February, the values of specific humidity are around $0.09\,\mathrm{g\,kg^{-1}}$ to $0.2\,\mathrm{g\,kg^{-1}}$ lower in LES_Cice and NWP_Cice compared to the observations.

The temporal evolution of wind speed at 5 m from all experiments shows that the simulations with adapted sea-ice surface parameterization do not differ from those without adaptation. The values in all experiments are slightly overestimated by $1\,\mathrm{m\,s^{-1}}$ to $2\,\mathrm{m\,s^{-1}}$, which is a commonly known issue in near-surface modeling (Maronga et al., 2020).

Table 7.3 presents statistical values of the observations and LES_Ctrl during the period of 6-10 February 2020. The Welch's t-test (Equations 7.1.1-7.1.5) indicates that the differences between LES_Ctrl and the observations are statistically significant for surface temperature, 5-m temperature, and specific humidity, while the mean values for wind speed statistically agree.

The probability density distribution for the meteorological variables from observations and LES_Ctrl and their corresponding probability density distribution of the differences between observations and LES_Ctrl are shown in Figure 7.17. The probability density distribution of the differences between observations and LES_Ctrl is calculated by subtracting the mean values from the model from the mean values from the observation. Compared to the observations, LES_Ctrl shows lower variations for all variables. Also, the probability density distribution of the differences shows large deviations between observations and LES_Ctrl. Note that, positive values refer to higher values in the observation and negative values refer to higher values in the simulation.

The probability density distribution for the simulated sea-ice surface temperature shows values in the range from 241 K to 246 K, whereas the observed sea-ice surface temperature is distributed between 237 K and 254 K.

Similar to the sea-ice surface temperature, the probability density distribution for the simulated air temperature at 5 m shows values between 242 K and 246 K, while the probability density distribution of the observed air temperature at 5 m ranges from 241 K to 255 K. Just like for the sea-ice surface temperature, the probability density distribution of the differences between observation and LES_Ctrl shows large mean deviations between simulated and observed temperatures with a large underestimation of the observation of around 9 K by the model.

The simulated probability density distribution for specific humidity at 5 m air shows also

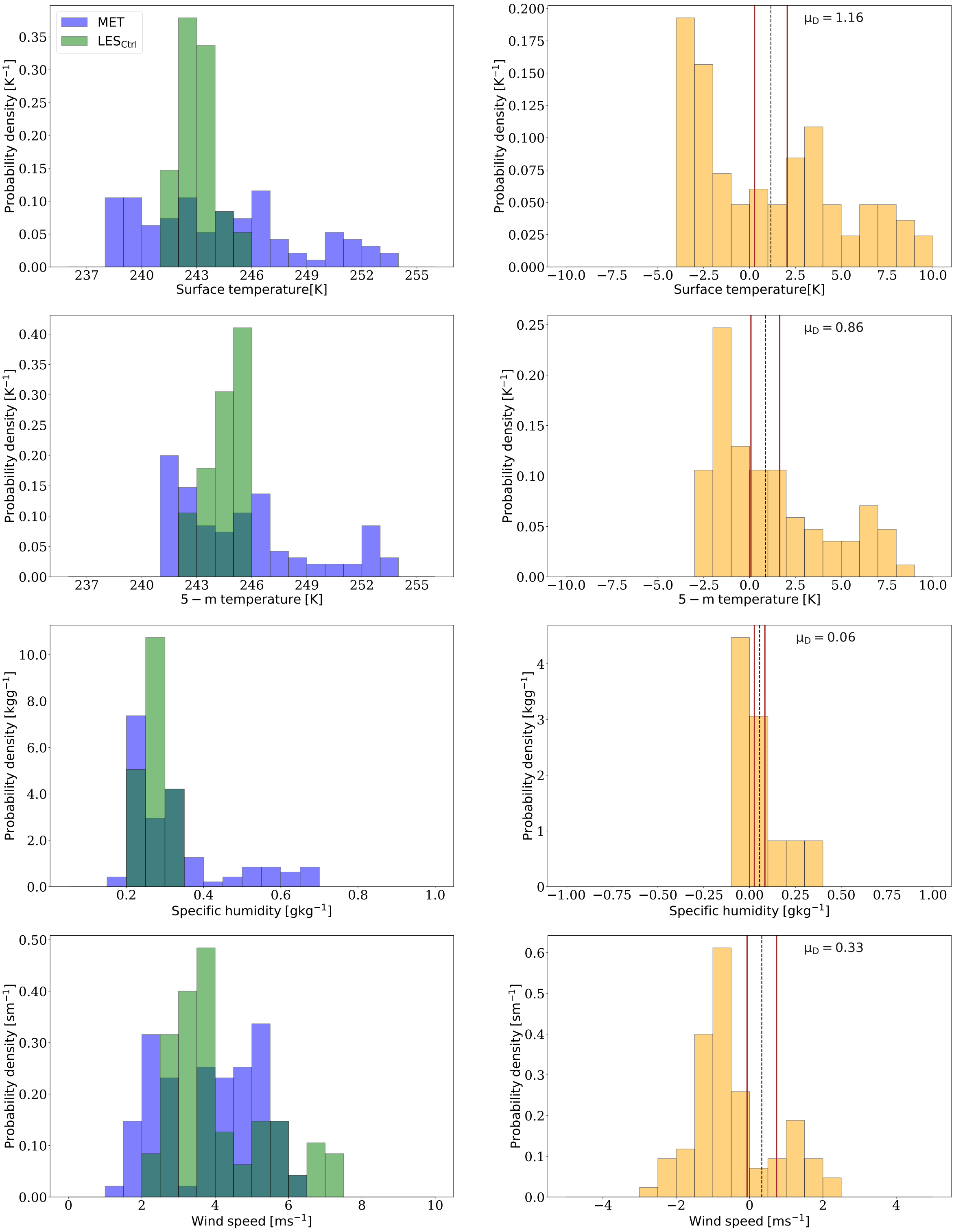

Figure 7.17: Probability density distribution (left) of sea-ice surface temperature, air temperature at 5 m, specific humidity at 5 m, and wind speed at 5 m (from top to bottom) from LES_Ctrl (green) and MOSAiC data (blue), as well as the corresponding probability density distribution of the differences between the simulations and observations (right), based on hourly data of the period in 6-10 February 2020 at the mean Polarstern position. The dashed lines show the mean of the differences of for each variable. The red lines show the 95% confidence interval.

Variable	μ_{obs}	s_{obs}	μ_{Lcice}	s_{Lcice}	ν	t'	p	μ_D
Surface temperature [K]	244.26	4.23	242.91	5.61	156.18	1.80	0.07	1.35
5 m temperature [K]	245.52	3.68	244.42	4.09	166.16	1.89	0.06	1.10
specific humidity [$\mathrm{g\,kg^{-1}}$]	0.327	0.136	0.29	0.096	151.1	2.11	0.04	**0.04**
wind speed [$\mathrm{m\,s^{-1}}$]	3.84	1.35	4.17	1.46	166.98	-1.54	0.13	-0.32

Table 7.4: Statistical values of different meteorological variables on 6-10 February 2020. Listed are the mean value μ_{obs} and the standard deviation s_{obs} from the observation, the mean value μ_{Lcice} and the standard deviation s_{Lcice} from LES_Cice, as well as their mean value of the differences μ_D. Bold values indicate that the difference between model and observation. The results of the statistical t-test include the number of degrees of freedom ν, the t-value t', and the p (probability that the null hypothesis is correct). The sample sizes are $n_1 = n_2 = 85$.

lower variations than the observed probability density distribution. The simulated values are mostly between 0.2 $\mathrm{g\,kg^{-1}}$ and 0.3 $\mathrm{g\,kg^{-1}}$, where as the observed ones are ranging between 0.1 $\mathrm{g\,kg^{-1}}$ and 0.7 $\mathrm{g\,kg^{-1}}$.

The simulated probability density distribution for wind speed at 5 m ranges between 2 $\mathrm{m\,s^{-1}}$ and 7.5 $\mathrm{m\,s^{-1}}$, while the observed one ranges between 1 $\mathrm{m\,s^{-1}}$ and 6.5 $\mathrm{m\,s^{-1}}$. Simulated wind speeds are more broadly distributed similarly as the observation. However, most of the modeled values are located between 2 and 4 $\mathrm{m\,s^{-1}}$, whereas the observation is more evenly distributed between 2-6 $\mathrm{m\,s^{-1}}$. Additionally, the simulated wind speed does not reach values lower than 2 $\mathrm{m\,s^{-1}}$ as was observed the observation. The corresponding probability density distribution of the differences shows that the model underestimates the observed high wind speeds, but also overestimates the observed low wind speeds.

The simulated sea-ice surface temperature, air temperature at 5 m and specific humidity in LES_Ctrl show low variability in their values compared to the observation. The default setting in ICON-LEM has difficulties to change according to the observed changes in near surface variables, except wind speed.

Table 7.4 shows the means, standard deviations, and Welch t-test results for the meteorological variables obtained from observation and LES_Cice during the period of 6-10 February 2020. Contrary to the results obtained for the comparison between observation and LES_Ctrl (Table 7.3), the mean values of the differences for sea-ice surface temperature and air temperature at 5 m show no significant difference between observation and LES_Cice, except for specific humidity.

Figure 7.18 shows the probability density distribution from LES_Cice and the observations and the probability density distribution of the differences between observations and LES_Cice. Compared to the results from LES_Ctrl (Figure 7.17), the probability densities of near-surface temperatures and specific humidity from LES_Cice show a wider range of values and thus agree better with the observations. Only the probability density distribution for wind speed is similar to LES_Ctrl.

The probability density distribution for the simulated sea-ice surface temperature shows values between 236 K and 251 K, while the one from the observations ranges from 237 K to 254 K. LES_Cice underestimates the higher and lower values compared to the observation (see also Figure 7.16). The modeled lower sea-ice surface temperature and air temperature at 5 m refer to the strong underestimation of the temperature on 7-9 February. The model shows higher temperature between 246 K and 247 K, attributable to overestimated temperatures at the end of the simulation period. The probability density distribution of the differences between observation and LES_Cice shows smaller mean deviations than

Variable	μ_{obs}	s_{obs}	μ_{Ncice}	s_{Ncice}	ν	t'	p	μ_D
Surface temperature [K]	244.26	4.23	244.41	4.01	167.52	-0.23	0.82	-0.14
5 m temperature [K]	245.52	3.68	245.87	2.76	155.78	-0.73	0.47	-0.35
specific humidity [$\mathrm{g\,kg^{-1}}$]	0.327	0.136	0.319	0.08	135.91	0.51	0.61	>0.0
wind speed [$\mathrm{m\,s^{-1}}$]	3.84	1.35	4.13	1.64	162.02	-1.25	0.21	-0.28

Table 7.5: Statistical values of different meteorological variables on 6-10 February 2020. Listed are the mean value μ_{obs} and the standard deviation s_{obs} from the observation, the mean value μ_{Ncice} and the standard deviation s_{Ncice} from NWP_Cice, as well as their mean value of the differences μ_D. The results of the statistical t-test include the number of degrees of freedom ν, the t-value t', and the p (probability that the null hypothesis is correct). The sample sizes are $n_1 = n_2 = 85$.

between observation and LES_Ctrl (Figure 7.17).

Just like sea-ice surface temperature, the probability density distribution for air temperature at 5 m from LES_Cice ranges from 236 K to 251 K, while the probability density distribution from the observation ranges from 241 K and 255 K. The model underestimates the highest and lowest air temperatures compared to the observation. A slight overestimation from LES_Cice compared to the observation is between 247 K and 251 K. This is again related to the end of the simulation period, where the model overestimates the air temperature.

The probability density distribution for the simulated specific humidity at 5 m from LES_Cice shows values between 0.1 $\mathrm{g\,kg^{-1}}$ and 0.5 $\mathrm{g\,kg^{-1}}$ and the observed one ranges from 0.15 $\mathrm{g\,kg^{-1}}$ to 0.7 $\mathrm{g\,kg^{-1}}$. Similar to the temperature, the simulated specific humidity at 5 m underestimates the higher values compared to the observation.

The simulated probability density distribution for wind speed at 5 m from LES_Cice ranges from 2 $\mathrm{m\,s^{-1}}$ to 7.5 $\mathrm{m\,s^{-1}}$, whereas the observed one ranges from 0.5 $\mathrm{m\,s^{-1}}$ to 7 $\mathrm{m\,s^{-1}}$. The simulated wind speed from LES_Cice is similar to the one from LES_Ctrl. Lower wind speeds are overestimated and the highest mean deviation is found at around 3 $\mathrm{m\,s^{-1}}$.

As the adapted sea-ice surface parametrization does affect the sea-ice surface temperature, mostly the simulated near-surface temperatures and specific humidity are influenced and show differences between LES_Cice and LES_Ctrl. The differences between the observation and LES_Cice are larger for the sea-ice surface temperature than for the air temperature at 5 m. Except for wind speed, higher values are still underestimated for all near surface variables. The mean deviations are smaller for LES_Cice than for LES_Ctrl, which is in better agreement with the observations.

Table 7.5 shows the statistical values from observation and NWP_Cice during the period of 6-10 February 2020. Compared to LES_Ctrl (see Table 7.3) and LES_Cice (see Table 7.4), the mean values of the differences between observation and model are closer to zero for each variable, and none of the values is statistically significant.

Figure 7.19 shows the probability density distribution from NWP_Cice and the observations, as well as the probability density distribution of the differences between observation and NWP_Cice. Similar to the probability density distributions for the temperature depending variables close to the surface from LES_Cice (Figure 7.18), NWP_Cice shows a larger range of values than LES_Ctrl (Figure 7.17). The wind speed distribution is similar to LES_Cice and to LES_Ctrl.

The simulated probability density distribution for the temperature at sea-ice surface ranges from 237 K to 251 K. Compared to the observation, NWP_Cice underestimates the higher sea-ice surface temperatures by around 3 K. The lower temperature limit is

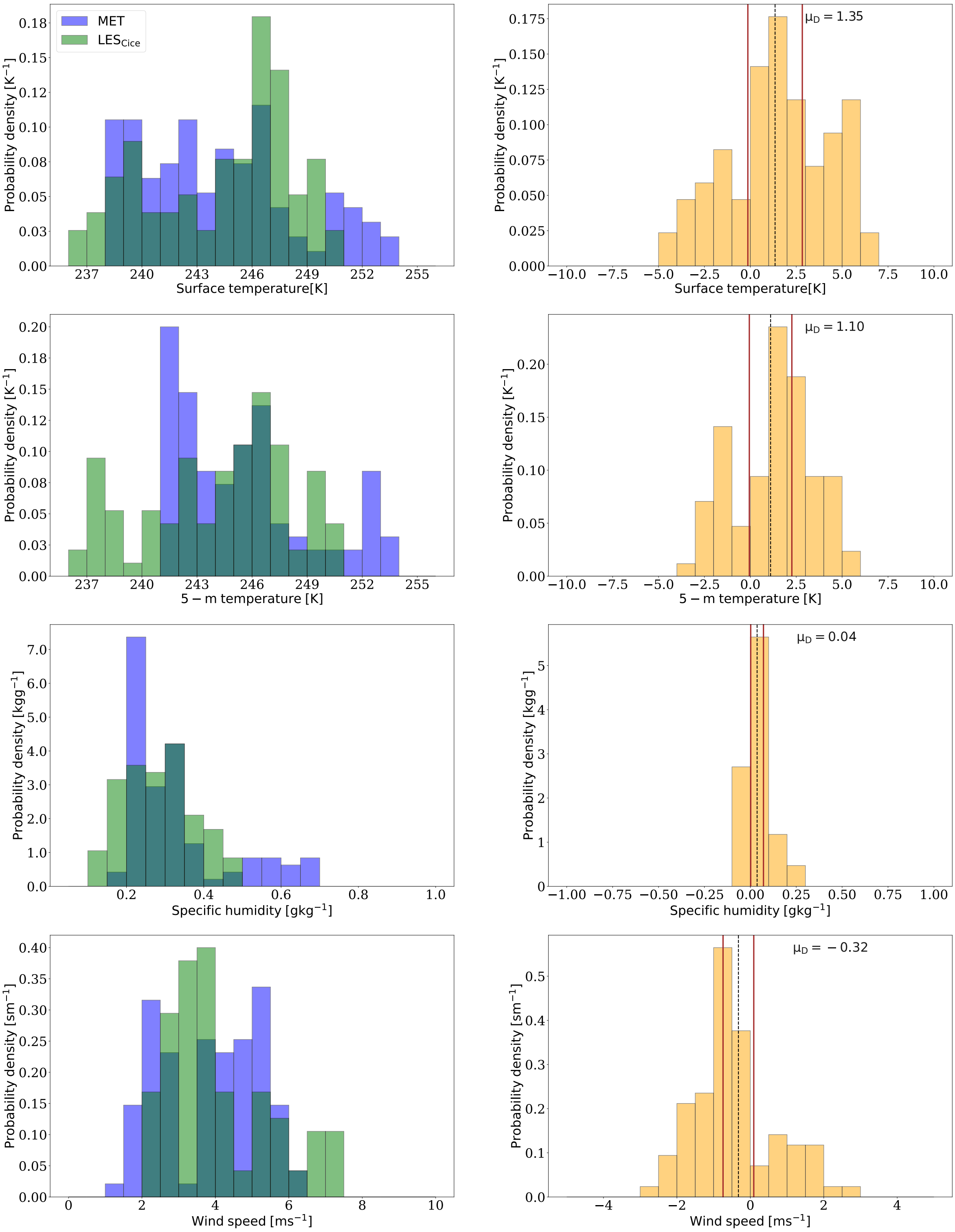

Figure 7.18: Probability density distribution (left) of sea-ice surface temperature, air temperature at 5 m, specific humidity at 5 m, and wind speed at 5 m (from top to bottom) from LES_Cice (green) and MOSAiC data (blue), and corresponding probability density distribution of the differences between the simulations and the observations (right), based on hourly data of the period 6-10 February 2020 at the mean Polarstern position. The dashed lines show the mean of the differences for each variable. The red lines show the 95% confidence interval.

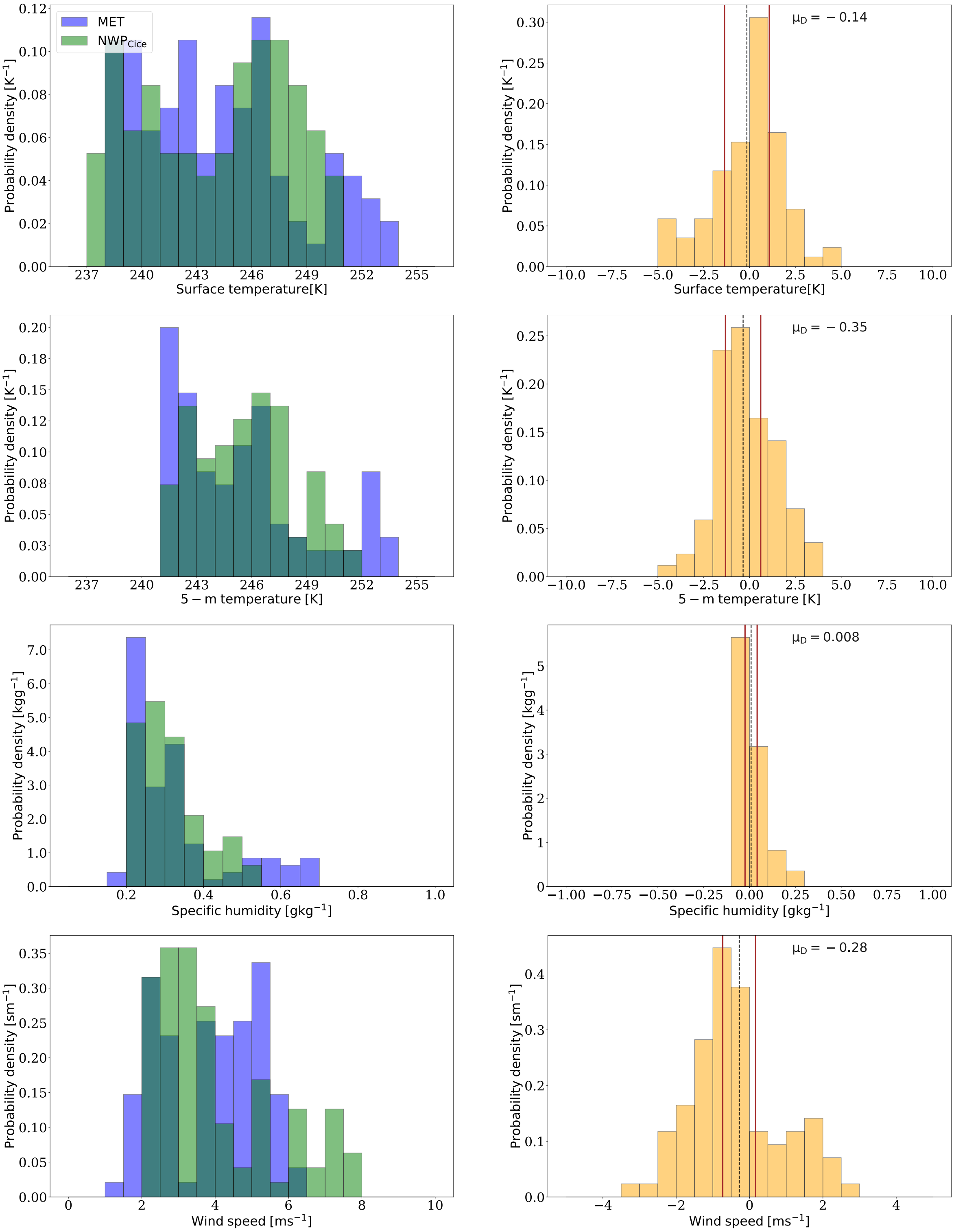

Figure 7.19: Probability density distribution (left) of sea-ice surface temperature, air temperature at 5 m, specific humidity at 5 m, and wind speed at 5 m (from top to bottom) from NWP_Cice (green) and MOSAiC data (blue), and corresponding frequency distribution of the differences between the simulations and observations (right), based on hourly data of the period 6-10 February 2020 at the mean Polarstern position. The dashed lines show the mean of the differences for each variable. The red lines show the 95% confidence interval.

consistent with the observation. However, the occurrence of low temperature at sea-ice surface is overestimated by NWP_Cice compared to the observation. Further, the model overestimates the values in the central section between 245 K and 251 K compared to the observation. Nevertheless, the sea-ice surface temperature distribution from NWP_Cice agrees better with the one from the observation than any of the previous simulations.
The probability density distribution for the air temperature at 5 m from NWP_Cice ranges from 241 K to 252 K. Similar to the modeled sea-ice surface temperature, NWP_Cice underestimates the higher values by around 2 K compared to the observation. The lower limit of the air temperature from observation and from NWP_Cice agree. However, the model underestimates the lower temperatures and shows an overestimation of values in the central section from 244 K to 251 K. Nevertheless, the air temperature at 5 m in NWP_Cice is in better agreement with the observation than the previous simulations.
The probability density distribution for the simulated specific humidity at 5 m from NWP_Cice shows values between 0.2 g kg^{-1} to 0.55 g kg^{-1}. NWP_Cice underestimates the higher values and slightly and overestimates the lower values compared to the observation.
The simulated probability density distribution for wind speed at 5 m from NWP_Cice ranges from 2 m s^{-1} to 8 m s^{-1}. Compared to the observation, NWP_Cice mostly overestimates the observed wind speed. On the other hand, the overall distribution of wind speed from NWP_Cice is similar to LES_Cice and LES_Ctrl. The simulated wind speed shows mainly values between 2 and 4 m s^{-1} and does not show values lower than 2 m s^{-1}.
Just as for LES_Cice, the adapted sea-ice surface parametrization affects the near-surface temperature and specific humidity from NWP_Cice. The values are broader distributed, even though higher values are still underestimated. Except for the wind speed, the modeled temperature and specific humidity in NWP_Cice are in better agreement with the near-surface observations than the other simulations.

The comparison of the simulation results from LES_Ctrl, LES_Cice and NWP_Cice for a very calm weather situation with stably stratified atmosphere in February 2020 demonstrates the impact of changed parameterizations on the near-surface variables. While the model with the default settings in the sea-ice surface parameterization (LES_Ctrl) shows almost no variations during the simulation periods, the sea-ice surface temperature, the air temperature at 5 m and the specific humidity at 5 m in LES_Cice and NWP_Cice the observations. The only variable that is less affected by the changes in the sea-ice surface parameterization is wind speed at 5 m. The comparison in LES_Cice and NWP_Cice shows that the choice of the turbulence parameterization is particularly important during very cold weather situations. However, the temporal evolution (Figure 7.16) of near-surface temperatures and specific humidity from NWP_Cice agrees better with the observation.

7.4.2 Vertical profiles

Figure 7.20 shows the vertical profiles of the lowermost 50 m for temperature from LES_Ctrl, LES_Cice, NWP_Cice, and the observations. The focus here is on the temperature profiles here, as the differences in the model performance are greatest for this variable. The vertical profiles are chosen around the very cold stably stratified atmospheric weather situation on 7-9 February. All three models show the same pattern of a temperature inversion as observed for the lowest layers. The modeled variables near to the surface show the largest differences with the observations. These differences decrease with increas-

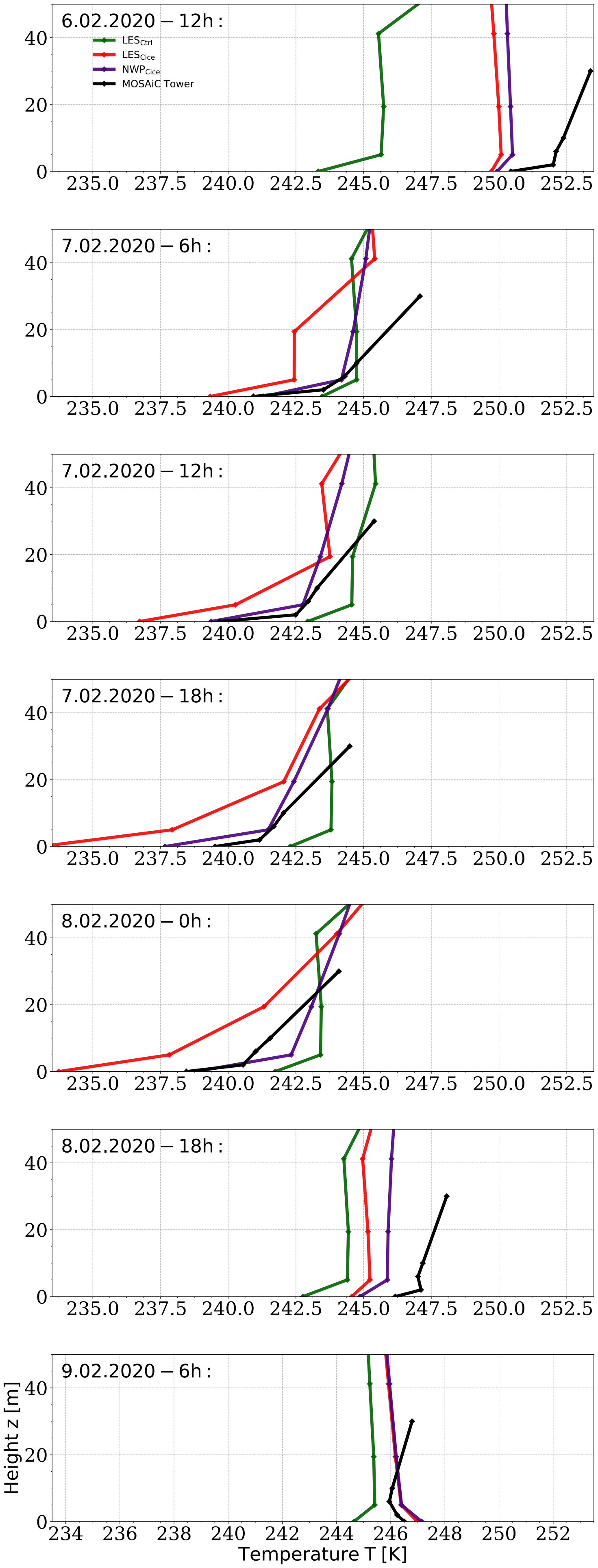

Figure 7.20: Vertical temperature profiles from LES_Ctrl (green), LES_Cice (red), NWP_Cice (violet), and MOSAiC data (black) for specific times within the period 6-10 February 2020.

ing height. The temperature profiles from the observations show a very stably stratified boundary atmosphere. Before the sky clears off on 6 February, the difference between the temperature at the sea-ice surface and the upper layer does not exceed 2 K. On 7 February, the sea-ice surface temperature drops by 10 K and remains around 240 K for the following hours. The observed profile shows a strong temperature gradient between the surface and the lowest 30 m. On 9 February the atmosphere changes near to the surface and the temperature profile shows a very weak unstable state with a small negative temperature gradient of less than -1 K between the surface and the lowest 10 m.

During the simulation period the vertical profiles of LES_Ctrl, LES_Cice and NWP_Cice have different values near to the surface, but the differences between the model runs decrease with height. Before the very stable stratification between 7 and 9 February, LES_Ctrl strongly underestimates the observation on 6 February. During the very cold days LES_Ctrl seems to be close to the observation. However, the temperature profiles from LES_Ctrl do not change at the same rate as the observed temperature profiles. At the beginning of the simulation period on 6 February, the modeled sea-ice surface temperature is located at around 244 K and the observation is around 250 K. During the very stable stratification observed on 7-8 February, the modeled sea-ice surface temperature slowly decreases towards 242 K, while the observed one is colder around 240 K. LES_Ctrl then does not response quickly enough to the observed temperature rise on 8 February, when the sea-ice surface temperature is warmer than the overlying atmospheric layers.

The temperature profiles of LES_Cice and NWP_Cice are about 2 to 2.5 K colder than the observation on 6 February. The temperature profiles from LES_Cice show smaller values than the observation for most of the simulation period. On 7-8 February, the modeled sea-ice surface temperature drops down towards 234 K, which is about 6 K lower than the observation. On 9 February, the temperature profile of LES_Cice is close to the observed profile. The variables from LES_Ctrl and from LES_Cice differ most near the surface. The near-surface temperature of LES_Cice is mostly lower than the observed, but changes faster with time and weather situation.

The near-surface temperature profile of NWP_Cice is closer to the observations than for the previous simulations. Throughout the simulation period, model and observed near-surface temperatures differ by less than 2 K. With increasing height, the vertical profiles of NWP_Cice approach those of the other models. Compared to LES_Ctrl and LES_Cice, the temperature profiles of NWP_Cice are in better agreement with the observations for the lowest atmospheric layers.

7.4.3 Surface fluxes

Since the short-wave radiation can be neglected during polar night, the surface energy balance is primarily controlled by downwelling long-wave radiation. To evaluate downwelling and upwelling heat fluxes at the surface for LES_Ctrl, LES_Cice, and NWP_Cice, the temporal evolution of the simulated downwelling long-wave radiation, upwelling long-wave radiation, the latent heat flux, the sensible heat flux, the drag coefficient and the bulk Richardson number at the surface are contrasted and compared to observations in Figure 7.21. At the beginning and towards the end of the period, the downwelling long-wave radiation increases more than 200 Wm^{-2} for the observation and the simulations, which indicate the presence of some low-level clouds. Between 7-8 February, the downwelling long-wave radiation decreases around 150 Wm^{-2}, which describes a cloud-free very stably stratified atmosphere. All model simulations underestimated the downwelling long-wave radiation between 7-8 February. During these days, the values were 10-20 $\mathrm{Wm^{-2}}$ lower than the observations. Consequently, the bias in the downwelling long-wave radiation causes an underestimation for the upwelling long-wave radiation and the sea-ice surface temperature from LES_Cice (see Figure 7.16) during the same time. Since all models are affected, it can be speculated that this discrepancy is caused by the lateral boundary conditions, as they come from ICON-LAM with a horizontal grid-scale of 3 km (NWP_Cice-3km). Mesoscale atmospheric models often face the challenge of modeling small-scale processes within their grid cells (e.g. Vihma et al. (2014)). There can be several reasons why incoming long-wave radiation is misinterpreted, a common one being the insufficient representation of clouds. They are highly sensitive to turbulence, vertical mixing, and surface fluxes. In addition, the cloud microphysics may not accurately represent the radiative properties of the clouds. Other boundary layer properties, such as aerosol and

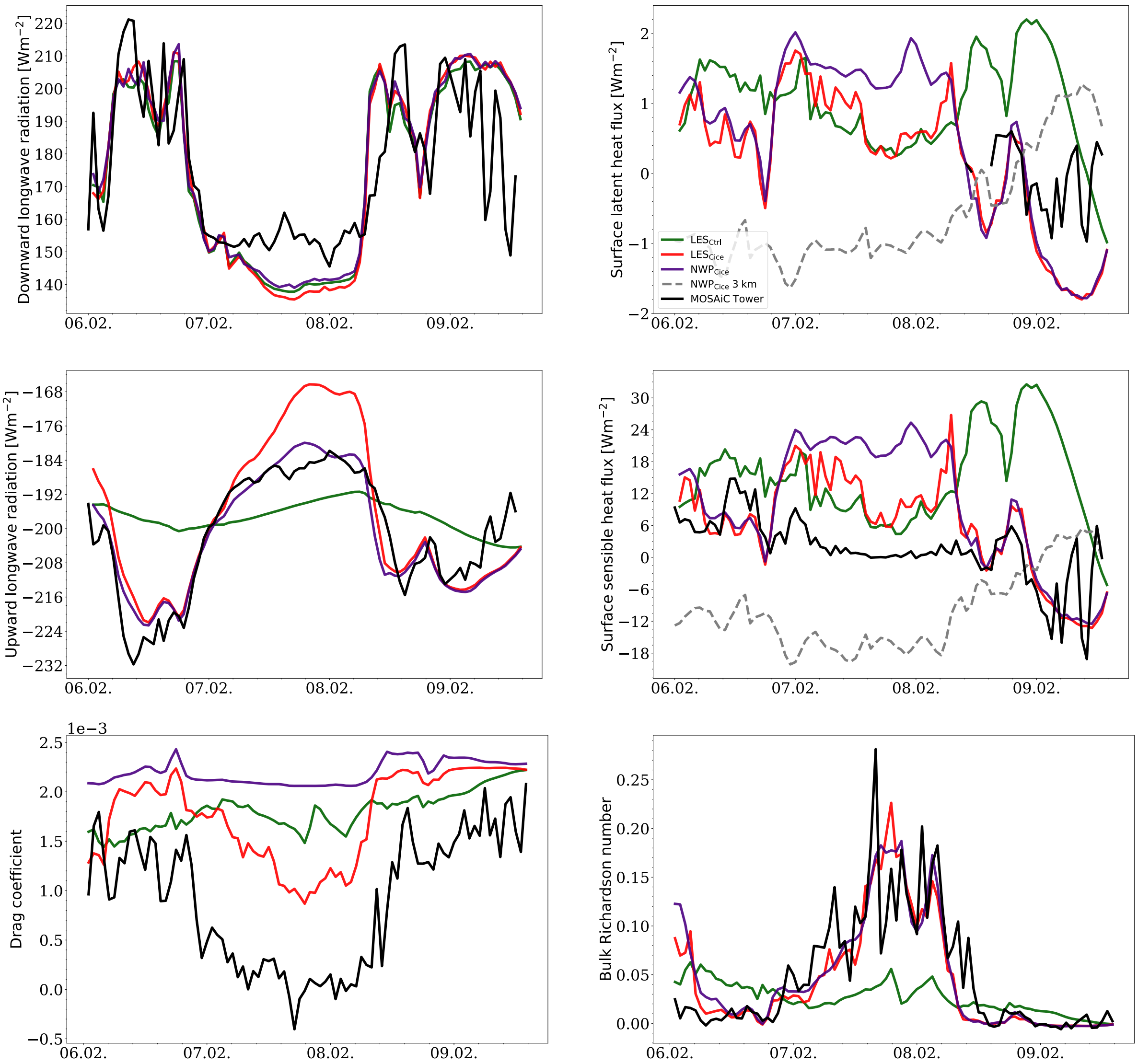

Figure 7.21: Temporal evolution of surface downwelling long-wave radiation (upper left), surface latent heat flux (upper right), upwelling long-wave radiation at surface (middle left), surface sensible heat flux (middle right), surface drag coefficient (lower left), and surface bulk Richardson number (lower right) from LES_Ctrl (green), LES_Cice (red), NWP_Cice (violet), and MOSAiC data (black) in the period 6-10 February 2020. Positive values suggest downwelling, negative values suggest upwelling fluxes.

trace gas concentrations, may be misrepresented, leading to inaccurate absorption and emission processes. However, this also means that NWP_Cice only shows supposedly better simulation results for the upwelling long-wave radiation and the sea-ice surface temperature. Unfortunately, hardly any data are available for the near-surface latent heat fluxes. Due to too low temperatures and the resulting low humidity, the latent heat flux has a smaller influence on the surface energy budget during the polar night than the sensible heat flux and is therefore negligible. For the sensible heat flux, observational data from 3.5 m are used for comparison. All simulation results overestimate the exchange of sensible heat fluxes between 7 and 8 February. However, the models show different performance with respect to their resolution and turbulence scheme. The simulation results with high horizontal grid-resolution are in better agreement with the observation than the coarser NWP_Cice-3km, which differs the most from the observation. Furthermore, LES_Ctrl overestimates the sensible heat flux for the whole simulation period compared to the observation. The model runs of LES_Cice and NWP_Cice are closer to the observations, but do overestimate the downwelling heat flux at the sea-ice surface during the very cold period of 7-8 February. The bias of more than 18 $\mathrm{W\,m^{-2}}$ in NWP_Cice is higher than in LES_Cice, which ranges between 6 and 12 $\mathrm{W\,m^{-2}}$. The overestimation of the sensible heat flux by NWP_Cice and the negative bias in the downwelling long-wave radiation lead to the supposedly coinciding sea-ice surface temperature (see Figure 7.16) between 7 and 8 February. For the same days, LES_Cice shows a smaller overestimation of the sensible heat flux. The dimensionless surface drag coefficient depends on the stability between the atmosphere and the surface, while the bulk Richardson number at the surface is a measure of the stability between the surface and the atmosphere (Figure 7.16). The drag coefficient is significantly overestimated by NWP_Cice, with a positive bias of about $2{\times}10^{-3}$. The time evolution of the drag coefficient in LES_Cice is similarly distributed to the observation, but slightly positively biased with $1{\times}10^{-3}$. The negative values in the observation refer to errors during the observations. The drag coefficient changes in the simulation results of LES_Ctrl and LES_Cice in proportion to the bulk Richardson number. On the other hand, the simulation results from LES_Cice and from NWP_Cice show similar values for the bulk Richardson number at the surface and are closer to the values of the observation than the control simulation.

The relationship between the sea-ice surface temperature and the downwelling long-wave radiation is shown in Figure 7.22. LES_Ctrl shows almost no correlation between temperature and radiation, while in the other simulations the temperature increases linearly with the radiation, which is in good agreement with the observations. For all simulations, the distribution between temperature and radiation is shifted to the left side, showing that the long-wave radiation is always underestimated compared to the observations. The downwelling long-wave radiation mainly reflects the specific synoptic-scale conditions controlled by the model's lateral boundary condition. Thus, the negative bias in the radiation has to be taken into account when evaluating the surface variables for the stably stratified atmosphere on 7-8 February. The deviation of the sensible heat flux from LES_Cice cannot compensate for the bias of the downwelling long-wave radiation. In other words, with a smaller bias in the downwelling long-wave radiation, the near-surface temperatures in LES_Cice would most likely be in better agreement with the observations than any of the other models. On the other hand, this also means that a warm surface temperature overestimation can be expected in NWP_Cice with realistic downwelling long-wave radiation.

Figure 7.23 shows the sensible heat flux scaled by the wind speed at 5 m against the

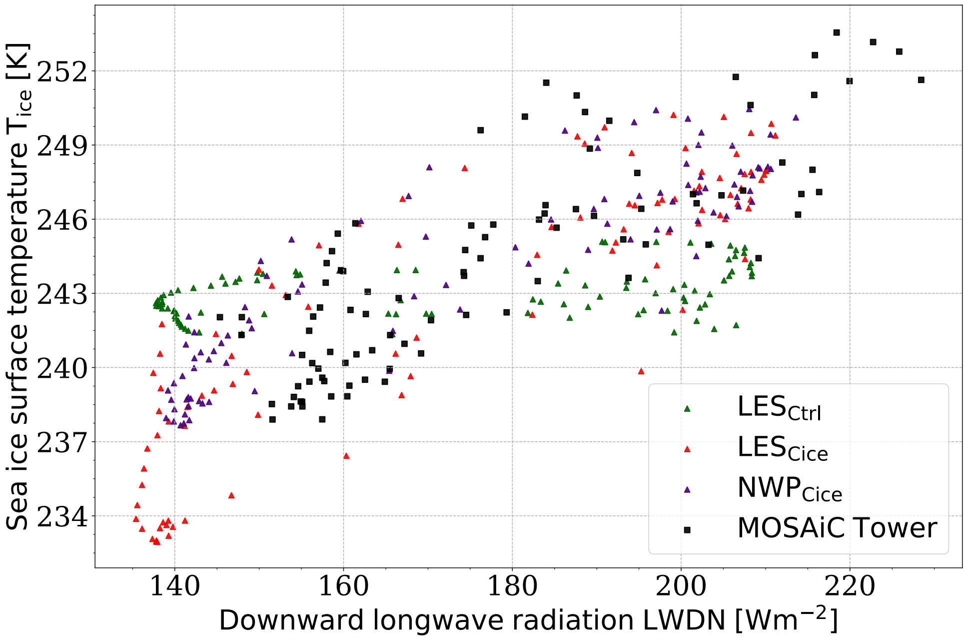

Figure 7.22: Sea-ice surface temperature as a function of surface downwelling long-wave radiation from LES_Ctrl (green triangles), LES_Cice (orange triangles), NWP_Cice (violet triangles), and MOSAiC data (black rectangles) in the period 6-10 February 2020.

vertical temperature gradient $\Delta T = T(z*) - T_s$, where $z*$=5 m and the index s refers to the sea-ice surface. Observations during MOSAiC are shown together with model results from LES_Ctrl, LES_Cice, and NWP_Cice. The observations show two distinct regimes. The first is characterized by slightly unstable and slightly stable stratification in the surface layer. In the unstable regime, the scaled upward heat flux decreases linearly with decreasing ΔT to zero for neutral conditions (ΔT=0). In the stable regime there is the same linear dependence exists with the same slope as in the unstable regime up to a threshold of $\Delta T \approx 1$ K, so that the amount of downward heat fluxes increases with increasing ΔT. For further increases in stability, the scaled heat flux approaches a plateau, but with large scatter (values between 0 and -4 kgm^{-1} s^{-2}).
All model runs are able to reproduce the same linear relationship as observed for the first regime for very small temperature gradients. NWP_Cice continues the linear relationship without any change in slope up to large ΔT of at least 4 K. Both runs, LES_Ctrl and LES_Cice, are able to reproduce the second regime with a kind of plateau at strong stability. However, this second regime starts later than in the observations, namely at ΔT =2 K. Two other results are noteworthy. The first is that, similar to the observations, the scatter of the model results is larger in regime 2 than in regime 1. The second finding is that for LES_Cice also sometimes produces large temperature gradients. The largest of these is about 5.7 K, while the largest in the observations is 3.5 K. This could indicate a systematic drawback in the model's ability to reproduce the stable regime. Furthermore, Figure 7.23 shows that especially in regime 2 the model runs all overestimate the heat flux.
In the first regime the temperature gradient dominates the heat flux, whereas in the second regime the exchange coefficient dominates the near-surface heat flux. The relationship between the scaled heat flux and the temperature gradient is determined by the parameterization of the near-surface transfer coefficients for momentum $f_m(R_i)$ and heat

$f_h(R_i)$, and in particular by their dependence on the stability, expressed by the transfer coefficients normalized to their neutral values. These stability dependent functions are usually determined on the basis of the Monin-Obukhov similarity theory. In this work, they are given by eq. 4.6.30 and eq. 4.6.31 for LES_Ctrl and LES_Cice.

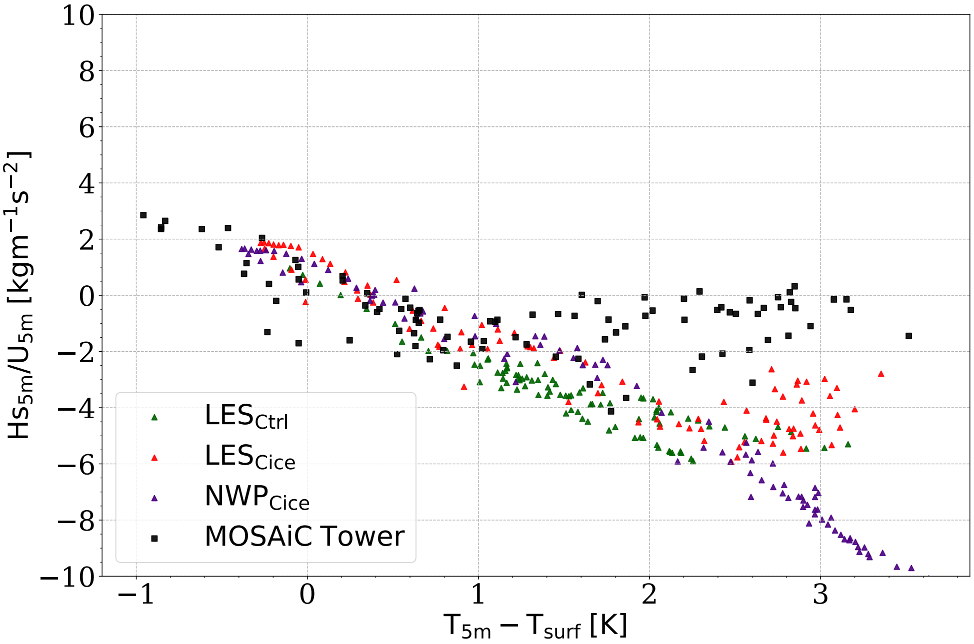

Figure 7.23: Sensible heat flux (positive upward) normalized with horizontal wind speed at 5 m as a function of the temperature difference between 5 m and the surface from LES_Ctrl (green triangles), LES_Cice (orange triangles), NWP_Cice (violet triangles), and MOSAiC data (black rectangles) in the period 6-10 February 2020.

7.4.4 Boundary Layer Height

The Planetary Boundary Layer (PBL) is shaped by the properties of the Earth's surface (Stull, 1988). Its height is a measure of the quality of the representation of surface processes at the local scale (Heinze et al., 2017). Several definitions of the height of the planetary boundary layer (PBLH) are considered equivalent because they correspond to the point where tangential turbulent stresses disappear, align with the low-level jet, and coincide with the level at which both the gradient and the flux Richardson numbers reach supercritical values (Kosović and Curry, 2000). To keep the comparison of results as consistent as possible, the same method was used to calculate the PBLH as was used to calculate the PBLH for the radiosondes. Here the definition used to determine the PBLH is the level at which the bulk Richardson number exceeds 0.28 (Richardson et al., 2013). The bulk Richardson number can be calculated using the equation

$$Ri_b = \frac{g}{\theta_{v0}} \frac{(\theta_v - \theta_{v0})z}{u^2 + v^2}, \tag{7.4.1}$$

where θ_{v0} and θ_v are the virtual potential temperatures at the surface and at height z, respectively. Figure 7.24 shows the time series for the PBLH between 6 and 10 February from the simulations (calculated using eq. 7.4.1) and derived from the observations. For 6-7 February, LES_Cice and NWP_Cice show a higher PBLH than LES_Ctrl and are closer to the observation. The drastic change in PBLH after the stable stratification period on 6-8 February is associated with a transition to a more cloudy state, which is also visible in the surface energy budget as discussed in section 7.4.3. During the days with a stable stratified atmosphere on 6-8 February, the simulation results are in overall good agreement with the observations. However, the PBLH of LES_Ctrl decreases later than in the other simulations due to the slow surface response. From 8 to 10 February, the PBLH increases in both the observations and the simulations. Between 9 and 10 February, the simulated PBLHs reach rather high values compared to the observed PBLH. The simulated PBLH is rather independent of the applied turbulence parameterization, but is positively influenced by the adjustment in the sea ice scheme.

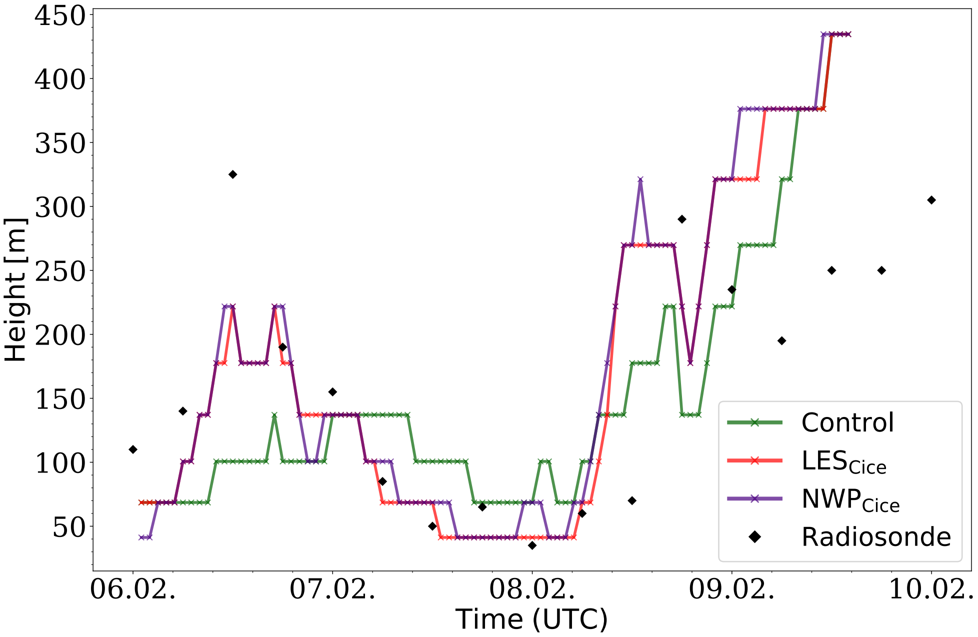

Figure 7.24: Temporal evolution of the boundary layer height from LES_Ctrl (green), LES_Cice (red), NWP_Cice (violet), and 6-hourly radiosonde data (diamonds) in the period 6-10 February 2020.

7.5 Impact of the parametrization schemes under stormy conditions

In order to evaluate the changes in ICON-LEM for various weather conditions during Arctic winter, a stormy period in November 2019 is chosen for the second investigation. The influence of strong turbulence on near-surface variables is studied with the same model setup mentioned above and compared to the observations.

7.5.1 Near-surface variables

Figure 7.25 shows the observed and the modeled temporal evolution of the temperature for the lowermost 500 m during a week full of storms in 15-22 November 2019. Both storms, between 16-17 November and 19-20 November, are captured at reasonable timing by the model. The range of values for the temperature are in good agreement between observation and simulation. However, the warm air-mass on 18 November is not well reproduced by the model. Instead, in the vertical the air temperature is interrupted by a colder layer, with warmer air masses near the surface and above around 400 m. This indicates to a known problem in atmospheric modeling related to low-level cloud processes and is addressed later in this chapter. In general, the cold phases after the storms are much more pronounced in the simulation than in the observation. The cold stratification after the second storm in 21 November is captured by the model, but is colder than observed. However, the following cold phase in the simulation around 22 November was not observed. Overall, the model seems to be colder than the observation.

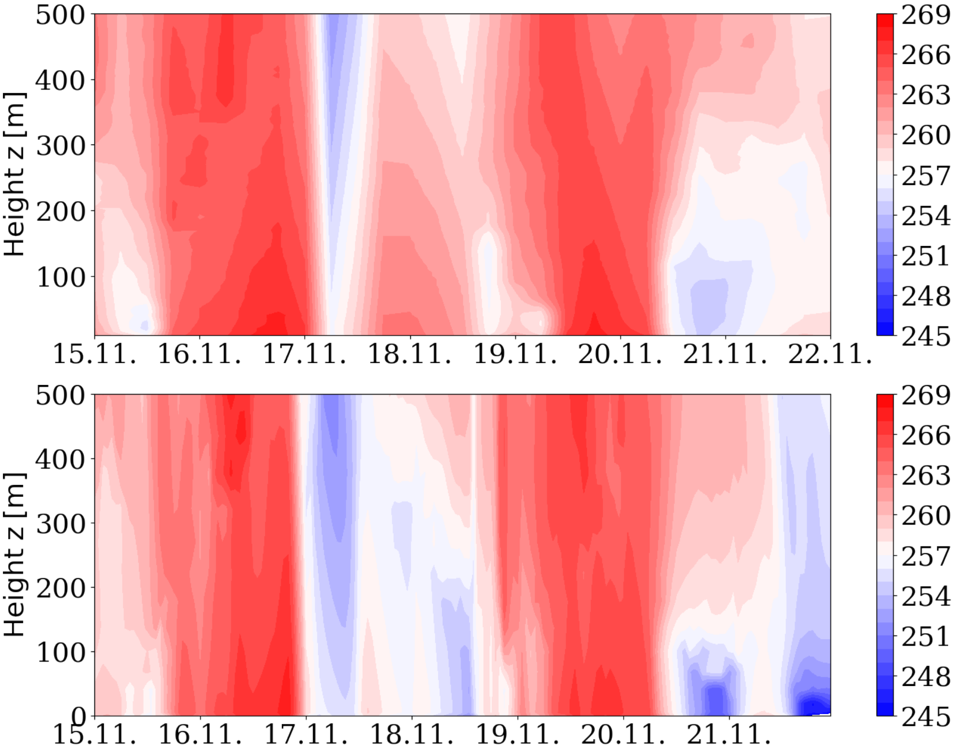

Figure 7.25: Height-time cross section of the temperature in the lowermost 500 m from 6-hourly radiosonde data (above) and from LES_Ctrl (below) for the period 15-22 November 2019.

Figure 7.26 shows the temporal evolution of temperature at surface and air, specific humidity and wind speed from LES_Ctrl, LES_Cice, NWP_Cice, and the observations in 15-22 November 2019. As a result of the severe storms, some of the instruments were damaged and had to be repaired. Therefore, some of the data is missing for comparison, especially after the first storm on 17 November 2019. This concerned in particular the 10 m tower, which was the only one to measure meteorological quantities, such as temperature, specific humidity, and wind speed at four different heights. Among other things, it measured the values between 5 and 6 m, which corresponds to the lowest level of the atmospheric model. In addition, the data consisting of the instabilities are not considered for the evaluation and are marked grey in Figure 7.26 and all the following evaluations. Nevertheless, there is enough data to give a good idea of the evolution of the near-surface variables. The exception was sea ice surface temperature measurements, which were unaffected by the storms. All experiments are able to catch the changing weather situations reasonably. The temperature at surface and air temperature at 5 m, as well as the specific humidity at 5 m are a bit lower and delayed in LES_Ctrl compared to the simulation results in LES_Cice and NWP_Cice. The latter ones are similarly distributed and closer to the observation for the whole simulation period. LES_Cice and

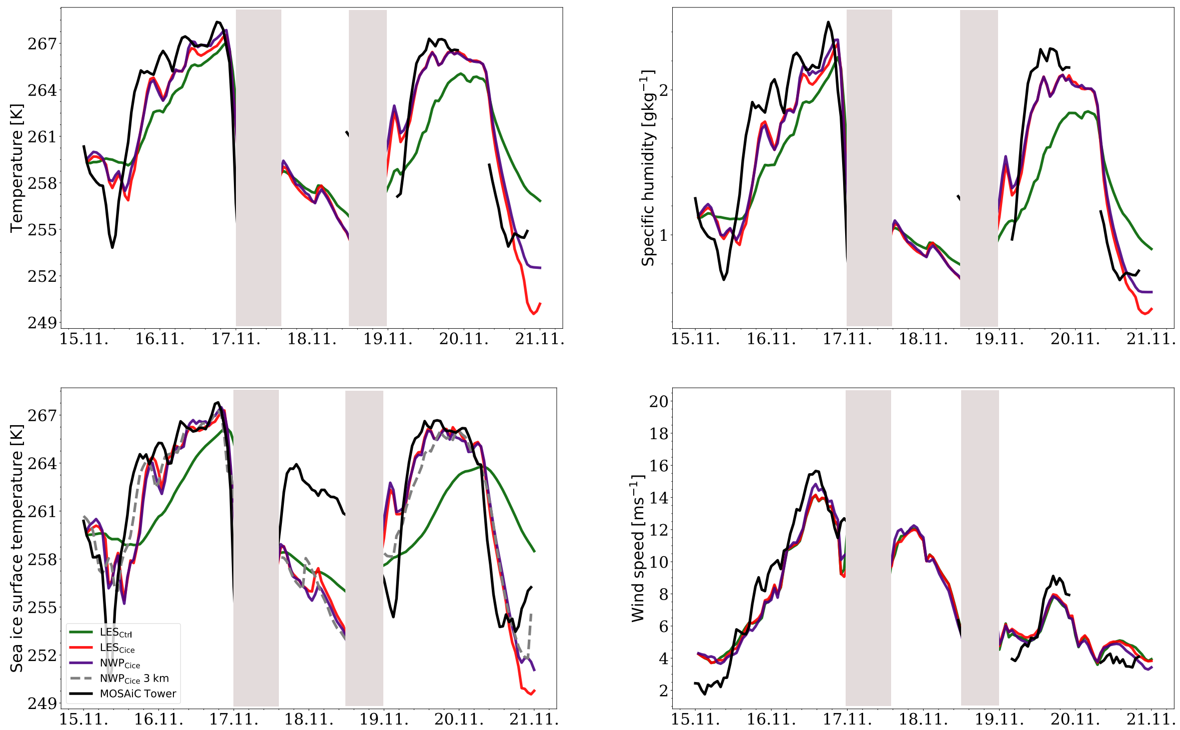

Figure 7.26: Temporal evolution of air temperature at 5 m (upper left), sea-ice surface temperature (lower left), specific humidity at 5 m (upper right), and wind speed at 5 m (lower right) from LES_Ctrl (green), LES_Cice (red), NWP_Cice (violet), NWP_Cice-3km (dashed grey), and MOSAiC data (black) in the period 15-22 November 2019.

Variable	n_1	n_2	n_D
Surface temperature [K]	143	116	116
5 m temperature [K]	94	116	81
specific humidity [g kg^{-1}]	93	116	80
wind speed [m s^{-1}]	93	116	80

Table 7.6: The sample sizes of the observation n_1, the simulations n_2, and their corresponding difference sample n_D.

NWP_Cice show stronger fluctuations than LES_Ctrl and are in better agreement with the observation as their derivations are comparatively small. The additional simulation result of the sea-ice surface temperature in NWP_Cice-3km is also shown in the Figure. Similar to LES_Cice and NWP_Cice, the values are close to the observation. However, the observed warmer air-mass for the sea-ice surface temperature is not recognized by any model in 17-19 November. The simulation results for wind speed at 5 m in LES_Ctrl, LES_Cice and NWP_Cice are similar to each other, with values slightly lower than those observed.

Table 7.6 shows the sample sizes for the observation n_1, the simulation n_2, and the sample size of their difference n_D in 15-21 November 2019. n_1 is affected by the absence of data due to the collapse of equipment during the storms. n_2 refers to the same sample size as in Section 7.1 (see e.g. Table 7.2), with missing data between 17 November 2019, 0 h and 14 h, as well as in 18 November 2019, 12 h, and 19 November 2019, 0 h. For this reason, the sample size of the difference between observation and simulation is reduced.

Variable	μ_{obs}	s_{obs}	μ_{ctrl}	s_{ctrl}	ν	t'	p	μ_D
Surface temperature [K]	261.15	4.41	260.57	2.7	240.22	1.29	0.19	0.58
5 m temperature [K]	261.83	4.94	261.12	3.16	151.43	1.19	0.23	0.7
specific humidity [$\mathrm{g\,kg^{-1}}$]	1.53	0.6	1.37	0.39	151.02	2.21	0.03	**0.16**
wind speed [$\mathrm{m\,s^{-1}}$]	7.34	4.05	7.43	3.11	169.28	-0.18	0.85	-0.09

Table 7.7: Statistical values of different meteorological variables on 15-21 November 2019. Listed are the mean value μ_{obs} and the standard deviation s_{obs} from the observation, the mean value μ_{ctrl} and the standard deviation s_{ctrl} from LES_Ctrl, as well as their mean value of the differences μ_D. Bold values indicate that the difference between model and observation. The results of the statistical t-test include the number of degrees of freedom ν, the t-value t', and the p (probability that the null hypothesis is correct).

Table 7.7 shows the statistical values calculated by the formulations of the Welch t-test (Equations 7.1.1-7.1.5) for the variables from the observation and from LES_Ctrl in 15-21 November 2019. Due to the lower sample sizes, the number of degrees of freedom is lower for the 5 m temperature, specific humidity and wind speed compared to the surface sea-ice temperature. For specific humidity, the null hypothesis can be rejected as the statistical test shows a significant result with a p-value lower than the significance level $\alpha = 0.05$. For this reason, the mean difference between observation and model is highlighted for specific humidity. The other variables have higher p-values, so the null hypothesis remains valid. However, the results show that the difference between observation and LES_Ctrl is smallest for wind speed.

The probability density distribution for the meteorological variables from observation and LES_Ctrl and their corresponding probability density distribution of the differences between observations and LES_Ctrl are shown in Figure 7.27. Positive values refer to higher values in the observation and negative values refer to higher values in the simulation. The simulation results in LES_Ctrl for the stormy case in November 2019 show stronger fluctuations compared to the simulations of the clear-sky period with stably stratification in February 2020 (see Section 7.4). However, all modeled variables range smaller than the observation. This results in a higher concentration of the values of all variables in the central section of the range of values for LES_Ctrl.
The probability density distribution for the simulated sea-ice surface temperature shows values in the range from 255 K to 267 K, whereas the observed sea-ice surface temperature range from 250 K to 268 K. The observed lowest sea-ice surface temperatures are related to the rapid temperature drop before and after the first storm (see also Figure 7.26). The simulated sea-ice surface temperature shows higher values between 255 K and 257 K than the observed sea-ice surface temperature, which mostly ranges at higher temperatures between 264 K and 268 K. The majority of the probability density distribution of the differences between observations and LES_Ctrl for the sea-ice surface shows mean deviations up to about 10 K, where the simulation over-predicts the observation. This is due to the not captured temperature drop in the simulation. However, LES_Ctrl underestimates the observation for most of the simulation period.
The probability distribution for the air temperature at 5 m in the observation ranges from 253 K to 269 K. The simulated air temperature at 5 m ranges from 255 K to 268 K. Similar to the sea-ice surface temperature, the simulation result of the air temperature are higher at colder values between 255 K and 257 K than the observation with higher temperatures between 266 K and 267 K, as well as between 253 K and 254 K. The probability density

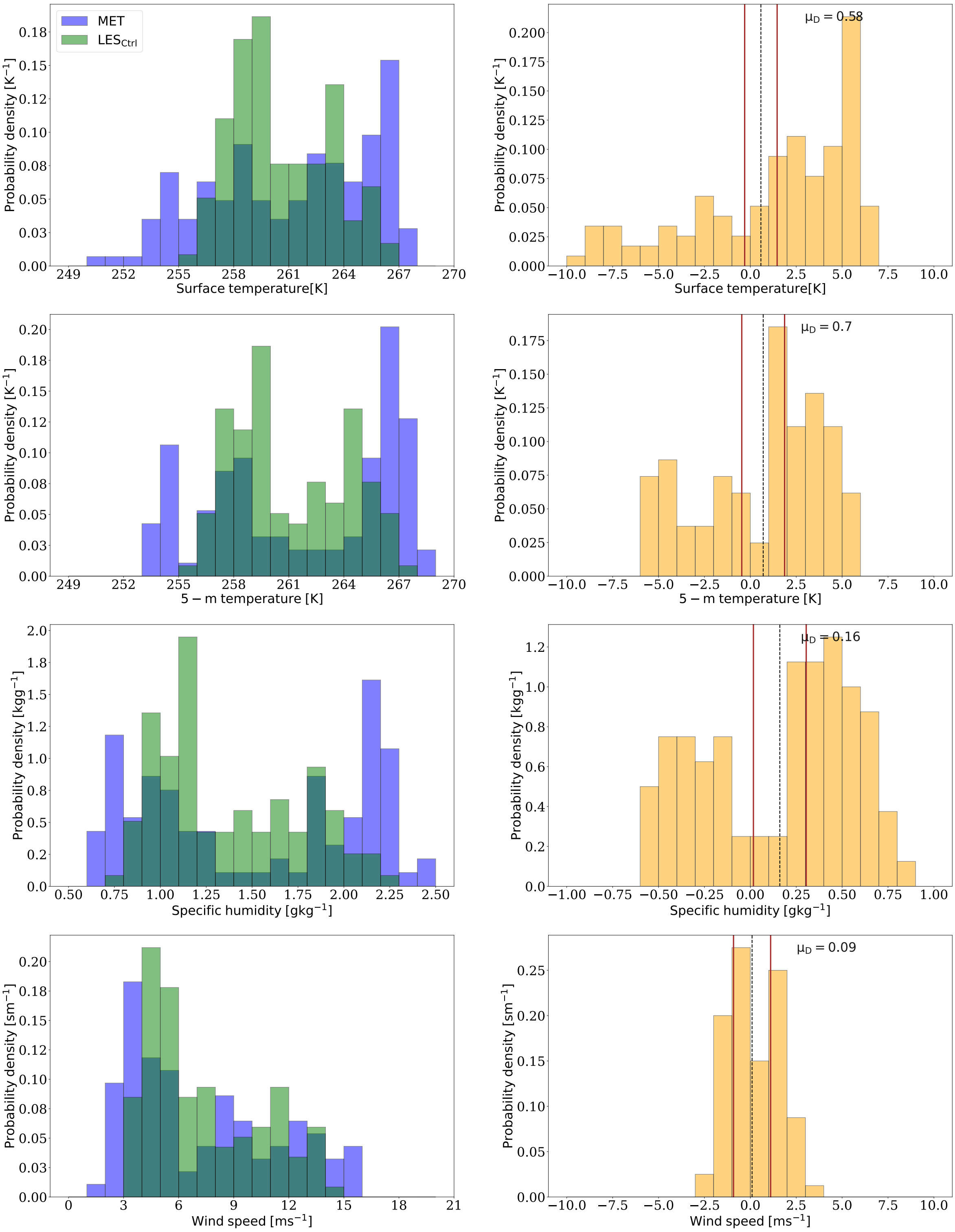

Figure 7.27: Probability density distribution (left) of sea-ice surface temperature, air temperature at 5 m, specific humidity at 5 m, and wind speed at 5 m (from top to bottom) from LES_Ctrl (green) and MOSAiC data (blue), and corresponding probability density distribution of the differences between the simulations and the observations (right), based on hourly data of the period 15-22 November 2019 at the mean Polarstern position. The dashed lines show the mean of the differences for each variable. The red lines show the 95% confidence interval.

Variable	μ_{obs}	s_{obs}	μ_{Lcice}	s_{Lcice}	ν	t'	p	μ_D
Surface temperature [K]	263.15	4.5	260.74	4.87	223.31	0.69	0.48	0.41
5 m temperature [K]	261.83	4.94	261.14	4.82	197.02	1.01	0.31	0.69
specific humidity [$\mathrm{g\,kg^{-1}}$]	1.53	0.6	1.42	0.54	187.15	1.37	0.17	0.11
wind speed [$\mathrm{m\,s^{-1}}$]	7.34	4.05	7.48	3.10	168.92	-0.27	0.78	-0.14

Table 7.8: Statistical values of different meteorological variables on 15-21 November 2019. Listed are the mean value μ_{obs} and the standard deviation s_{obs} from the observation, the mean value μ_{Lcice} and the standard deviation s_{Lcice} from LES_Ctrl, as well as their mean value of the differences μ_D. Bold values indicate the difference between model and observation. The results of the statistical t-test include the number of degrees of freedom ν, the t-value t', and the p (probability that the null hypothesis is correct).

distribution of the differences between observation and LES_Ctrl for air temperature at 5 m shows mean differences up to around 6 K. As already mentioned above for the sea-ice surface temperature, the overestimated simulated air temperature is caused by the temperature drop at the beginning of the simulation period.
The probability density distribution for specific humidity at 5 m from the observation ranges from 0.6 $\mathrm{g\,kg^{-1}}$ to 2.5 $\mathrm{g\,kg^{-1}}$. The from specific humidity LES_Ctrl ranges between 0.75 $\mathrm{g\,kg^{-1}}$ and 2.25 $\mathrm{g\,kg^{-1}}$ and are similarly distributed as the observation. LES_Ctrl overestimates the observed low specific humidity, but also underestimates the high observed specific humidity. Therefore, observation and simulation show mean deviations up to 0.6 $\mathrm{g\,kg^{-1}}$.
The probability density distribution of the observed wind speed at 5 m ranges between 1 $\mathrm{m\,s^{-1}}$ and 16 $\mathrm{m\,s^{-1}}$, while the simulated one ranges between 3 $\mathrm{m\,s^{-1}}$ and 15 $\mathrm{m\,s^{-1}}$. Simulated wind speeds are similarly to the observation, with a large distribution for low wind speed and a small distribution for high wind speed. The probability density distribution of the differences between observation and LES_Ctrl shows mainly mean deviations up to 4 $\mathrm{m\,s^{-1}}$.
In contrast to the calm case in February 2020, the simulation results from LES_Ctrl vary similar to the observation for the turbulent case in November 2019. However, the smallest and highest observed values are not captured by the model. Due to the strong temperature and moisture intrusions, the slow response of the sea-ice surface temperature is less recognizable for the changes in the atmosphere. Furthermore, the differences in the results for the specific humidity suggest that the model generally underestimates the specific humidity near the surface.

The means, standard deviation and results of the Welch test (Equations 7.1.1-7.1.5) for the meteorological variables from the observation and LES_Cice in 15-21 November 2019 are shown in Table 7.8. The degrees of freedom between observation and LES_Cice show a higher number of degrees of freedom for air temperature at 5 m and specific humidity than between the observation and LES_Ctrl. The t'-values and p-values show that there is no significant difference between the observation and LES_Cice and the null hypothesis holds.

Figure 7.28 shows the probability density distribution from the observations and LES_Cice, as well as the corresponding probability density distribution of the differences between observations and LES_Cice. The range of values is wider in LES_Cice than for the simulation results of LES_Ctrl (Figure 7.27). The probability density distribution of the differences shows smaller mean deviations between observation and model. The probability density distribution for the sea-ice surface temperature from LES_Cice

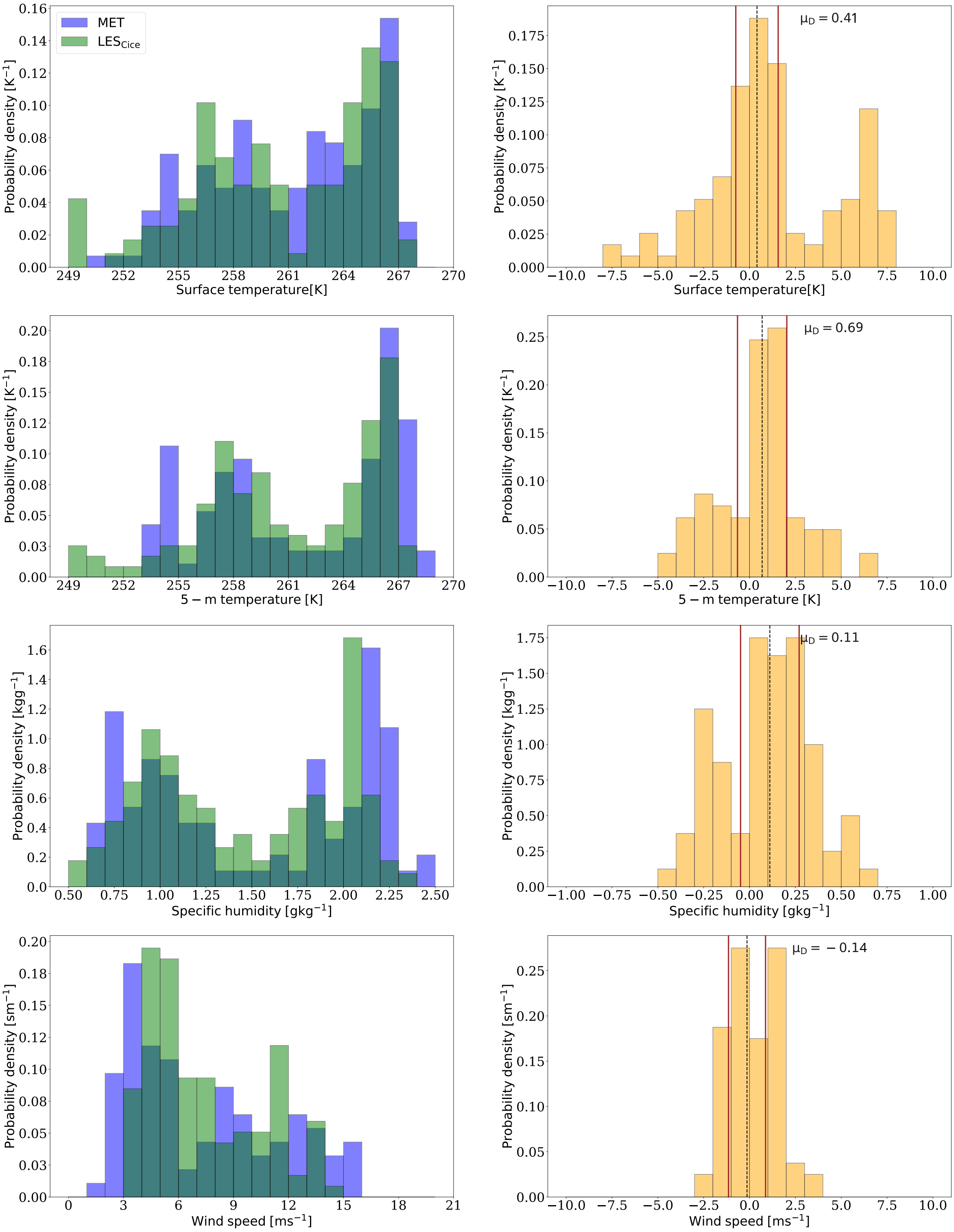

Figure 7.28: Probability density distribution (left) of sea-ice surface temperature, air temperature at 5 m, specific humidity at 5 m, and wind speed at 5 m (from top to bottom) from LES_Cice (green) and MOSAiC data (blue), and corresponding probability density distribution of the differences between LES_Cice and the observations (right), based on hourly data of the period 15-22 November 2019 at the mean Polarstern position. The dashed lines show the mean of the differences for each variable. The red lines show the 95% confidence interval.

Variable	μ_{obs}	s_{obs}	μ_{Ncice}	s_{Ncice}	ν	t'	p	μ_D
Surface temperature [K]	263.15	4.5	262.14	4.72	241	0.60	0.54	0.34
5 m temperature [K]	261.83	4.94	261.47	4.47	189.78	0.54	0.58	0.36
specific humidity [g kg^{-1}]	1.53	0.6	1.44	0.53	185.14	1.08	0.28	0.08
wind speed [m s^{-1}]	7.34	4.05	7.36	3.24	174	-0.04	0.96	-0.02

Table 7.9: Statistical values of different meteorological variables on 15-21 November 2019. Listed are the mean value μ_{obs} and the standard deviation s_{obs} from the observation, the mean value μ_{Ncice} and the standard deviation s_{Ncice} from LES_Ctrl, as well as their mean value of the differences μ_D. Bold values indicate that the difference between model and observation. The results of the statistical t-test include the number of degrees of freedom ν, the t-value t', and the p (probability that the null hypothesis is correct).

ranges between 249 K and 267 K, similar to the observation. LES_Cice shows colder values than was observed at 249 K. In general, the simulated sea-ice surface temperature is colder than the observation.
A similar probability density distribution between the observation and LES_Cice is shown for the air temperature at 5 m. The values from LES_Cice range between 249 K and 268 K and thus, are in general colder than the observation. The LES_Cice overestimates the observed air temperature at 5 m between 259 K and 266 K, as well as for low temperatures from 249 K to 253 K.
The probability density distribution for specific humidity at 5 m from LES_Cice ranges from 0.6 g kg^{-1} to 2.25 g kg^{-1}. The simulation is similar distributed as the observation, even if the range of values is somewhat shifted towards lower values. The simulated specific humidity is therefore slightly drier than was observed, but not as dry as in LES_Ctrl (Figure 7.27).
The wind speed at 5 m of the probability density distribution from LES_Cice ranges between 3 m s^{-1} and 15 m s^{-1} and is within the range of values as the observation. Higher and lower wind speeds are underestimated by LES_Cice, whereas values in the central section of the wind speed distribution are overestimated.
Similar to the period of calm weather in February 2020 (Section 7.4), the model underestimates the high observed values and overestimates the low observed values for each variable. This is related to the observed temperature drop, that was not captured by the model and the underrepresented warm-air mass intrusion between 17-19 November. The only exception is that the simulation overestimates the low observed wind speeds.

Table 7.9 shows the calculated mean values and their corresponding standard deviations, as well as the results of Welch's t-test (calculated by Equations 7.1.1-7.1.5) for the compared variables from the observation and NWP_Cice in 15-21 November 2019. It is striking that the difference between the means of the observation and NWP_Cice is not significant and smaller than between the other experiments (LES_Ctrl and LES_Cice).

Figure 7.29 shows the probability density distribution from the observations and NWP_Cice, as well as the probability density distribution of the difference between the observation and NWP_Cice. Similar to the simulations from LES_Cice (Figure 7.28), NWP_Cice shows a larger range of values than LES_Ctrl (Figure 7.27).
The probability density distribution of the sea-ice surface temperature from NWP_Cice ranges between 251 K and 268 K. Similar to the simulations from LES_Cice, the sea-ice surface temperature from NWP_Cice overestimates colder observed sea-ice surface temperatures. In contrast to LES_Cice, the lowest observed sea-ice surface temperature is

not obtained by NWP_Cice. Instead, the model overestimates the central section in the range of values. NWP_Cice also underestimates the largest observed sea ice temperatures. The probability density distribution of the differences between observation and NWP_Cice show the largest mean deviation at around 8 K.
The probability density distribution of the air temperature at 5 m from NWP_Cice ranges between 252 K and 268 K. The value range of the simulation is shifted towards lower values by around 1 K compared to the observation, but otherwise similar distributed to the observation. Except for the higher observed temperatures, NWP_Cice overestimates the central section of the range of values lower than 266 K. The mean deviation for the probability density distribution of the differences between observation and NWP_Cice is similar to LES_Cice. Therefore, NWP_Cice and LES_Cice show similar results for the air temperature at 5 m.
The probability density distribution of the specific humidity at 5 m from NWP_Cice shows values between 0.6 $\mathrm{g\,kg^{-1}}$ and 2.3 $\mathrm{g\,kg^{-1}}$ and is within the range of the observation. The simulation is similar to the observation. However, NWP_Cice slightly overestimates the low values and underestimates the high values.
The simulated probability density distribution for wind speed at 5 m from NWP_Cice ranges between 3 $\mathrm{m\,s^{-1}}$ and 15 $\mathrm{m\,s^{-1}}$ and and ranges within the observed wind speed like the model runs from above. Compared to the observation, the wind speed is slightly overestimated by the model. Similar to LES_Cice, NWP_Cice shows a higher distribution at lower values, but underestimates higher values. The probability density distribution of the differences between observation and NWP_Cice is on a similar range of values as LES_Cice.
Just like LES_Cice, NWP_Cice agrees better with the observation than LES_Ctrl. The simulated variables show similar values compared to the observation. NWP_Cice simulations confirm the improved agreement with observations due to the adapted sea-ice surface parameterization.

In contrast to the very calm weather case in February 2020 (Section 7.4), all simulations of the stormy weather situation in November 2019 are in good agreement with the observation. However, LES_Cice (Figure 7.28) and NWP_Cice (Figure 7.29) are in better agreement with the observations for than LES_Ctrl (Figure 7.27) because of the adapted sea-ice surface parametrization. Both models show less differences in the individual variables obtained. NWP_Cice is closer to the observation than LES_Cice, even if the differences are comparably small. Simulated wind speed shows similar ranges of values for all models. The comparison between LES_Cice and NWP_Cice shows that the choice of turbulence parameterization has a small effect on model performance for weather period of strong turbulence appearance.

7.5.2 Vertical profiles

Figure 7.30 shows the vertical profiles for the lower 50 m for the temperature from LES_Ctrl, LES_Cice, NWP_Cice, and the observations. The temperature profiles are selected where the observational data are complete and where the timing is close to one of the storm periods. The top two rows show the vertical profiles around the first storm on 16 November, followed by a colder period between 17 and 18 November. The fifth to sixth rows show the vertical profiles during the second storm on 19 November, followed by another colder day on 20 November. During the first storm on 16 November, the observed temperature profile near the surface reaches values between 266 K and 269 K,

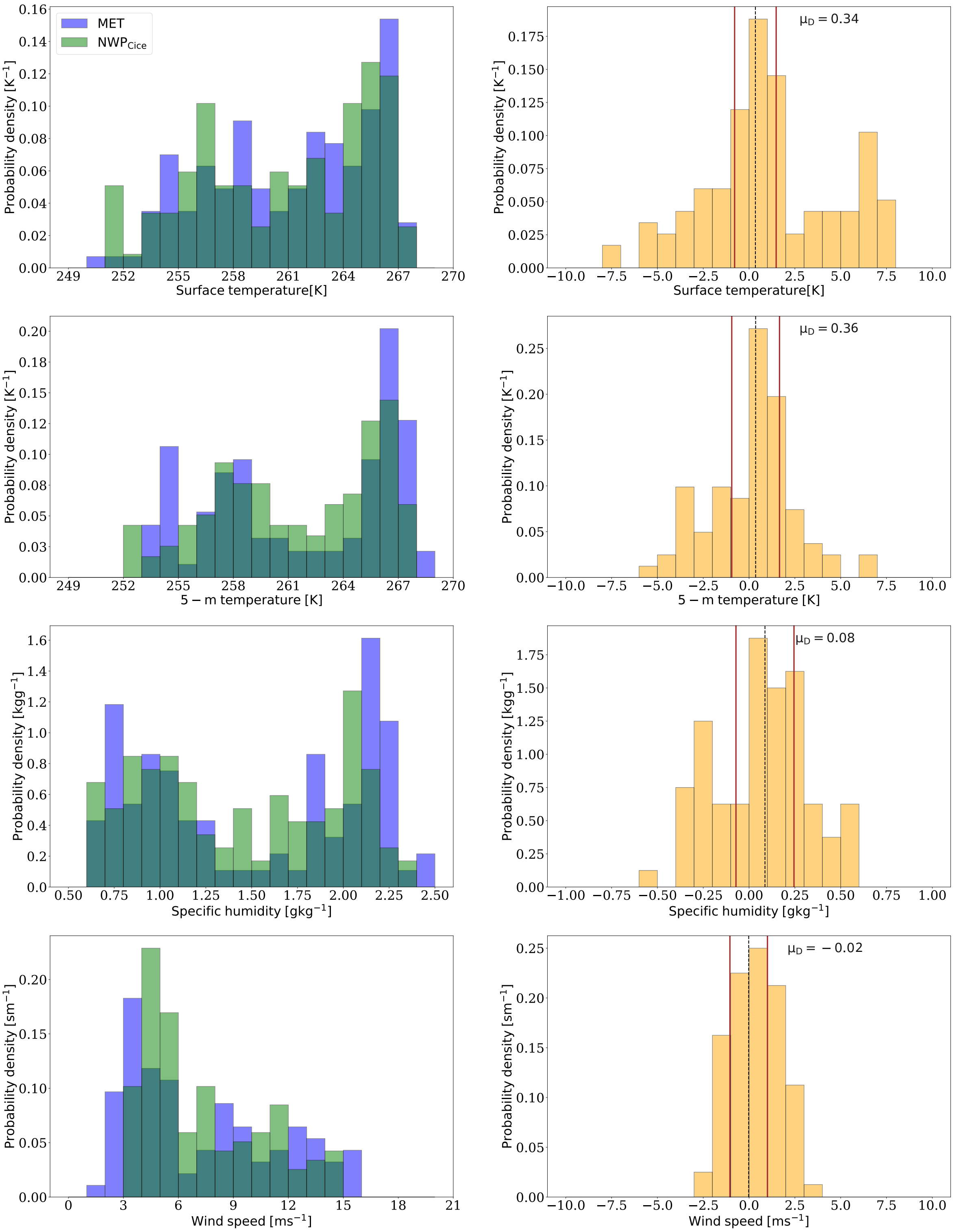

Figure 7.29: Probability density distribution (left) of sea-ice surface temperature, air temperature at 5 m, specific humidity at 5 m, and wind speed at 5 m (from top to bottom) from NWP_Cice (green) and MOSAiC data (blue), and corresponding probability density distribution of the differences between the simulations and the observations (right), based on hourly data of the period 15-22 November 2019 at the mean Polarstern position. The dashed lines show the mean of the differences for each variable. The red lines show the 95% confidence interval.

before dropping more than 10 K after the storm has passed the ship's position on 17 November. Temperatures begin to rise again around 258 K on 18 November. During the second storm, temperatures rise again to around 266 K on 19 November and fall to around 254 K on 20 November.
In general, the modeled temperatures are colder during the storm periods and too warm after the storms have passed. The simulation results from LES_Cice and NWP_Cice show a similar evolution to the observations. The deviation of the two modeled temperature profiles near the surface only differs by about 0.5 to 2 K from the observed temperature profile and is therefore in good agreement with the observation. The temperature profiles from NWP_Cice are slightly closer to the observation than those from LES_Cice for the first storm on 16 November. However, before and after the passage of the second storm on 18 November and 20 November, the near-surface temperatures of LES_Cice are closer to the observations than those of NWP_Cice. The change in vertical temperature profiles from LES_Ctrl is delayed during the change in events. The temperatures from LES_Ctrl are underestimated during the storms with deviations between 2 K and 4 K from the observation. The temperature drop after the first storm is not captured by LES_Ctrl. The model shows a temperature inversion with higher temperatures, whereas the opposite was observed on 17 November. As the second storm approaches at the end of 18 November, the changes in the temperature profiles of LES_Ctrl are much slower than those of LES_Cice and NWP_Cice, and therefore the modeled temperatures are about 6 K colder than the observations. After the second storm has passed on 20 November, the modeled temperature profile from LES_Ctrl is about 8 K warmer than the observation.

7.5.3 Surface fluxes

For the evaluation of the near-surface upwelling and downwelling radiation from LES_Ctrl, LES_Cice and NWP_Cice, the temporal evolution of the latent heat flux, the sensible heat flux, the upwelling long-wave radiation, the downwelling long-wave radiation, the drag coefficient and the bulk Richardson number at the surface are compared with the observations shown in Figure 7.31. As in the case of a stable stratified atmosphere (Section 7.4.3), the short-wave radiation is neglected due to the polar night. All model simulations strongly underestimate the downwelling long-wave radiation between 17 and 19 November. The values are about 40-90 $\mathrm{W\,m^{-1}}$ lower than the observations. During this period, low-level mixed-phase clouds were observed (consultation with Ola Persson and Matthew Shupe at the MOSAiC conference on 26 April 2022). However, these mixed-phase clouds were not resolved in ICON-LAM. Therefore, no advection of saturated air was transported into the domain of ICON-LEM, and thus no low-level clouds developed in the model (not shown here). This indicates that the performance of ICON-LEM is highly dependent on the lateral boundary conditions. A more detailed analysis of the discrepancies in the downwelling long-wave radiation, the state of the clouds and the water vapor concentration in the atmospheric boundary layer would be an interesting addition. However, the focus is on the interacting processes between the surface and the atmosphere, and a deeper analysis of the upper part of the atmospheric boundary layer is beyond the scope of this study and is therefore not discussed further. The simulation results for the upwelling long-wave radiation from LES_Cice and NWP_Cice are in better agreement with the observations than LES_Ctrl. For the sensible heat flux, the comparison between the observational and simulated results had to use da from 3.5 m height, so that the accuracy of their values could be affected. Throughout the whole

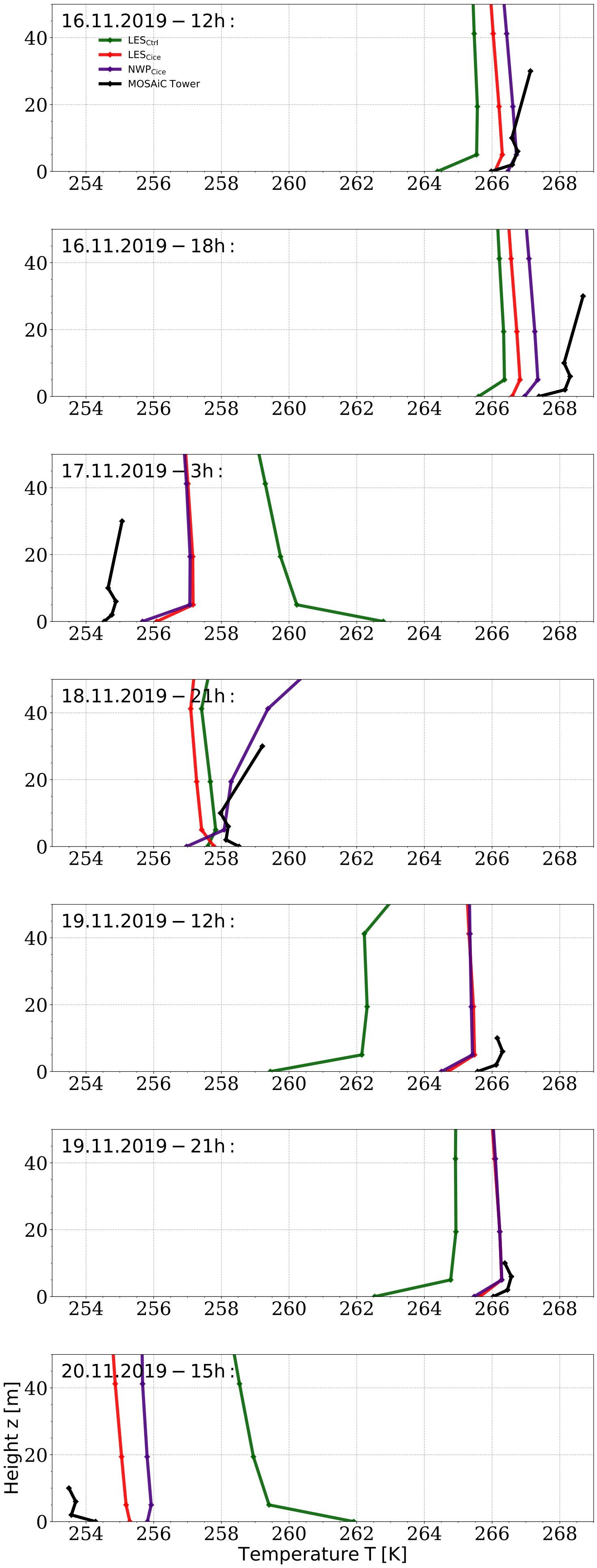

Figure 7.30: Vertical profiles of temperature from LES_Ctrl (green), LES_Cice (red), NWP_Cice (violet), and MOSAiC data (black) for specific times within the period 15-22 November 2019.

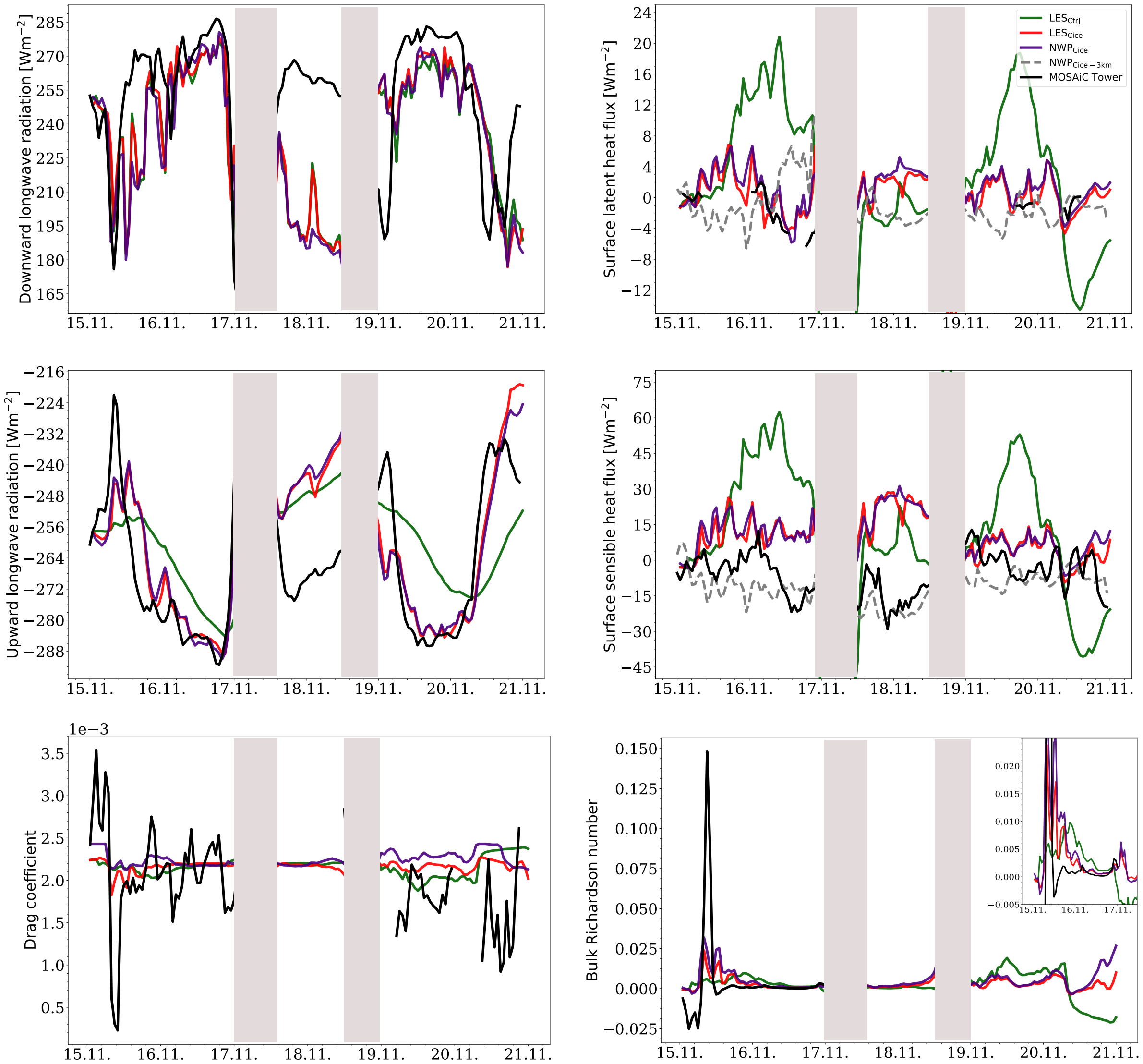

Figure 7.31: Temporal evolution of surface downwelling long-wave radiation (upper left), surface latent heat flux (upper right), surface upwelling long-wave radiation (middle left), surface sensible heat flux (middle right), surface drag coefficient (lower left), and surface bulk Richardson number (lower right) from LES_Ctrl (green), LES_Cice (red), NWP_Cice (violet), NWP_Cice-3km (grey), and MOSAiC data (black) in the period 15-22 November 2019.

simulation period, LES_Ctrl, LES_Cice and NWP_Cice overestimate the sensible heat flux compared to the observation. However, the sensible heat flux from NWP_Cice-3km seems to be in better agreement with the observation. The impact of the storms caused a breakdown of the instruments, where the turbulent heat fluxes closest to the surface were observed. For this reason, the latent heat flux measurements for that period are scarce. As mentioned in the previous section, the effect of the latent heat flux on the surface energy balance is comparatively small compared to the sensible heat flux. But also the calculated dimensionless drag coefficient C_d based on the observed momentum flux and the calculated bulk Richardson number Ri_b show some missing values as they depend on other variables like wind speed (Figure 7.26). The observed bulk Richardson number is incomplete and extends until 17 November. At the beginning of the observation on 15 November 2019 before noon, the observed bulk Richardson number decreases to a negative value at around $Ri_b = -0.025$, indicating an unstable atmospheric state. Just after noon, an exceptional peak in the observed bulk Richardson number appears with a value around $Ri_b = 0.15$. This peak refers to a stable environment between the surface and the atmosphere and appears just at the time when the temperature dropped to a minimum just before the arrival of the first storm (see Figure 7.26). Shortly before 16 November, the bulk Richardson number drops to around zero, indicating near-neutral atmospheric conditions, and remains in this state continuously. The model runs are not able to reproduce these rapid changes as observed for the bulk Richardson number, but LES_Cice and NWP_Cice seem to capture the changes with weaker increasing values and a small peak at around $Ri_b = 0.025$, thus showing a slightly stable atmospheric state, as can be seen in the enlargement of this figure. Furthermore, the simulations from LES_Cice and NWP_Cice reach near-neutral conditions with values around zero faster than LES_Ctrl. The bulk Richardson numbers of LES_Cice and NWP_Cice increase slightly after the first storm has passed between 17 and 18 November. LES_Ctrl shows rather unstable atmospheric conditions for this period with values below zero. The values of all model results show a slightly stable atmosphere with increasing values above $Ri_b = 0.025$ between 18 and 19 November before the second storm arrives. Between 19 and 21 November, the simulation results of LES_Cice and NWP_Cice are closer to the near-neutral atmospheric conditions than LES_Ctrl. For the short period at the beginning of this case study, the observed dimensional drag coefficient changes in proportion to the bulk Richardson number. The simulation results show a similar relationship between the two coefficients throughout the simulation period. However, all model results show lower values for the dimensionless drag coefficient and the bulk Richardson number compared to the observation. The dimensionless drag coefficient changes over a wider range of values for the observation, while all the simulation results show smaller changes with a rather constant temporal evolution at around $C_d = 2\times10^{-3}$. Compared to the other observational and simulation results, the drag coefficient determined from the observations shows an unusual behavior and is far from being interpretable.

The sea-ice surface temperature from the observations and the model simulations is plotted against the downwelling long-wave radiation in Figure 7.32. For the observations, the sea-ice surface temperature increases with increasing downwelling long-wave radiation. However, for all simulation results, the sea-ice surface temperatures remain almost constant below $240\,\mathrm{W\,m^{-1}}$ and increase with increasing downwelling long-wave radiation only above $240\,\mathrm{W\,m^{-1}}$. The simulated sea-ice surface temperatures, which increase linearly with the radiation, refer to the two storm phases. The colder temperatures refer to the period between the two storms on 17-19 November. In contrast to the observations, high sea-ice surface temperatures occur even with relatively low downwelling long-wave radiation.

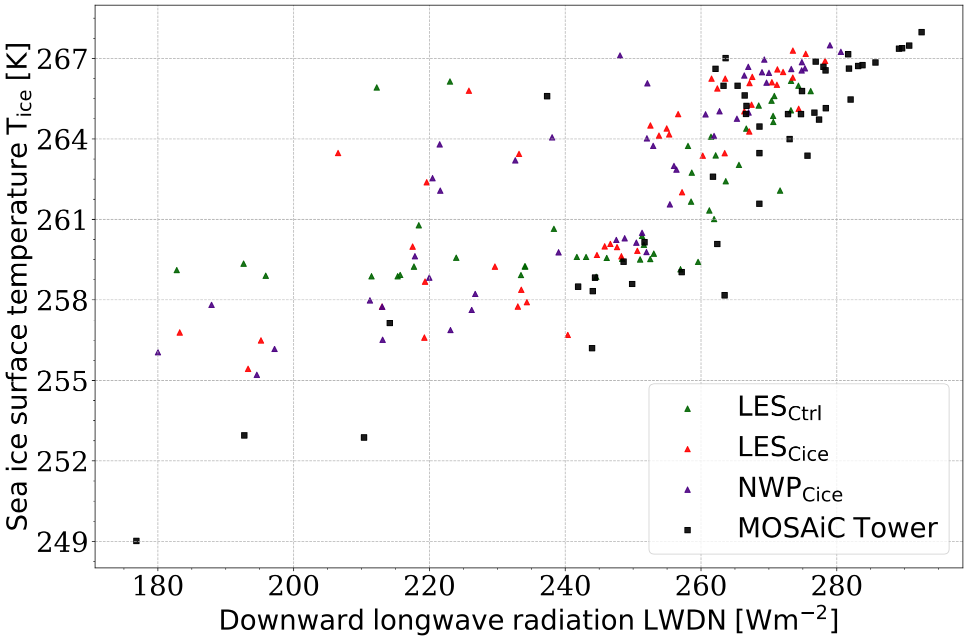

Figure 7.32: Sea-ice surface temperature as a function of surface downwelling long-wave radiation from LES_Ctrl (green crosses), LES_Cice (orange crosses), NWP_Cice (violet crosses), and MOSAiC data (black triangles) in the period 15-22 November 2019.

Figure 7.33 shows the sensible heat flux normalized to the wind speed at 5 m plotted against the temperature gradient $\Delta T = T(z*) - T_s$, where $z*$=5 m and the index s refers to the sea-ice surface. Results are shown for the observations, LES_Ctrl, LES_Cice and NWP_Cice. Similar to the case of February 2020 (Figure 7.23), the observations are characterized by two different regimes in the surface layer. In the first regime the temperature gradient dominates the heat flux and the atmosphere near the surface is characterized by a slightly unstable and a slightly stable stratification. In the second regime, the heat exchange coefficient dominates the heat flux and the atmosphere is characterized by increasing stability. In the first regime, the observations show a linearly decreasing scaled upward heat flux with small temperature gradients around slightly unstable (-1 K <ΔT < 0), neutral ($\Delta T = 0$) and slightly stable conditions ($\Delta T < 1\,K$). The upward normalized heat flux decreases continuously for increasing temperature gradients for slightly stable conditions up to a threshold of $\Delta T \approx 1\,K$. The second regime is associated with increasing stability in the surface layer. Only a few low scaled heat flux values (between -2 kgm^{-1} s^{-2} and 1 kgm^{-1} s^{-2}) remain for increasing temperature gradients as the surface layer is mostly determined by the heat and moisture intrusions.

All model runs are able to reproduce the linear relationship for small temperature gradients in the first regime as observed. The simulation results of LES_Ctrl and NWP_Cice continue the linear relationships without any changes in the slope and reach temperature gradients up to about ΔT = 2 K. LES_Cice is mostly localized at very small positive temperature gradients and normalized heat fluxes up to -2 kg m^{-1} s^{-2}. However, none of the models are able to produce a second regime of increasing atmospheric stability with increasing temperature gradients and decreasing scaled heat fluxes. Thus, the modeled heat fluxes are dominated only by the temperature gradients, leading to stronger vertical

heat exchange at the surface than for the observed (as can be seen for the sensible heat flux in Figure 7.31). For the February 2020 case, LES_Ctrl and LES_Cice were able to produce a delayed plateau with strong stability ($\Delta T > 2\,\mathrm{K}$). However, for the November 2019 case, the models do not extend temperature gradients higher than $\Delta T > 2\,\mathrm{K}$, so that LES_Ctrl and LES_Cice cannot reproduce a second regime.
The model simulation results from the November 2019 stormy weather case show that the model runs have difficulties in performing stable atmospheric conditions near the surface (Figure 7.33). This issue is again related to the surface transfer parameterization, where the stability dependent functions are based on transfer coefficients under neutral conditions. Both the February 2020 and the November 2019 case studies show that an adjustment to the stability dependent functions is required to allow earlier and faster convergence of the vertical heat exchange to lower values with increasing temperature gradients.

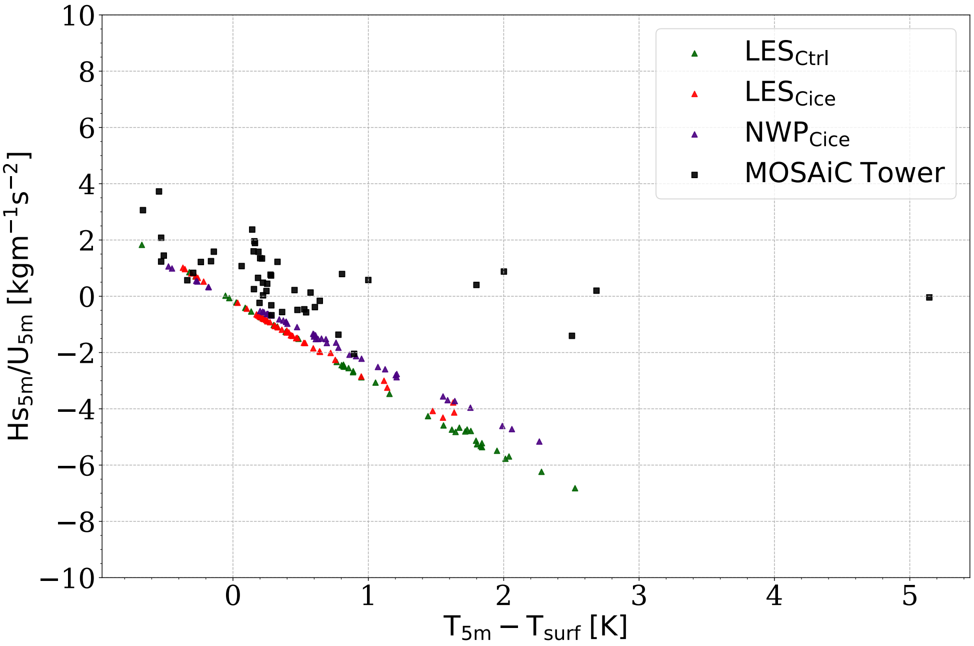

Figure 7.33: Sensible heat flux normalized with horizontal wind speed at 5 m as a function of the temperature difference between 5 m and the surface from LES_Ctrl (green crosses), LES_Cice (orange crosses), NWP_Cice (violet crosses), and MOSAiC data (black triangles) in the period 15-22 November 2019.

7.5.4 Boundary Layer height

Similar to Section 7.4.4, the bulk Richardson number is used as a measure of the PBLH. Equation 7.4.1 is used to calculate the bulk Richardson number. The result is shown in Figure 7.34, where the simulated height is compared with 6-hourly radiosonde data. During the hours of the first storm between 16 and 17 November, the PBLH increases, reaching a maximum of about 1.2 km above the surface between 17 and 18 November. All experiments are able to show a similar development, but have their maximum of the PBLH at an earlier time and at a slightly lower height. All simulation results are able to reproduce a PBLH similar to that observed. As the warm phase between 17 and 18 November is not recognized by any model, the simulated PBLH decreases faster after the first storm has passed and shows a much lower PBLH compared to the observation. During the second storm between 19 and 20 November, the simulated PBLH increases again for all simulations, but remains lower than the observation. In particular, the PBLH of LES_Ctrl is lower compared to the other model results and therefore less in agreement with the observation. With a lower PBLH than observed, the model results show that the atmosphere is less mixed.

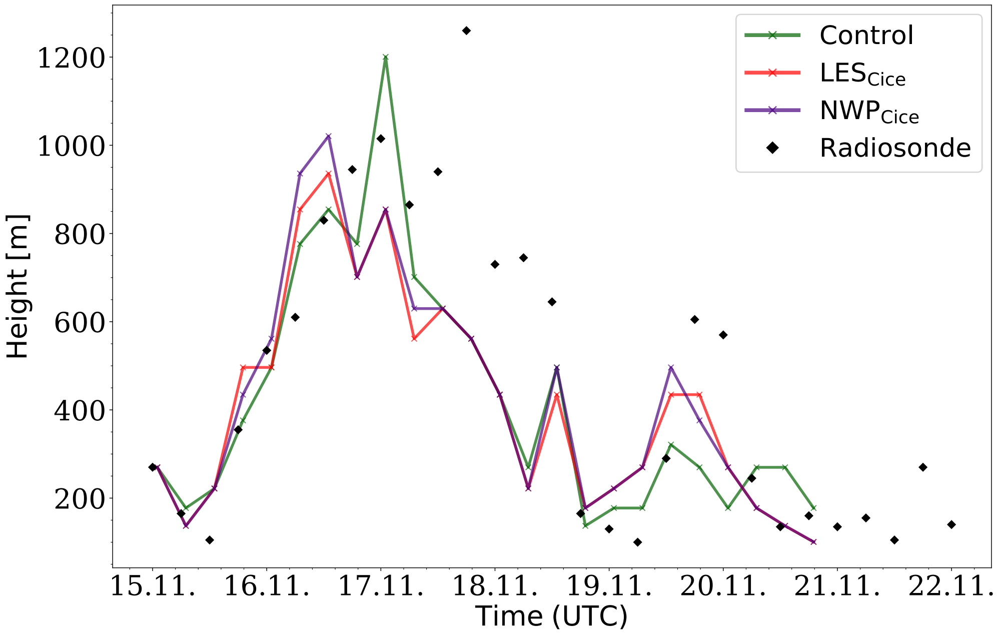

Figure 7.34: Temporal evolution of the boundary layer height from LES_Ctrl (green), LES_Cice (red), NWP_Cice (violet), and 6-hourly radiosonde data (diamonds) in the period 15-22 November 2019.

8. Discussion and Summary

In order to understand the changing Arctic and the related processes, it is important to study the atmospheric boundary layer in the central Arctic. The high-resolution mesoscale ICON-LEM is an unique model setup to resolve small-scale processes, which coarser forecast models cannot. High resolution climate models at the mesoscale of 100 m and 1 km have a high spatial resolution and can provide more detailed information on weather patterns and climate processes at the local level. However, they are also associated with computational challenges, data limitations, uncertainties, and mismatches between resolved and unresolved model components. As the model setup was applied in the central Arctic for the first time, the application implied many difficulties. During the course of the research, many model errors were discovered and had to be solved in order to make simulation results useable.

The lower atmospheric boundary layer was studied for two different weather conditions in the Arctic winter. In this chapter, the findings of the investigation are discussed, followed by a summary that concludes these findings and the overall performance of ICON-LEM in the central Arctic.

The results for all model configurations revealed, that the downwelling long-wave radiation was permanently underestimated in both, weak and strong turbulence case studies. Simulations of Arctic cloud processes and cloud properties continue to prove a significant issue in mesoscale models (e.g. Klaus et al., 2016; Rinke et al., 2006; Tjernström et al., 2005). As a consequence, low-level mixed-phase clouds cannot be reproduced and the downwelling long-wave radiation is misrepresented.

Further, the atmospheric boundary layer was not well presented by ICON with default settings (LES_Ctrl). The bulk thermodynamical sea-ice surface scheme implemented in ICON does not consider a snow layer on sea ice. This lead to very slow changes in the averaged surface temperature in relation to atmospheric changes. A new version of the heat capacity term was found for the rate of temperature change in the sea-ice surface scheme, which only considered the uppermost sea ice layer and thus, enabled a faster response of the sea-ice surface temperature to external forcing. The simulation results with the adapted sea-ice surface parameterization for two different turbulence closures (LES_Cice and NWP_Cice) of two different weather scenarios showed stronger fluctuations for the near-surface variables than LES_Ctrl. In particular, the model simulations for a case of weak turbulence during a rather calm weather period in February 2020 changed the model performances on various near-surface variables, and thus, had an impact on the whole atmospheric boundary layer. Further, the fluctuations from LES_Cice and NWP_Cice increased for a very strong turbulence case during a storm period in November 2019. Though, the effect of the adapted sea ice parametrization on the near-surface variables was smaller than in the case of weak turbulence, the variables still agreed better with

the observation than the results without the adaptation in LES_Ctrl. In an early stage during the investigation, similar results were obtained using the default settings of the NWP turbulence scheme (NWP_Ctrl) for comparison instead of the LES_Ctrl.
The new sea-ice parameterization is also suitable for coarser model resolutions, like the one used in regional and global model applications. Thus, the new sea-ice parametrization was used for the ICON-LAM with a 3 km gird-resolution (NWP_Cice-3km) that provided the lateral boundary conditions for ICON-LEM. The comparison of the surface variables showed that NWP_Cice-3km agreed better with the observation than without the adaptation. For future studies of the Arctic atmosphere with ICON, it would be beneficial to further develop the sea-ice parameterization to include a snow layer on the sea-ice surface (Heinemann et al., 2022).

The accurate representation of the sea-ice concentration in the central Arctic plays an important role in the study of the surface energy balance (Lüpkes et al., 2008a). The sea-ice surface in ICON was provided by the downscaled initial data from NWP_Cice-3km. This sea-ice surface structure did not consider leads, or rifts, or any other complex topography that was observed during the MOSAiC expedition. The model runs showed, that the plain sea-ice surface in ICON caused an overestimation of the near-surface heat fluxes and wind speed and an underestimation of the near surface temperature depending variables. With finer grid-resolution the accuracy of the lower boundary condition became more crucial. Especially cases of stably stratified atmosphere with weak turbulence depend on a finer sea-ice-ocean surface structure, as the occurrence of open water channels, e.g. leads have a major impact on the surface energy budget (Lüpkes et al., 2008b; Michaelis and Lüpkes, 2022).
An implementation of randomly placed open-water grid-points into the sea-ice surface allowed the study of the lower boundary layer under the assumption of more complex surface structures like leads. The presence of these open-water channels decreased the temperature difference near the surface for both weather periods, with calm weather in February 2020, and strong stormy weather in November 2019. The model results show that the influence of open water channels on the near surface variables varies in many degrees, depending on the weather situation, the lead size, and the overall boundary layer condition. By increasing the horizontal grid scale, a more complex circulation pattern for the wind field and thus, the turbulent flow becomes visible. However, to fully resolve the effect of leads under stable stratification, a specific turbulence parametrization for lead experiments is required, or much higher grid scales are needed to investigate the buoyancy fluxes and their subsequent decay of individual thermal eddies over plumes (Glendening and Burk, 1992).
The use of a high-resolution grid has several advantages as the implementation of leads or built-in water channels is easier to archive. The latter one could promise to be a better solution on studying the influence of complex sea-ice surface structures on the Arctic boundary layer. As the evaluation of the MOSAiC data progresses, the completion of an on site measured sea-ice surface map is increasingly likely and could be implemented into the lateral boundary conditions. Both proposals would be interesting examples for future high-resolution studies in the central Arctic.

The simulation results from LES_Cice for a cold period of weak turbulence in February 2020 were in best agreement with the observations compared to the other model results. The comparison of both turbulence schemes showed that a high resolution and a sub-grid scale parametrization are crucial for modeling cold weather situations with weak turbulence. For a stormy period in November 2019, the differences between both turbulence closures and various mesoscale horizontal grid-resolutions were less pronounced. However, the sea-ice surface temperature from LES_Cice still agrees best with the observation. The atmospheric forcing was much stronger and turbulent mixing was not only influenced by the surface itself, but rather by the approaching temperature and moisture intrusion of the much stronger passing cyclones. Thus, increasing horizontal grid-resolution does not necessarily lead to a better model performance. For both weather scenarios the model runs converged with increasing height for the atmospheric boundary layer.

All model runs had difficulties to simulate small-scale turbulence for very stable atmospheric conditions as was observed. However, LES_Ctrl and LES_Cice were able to reproduce a regime of lower turbulence with increasing temperature gradients. NWP_Cice was compensating the temperatures close to the surface and showed a large overestimation for the sensible heat flux. The coarser NWP_Cice-3km showed the strongest deviation from the observation. The main difference between the two turbulence closures is the treatment of the turbulence length-scale. Unlike NWP_Cice, the turbulence length-scale in LES_Cice is increasing proportional to the grid volume. With other words, the finer the horizontal grid-resolution the smaller the sub-grid length scale, e.g. the size of the eddies. However, with increasing horizontal grid-resolution a more realistic sea-ice surface structure also becomes essential. Altough recognizable differences are only likely to play a noticeable role below 10 m for large eddy simulations, the simulation results show how important the choice of grid-resolution and turbulence parameterization is for studying boundary layer interactions during cold weather periods.

It is well known that the stability dependent functions and their counterpart, the stability correction functions based on the Monin-Obukhov similarity theory (MOST) have a large uncertainty and many different versions exist, which are all based on well accepted turbulence data. This has been described in much detail, e.g. by Gryanik et al. (2020, 2021) and Gryanik and Lüpkes (2022). The existence of a regime with small turbulence under stable conditions in the surface boundary layer has also been the topic of many publications and depends on the value of the critical Richardson number Ri_{crit} (e.g. (Grachev et al., 2013)). Using functions of Dyer and Businger turbulence decreases to zero for stability above Ri_{crit}, but other functions allow a certain level of remaining turbulence, which is different for different approaches.

The impact of the parameterization schemes under cold, light wind conditions have been studied by Rinke et al. (2012); Tjernström et al. (2005) and they also pointed to the importance of a realistic parameterization in strongly stable conditions. This topic is related also to the possible decoupling of atmosphere and sea ice in which is often a drawback of models. In addition, large eddy simulations (LES) with sufficient grid scales to resolve energy-containing eddies suffer from discrepancies between observed and modeled surface temperatures due to overestimated surface heat fluxes (e.g. Kosović and Curry (2000); van der Linden and Ansorge (2022)). To avoid strong large variations, many LES models use semi-idealized boundary conditions (e.g. Neggers et al. (2019)), where either the surface temperature is kept constant, or the vertical profiles are generated.

Testing such parameterizations requires high costs when iterative schemes with stability functions dependent on the Obukhov length L are used. One possible solution was found for LES models by Maronga et al. (2020), where they improved the shear stress and heat fluxes calculation based on MOST by introducing an elevated level in the surface layer, instead of being limited to the first grid level above surface. Recently, Gryanik and Lüpkes (2018, 2022) developed a universal non-iterative scheme that can be used with many different state-of-the-art stability corrections dependent on the bulk Richardson number instead of using L. The set of functions includes functions allowing only little turbulence for strong stability (like those of Gryanik et al. (2021); Zilitinkevich et al. (2013); Zilitinkevich and Esau (2007). Thus their test in ICON looks promising (see also Schneider et al. (2021)), but this work is beyond the scope of this thesis and should be done in future work.

ICON-LEM was applied to investigate different weather scenarios during the polar night. The findings show how sensitive Arctic surface temperatures and thus turbulent heat fluxes are to changes in the downwelling radiation, model physic, horizontal grid-resolution, lower boundary conditions, and heat capacity of sea ice during polar winter. The aim of this thesis was to analyze the ICON-LEM performance on low boundary conditions during polar night. The results indicate the need of an extended sea-ice parameterization, a complex sea-ice surface condition, and a adapted stability correction term in case of very stable atmospheric stratification to represent the exchange processes in the boundary layer according to the observation. The high grid-resolution and the resolving large eddy turbulence parameterization enables the investigation of stable stratified atmospheric conditions. However, the model performance is limited for the study of strong and very weak turbulence with the used model configuration. The increasing of the horizontal grid-scale and the implementation of a high resolution sea-ice map offers new opportunities. The influence of rifts and leads on the Arctic boundary layer can be investigated in the context of a non-idealized model setup. The recently developed bulk Richardson number depending stability functions for the surface layer opens the perspective to enable weak turbulent mixing under very strong stable stratification.

This study shows how important boundary layer investigations are in order to better comprehend and further develop the existing parametrizations. The findings of this thesis help to improve even coarser model setups in ICON for the studies in the Arctic region and enhance our understanding about forecasting Arctic climate processes in the atmospheric boundary layer during polar night.

Acknowledgements

The successful completion of this thesis is credited to the contribution and support of many people. As the funded project is related to the MOSAiC expedition, many people deserve my gratitude for giving me the unique opportunity to work on this exciting project. My very sincerest thanks goes to my supervisor, Professor Markus Rex. I appreciate that he selected me and that he entrusted me with this challenging research topic at the Alfred Wegener Institute (AWI) in Potsdam. Moreover, I am very grateful to him for his support in the versatility of my scientific career that not only included the deepening education of a climate modeler, but also the training of going to expeditions. I would also like to extend my sincere thanks to my co-supervisor Professor Roel Neggers, who encouraged me with his expert knowledge in our meetings. Special thanks goes to Professor Günther Heinemann, with whom I had some inspiring discussions over the modeling challenges of regional models in the Arctic.

I would like to express my utmost gratitude to my mentor Wolfgang Dorn, who guided me throughout my whole PhD. He always had an open door for me and our countless hours of conversation helped me a lot not to lose sight of the task at hand. I am also deeply indebted to Christof Lüpkes. Together with Wolfgang and Christof, we had many fruitful discussions and their valuable insights in modeling problems and unique expertise in measuring campaigns helped me a lot to successfully complete my PhD project. Thanks should also go to Annette Rinke for her many kind and motivating words. With this I would like to thank all members of the whole TAC meeting committee again. The regular discussion rounds between all the experts were very helpful in solving the many challenges I was facing during my PhD.

Moreover, I would like to thank the many colleagues at AWI who have supported me in many ways. My profound gratitude goes to Hélène Bresson, with whom I had the most discussions about the initially staging of a new model setup and the many related challenges and who later provided with the important downscaled global forecasts. Special thanks goes also to Ines Hebestadt for continuing to provide me the downscaled boundary conditions and helping me in answering many technical questions. The implementation of ICON-LEM would not have been successful without the help of Vera Schemann and Daniel Reinert. Both of them guided me through the many technical model issues and configuration problems at the beginning of my project. Therefore, I am sincerely thankful. My warmest thanks goes to Sara Khosravi for the support that we gave each other during our final stages of our PhD. Special thanks goes also to Marie-Louise Zeller, Lena Pfister, Jannis-Michael Huss, Raphael Köhler, Katrin Müller, Sandro Dahlke, Samantha Pasowicz, Ingo Timm, and many others who I had the pleasure of working with.

Many special thanks goes to all the people who made the realization of the project possible. At this point, I would like to thank Professor Klaus Dethloff for initiating the project. Thanks should also go to all the contributors of the MOSAiC expedition who carried out the measurements and provided me with the necessary data to compare my model results, as well as given me the background knowledge of the measuring sites. This includes special thanks to Marion Maturilli and her Team at our institute, which provided me with Radiosonde data for the first comparison to the model output. I would also like to extend my sincere thanks to the people from the University of Colorado/ NOAA surface flux team under Matthew Shupe for the near-surface meteorology and surface energy flux measurements that were carried out and processed.

Lastly, I would be remiss in not to mention my partner Andrea for encouraging me unconditionally, my sister Cornelia for always giving me good advises and support, my parents and friends in cheering me through all those years and different phases of my life.

Many institutions, external agencies and stakeholders from more than 20 countries were financially involved into the succession of this unique expedition. The Multidisciplinary drifting Observatory for the Study of Arctic Climate (MOSAiC) was led by AWI and a significant funding was raised by the German Federal Ministry of Education and Research (BMBF). Funding for the meteorological sites was contributed from the National Science Foundation, Department of Energy, NOAA and NASA. Sea-ice concentration from 2019 to 2020 originating from `https://www.meereisportal.de` (Funding: REKLIM-2013-04).

Appendix

A. Averaging Methods

In 1895 Reynolds introduced the concept of averaging, which was generally used to describe the "mean" value of an equation. The averaging can be performed in two ways, e.g. over an integral-form, or over a sum-form. In both forms the mean of a quantity is governed through spatial, temporal, or ensemble averaging. In context of averaging the dynamic of a fluid, fluctuations are getting smoothed out during the temporal evolution by assuming they only exist in a short period of time T_1 within the significant longer temporal evolution T_2 of the flow. For the velocity component $u_i(\mathbf{x}, t)$ the mean of a velocity is than

$$\overline{u}_i(\mathbf{x}) = \underbrace{lim}_{T\to\infty} \frac{1}{T}\int_t^{t+T} u_i(\mathbf{x}, t)dt, \tag{.0.1}$$

$$= \frac{1}{T}\int_t^{t+T} u_i(\mathbf{x}, t)dt,\ T_1 << T << T_2, \tag{.0.2}$$

whereas the fluctuation is given by

$$u_i'(\mathbf{x}, t) = u_i(\mathbf{x}, t) - \overline{u}_i(\mathbf{x}). \tag{.0.3}$$

This relation includes that the mean on the fluctuation causes its assumed disappearance

$$\overline{u}_i'(\mathbf{x}, t) = \underbrace{lim}_{T\to\infty} \frac{1}{T}\int_t^{t+T} [u_i(\mathbf{x}, t) - \overline{u}_i(\mathbf{x})] = \overline{u}_i(\mathbf{x}) - \overline{u}_i(\mathbf{x}) = 0. \tag{.0.4}$$

The Reynolds averaging in eq. .0.2 counts only for the ideal case of a stationary turbulent flows, where fluctuations are short lived compared to a long time period and do not disturb the evolution of a steady mean flow. However, in cases of unsteady flows, where mean and turbulent components are connected, their time-averaged product does not vanish. In meteorology, for example, this is known as the spectral gap problem (Wilcox, 2006). The Large Eddy Simulations deals with those unsteady flows. Regarding to this, another filter method will be discussed in section 3.

For simplicity reasons we define

$$\phi(\mathbf{x}, t) = \phi_t \tag{.0.5}$$

$$\phi(\mathbf{x}) = \phi. \tag{.0.6}$$

The product of two mean quantities, like two velocity components, works as follows:

$$\overline{u_{i,t}u_{j,t}} = \overline{(\overline{u}_i + u_i')(\overline{u}_j + u_j')} \tag{.0.7}$$

$$= \overline{\overline{u}_i\overline{u}_j} + \overline{\overline{u}_i u_j'} + \overline{u_i'\overline{u}_j} + \overline{u_i'u_j'} \tag{.0.8}$$

$$= u_i u_j + \overline{u_i'u_j'}, \tag{.0.9}$$

The product of a mean quantity and a turbulent quantity is zero like in eq. .0.4. If the turbulent components of the product are correlated it follows $\overline{u_i' u_j'} \neq 0$, otherwise $\overline{u_i' u_j'} = 0$ (e.g. Wilcox, 2006). For a triple product it is similar:

$$\overline{u_{i,t} u_{j,t} u_{k,t}} = u_i u_j u_k + u_i \overline{u_j' u_k'} + \overline{u_i' u_j'} u_k + \overline{u_i' u_k'} u_j + \overline{u_i' u_j' u_k'}. \qquad (.0.10)$$

B. Measurement discrepancies

During MOSAiC many measurements of the same variable at different heights were carried out. In the ideal case, a simulated variable would be compared to the exact observational counterpart. However, the atmospheric level in the model does not always corresponded to the measuring height. For instance, the calculated observational sensible heat flux was not measured directly at the surface, but the same output variable in ICON represents the surface sensible heat flux. With increasing height, the near-surface variables, which are a measure from the surface radiation towards the upper atmosphere are influenced by the intermediate atmospheric layer. Further, observational instruments were impacted by external forces, e.g. strong turbulent winds and maintenance procedures. Thus, one has to examine the same variable for different height and locations to ensure its credibility. Here, the comparison of the sensible heat flux is shown as an example. Unfortunately, the error value is missing in the calculation of the observations.

Figure 1 shows the temporal evolution of the observed sensible heat flux at 2 m, 6 m, 10 m, from the 10 m-Tower and at 3.5 m from the ASFS40 in 6-10 February 2020. The observed sensible heat flux shows many fluctuations for each height. The curve of the sensible heat flux at 2 m differs the most from the rest of the curves.

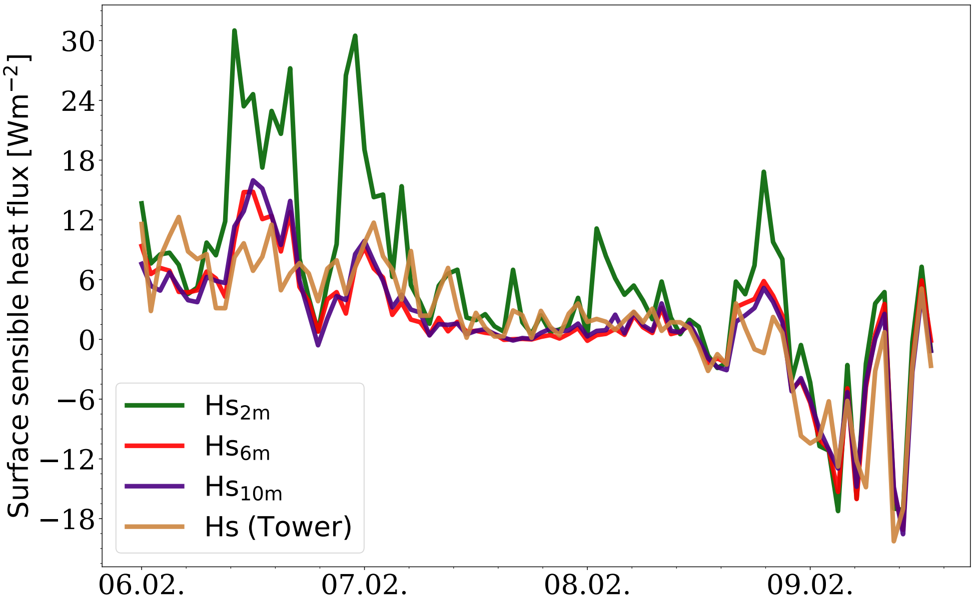

Figure 1: Temporal evolution of sensible heat flux from the 10 m-Tower, at around 2 m (green), at around 6 m (red), at around 10 m (violet) and from ASFS30 data at around 3.5 m (brown) in the period 6-10 February 2020.

Figure 2 shows the temporal evolution of the observed sensible heat flux at 2 m, 6 m, 10 m, from the 10 m-Tower, and at 3.5 m from the ASFS30 station on 15-21 November

2019. Due to the strong storm events, the data of the ASFS40-Tower is partly missing. However, the variables at different heights seem to agree well, a the course of the curves is close to each other.

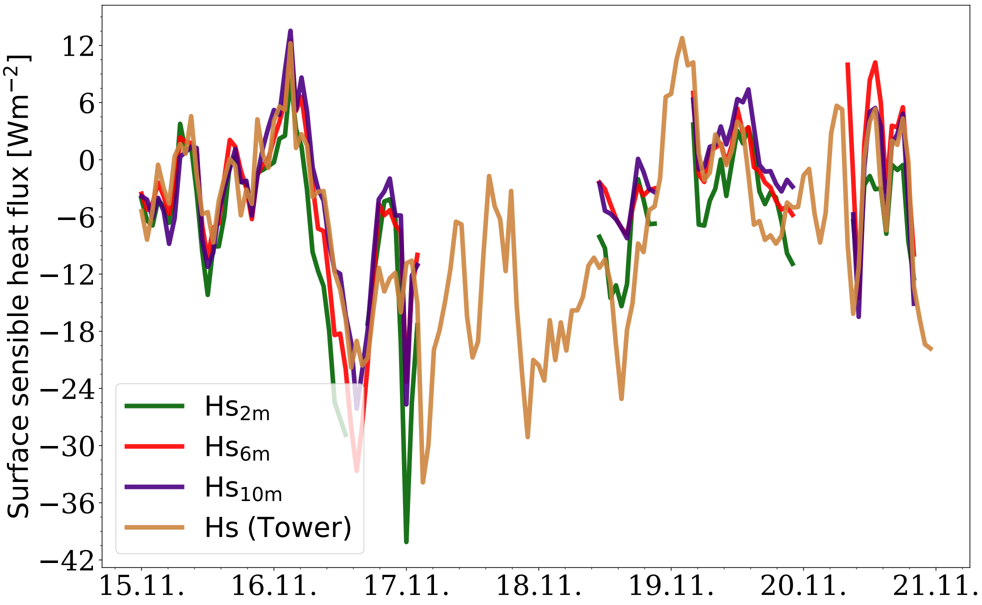

Figure 2: Temporal evolution of sensible heat flux from the 10 m-Tower at around 2 m (green), at around 6 m (red), at around 10 m (violet) and from the ASFS30 data at around 3.5 m (brown) in the period 15-21 November 2019.

C. Impact of the horizontal resolution

For te sake of completeness, the simulation results for the sea-ice surface temperature, air temperature at 5 m, specific humidity, and wind speed from NWP_Cice-800 and from NWP_Cice-100 are shown in this section. The simulation results show a somewhat similar behavior as the LES_Cice-800 and LES_Cice-100 in Section 7.1.

Figure 3 shows the temporal evolution of the meteorological variables from NWP_Cice-800 and NWP_Cice-100 in 6-10 February 2020. The variables from NWP_Cice-800 have slightly higher values than the ones from NWP_Cice-100. However, the differences between both model resolutions is comparably small. The additional simulation result for the sea-ice surface temperature from NWP_Cice-3km is lower between 6-7 and 8-9 February compared to the other simulation results and shows a bit higher values between 7-8 February.

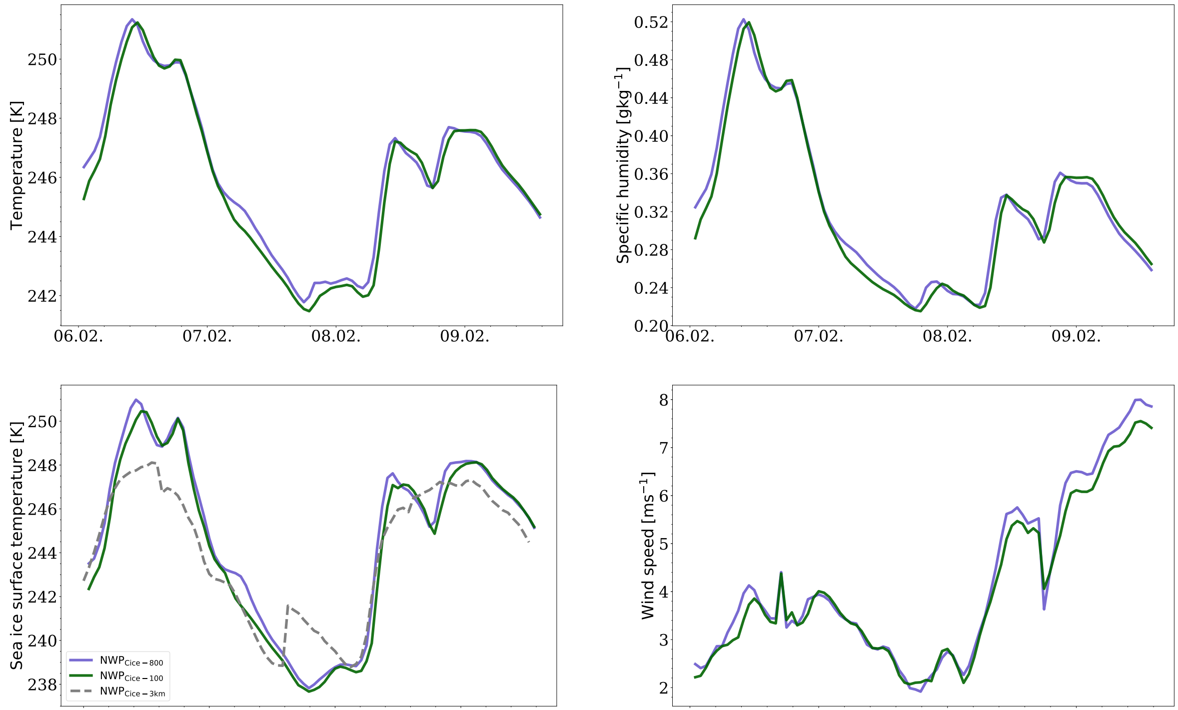

Figure 3: Temporal evolution of 5-m temperature (upper left), sea-ice surface temperature (lower left), specific humidity (upper right), and wind speed (lower right) from NWP_Cice-800 (blue), NWP_Cice-100 (green), and NWP_Cice-3km (grey) in the period 6-10 February 2020.

Figure 4 shows the probability density distribution from NWP_Cice-800 and from NWP_Cice-100 and the corresponding probability density distribution of the differences between both model setups for the same period in February 2020. The difference distribution is calculated by subtracting NWP_Cice-100 from NWP_Cice-800. Further, the expected value μ (calculated after eq. 7.1.1) and the sample standard deviation s (calculated after eq. 7.1.2) are also shown for the difference distribution. The model results show that NWP_Cice-800 and NWP_Cice-100 are on same range of values for each variable. However, the variables from NWP_Cice-800 show slightly higher values.

Figure 5 shows the temporal evolution of the meteorological variables from NWP_Cice-800 and NWP_Cice-100 in 15-21 November 2019. The simulation results of both resolutions do not differ much. The course of the curves is lying on top of each other most of the

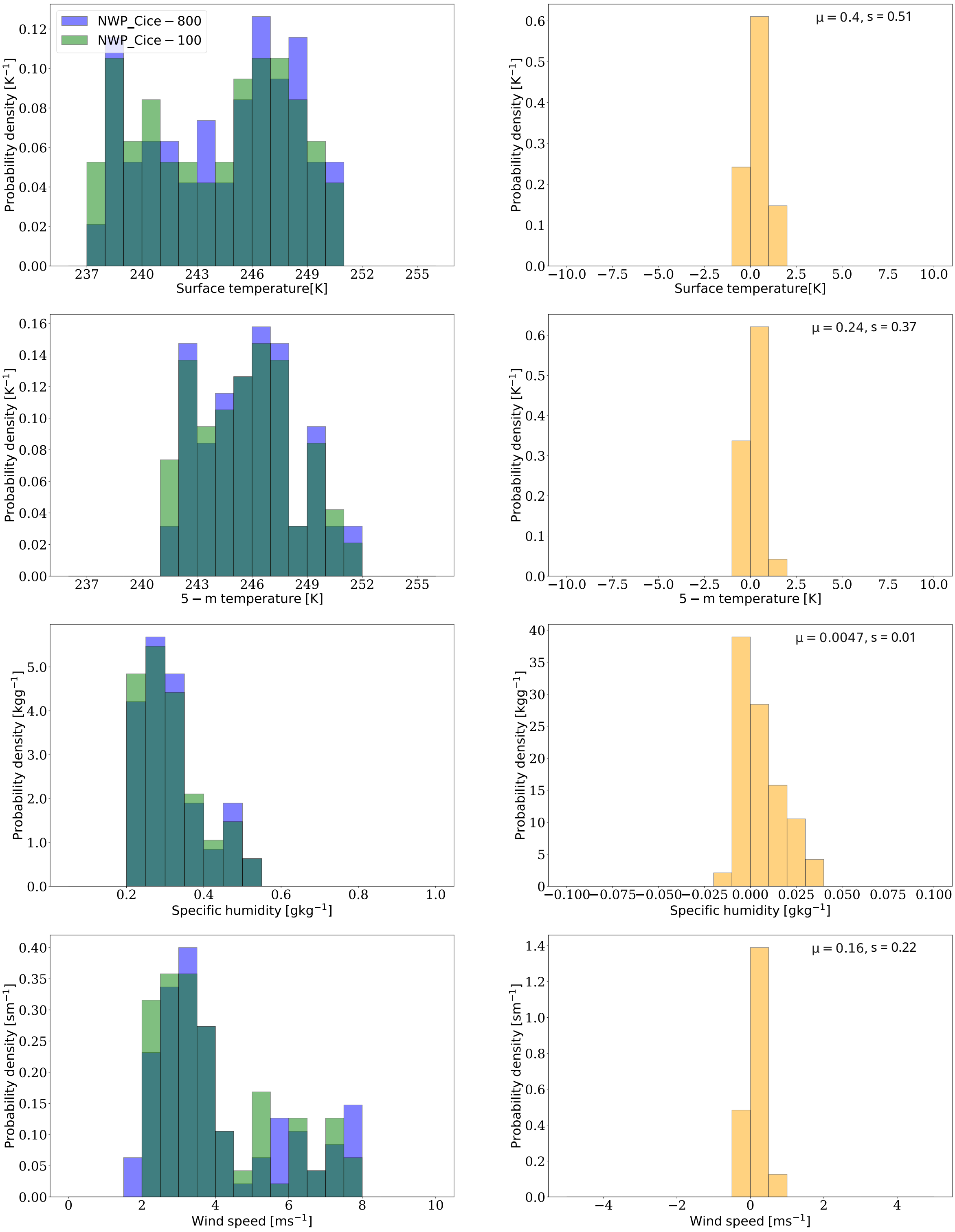

Figure 4: Probability density distribution (left) of sea-ice surface temperature, air temperature at 5 m, specific humidity at 5 m, and wind speed at 5 m (from top to bottom) from the simulations with NWP_Cice-800 (blue) and NWP_Cice-100 (green), and corresponding probability density distribution of the differences between the simulations with NWP_Cice-800 and NWP_Cice-100 (right), based on hourly data of the period 6-10 February 2020 at the mean Polarstern position.

times. Small exceptions can be seen for the air temperature at 5 m, were NWP_Cice-800 shows somewhat higher values for the colder phase around 19 November. Additionally, the wind speed is a bit higher from NWP_Cice-800 between 16-18 November. The additional sea-ice surface temperature from NWP_Cice-3km is very close to the other model runs.

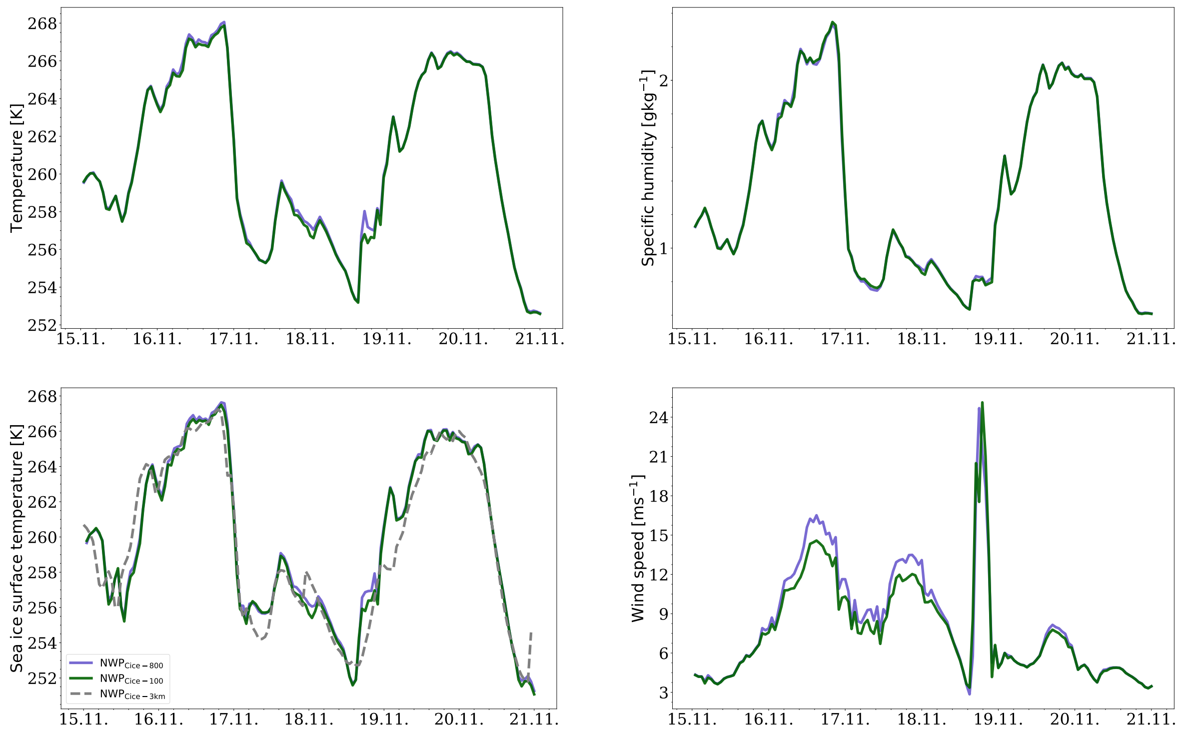

Figure 5: Temporal evolution of 5-m temperature (upper left), sea-ice surface temperature (lower left), specific humidity (upper right), and wind speed (lower right) from NWP_Cice-800 (blue), NWP_Cice-100 (green), and NWP_Cice-3km in the period 15-21 November 2019.

Figure 6 shows the probability density distribution from NWP_Cice-800 and from NWP_Cice-100 and the corresponding probability density distribution of the differences between both model setups for the same period in November 2019. The difference distribution is calculated by subtracting NWP_Cice-100 from NWP_Cice-800. Further, the expected value μ (calculated after eq. 7.1.1) and the sample standard deviation s (calculated after eq. 7.1.2) are also shown for the difference distribution. The model results show that NWP_Cice-800 and NWP_Cice-100 are on same range of values for each variable. However, some of the near-surface temperatures from NWP_Cice-100 are slightly higher than from NWP_Cice-800.

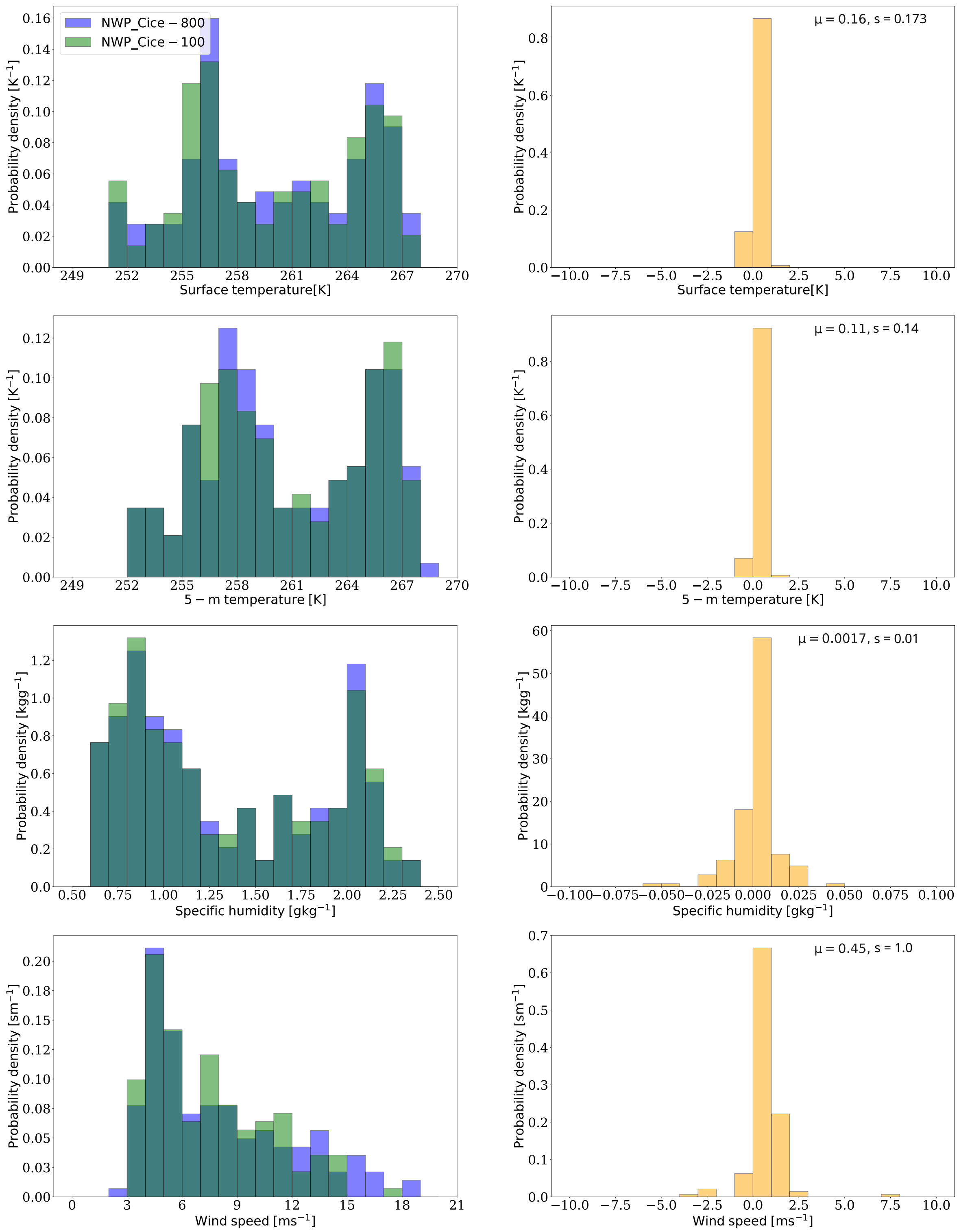

Figure 6: Probability density distribution (left) of sea-ice surface temperature, 5 m temperature, 5 m specific humidity, and 5 m wind speed (from top to bottom) from the simulations with NWP_Cice-800 (blue) and NWP_Cice-100 resolution (green), and corresponding probability density distribution of the differences between the simulations NWP_Cice-800 and NWP_Cice-100 (right), based on hourly data of the period 15-21 November 2019 at the mean Polarstern position.

Bibliography

Abrams, M. . The advanced spaceborne thermal emission and reflection radiometer (aster): data products for the high spatial resolution imager on nasa's terra platform. *international Journal of Remote sensing*, 21(5):847–859, 2000. doi:10.1080/014311600210326.

Abrams, M. , Tsu, H. , Hulley, G. , Iwao, K. , Pieri, D. , Cudahy, T. , and Kargel, J. . The advanced spaceborne thermal emission and reflection radiometer (aster) after fifteen years: review of global products. *International Journal of Applied Earth Observation and Geoinformation*, 38:292–301, 2015. doi:10.1016/j.jag.2015.01.013. URL `https://www.glims.org/glacierdata/data/lit_ref_files/abrams2015_aster_at_15.pdf`.

Ahad, N. A. and Yahaya, S. S. S. . Sensitivity analysis of Welch's t-Test. In *AIP Conference proceedings*, volume 1605, pages 888–893. American Institute of Physics, 2014. doi:10.1063/1.4887707.

Andreas, A. , Dooraghi, M. , Habte, A. , Kutchenreiter, M. , Reda, I. , and Sengupta, M. . *Solar Infrared Radiation Station (SIRS), SkyRadiation (SKYRAD), Ground Radiation (GNDRAD),and Broadband Radiometer Station (BRS)Instrument Handbook*. U.S. Department of Energy - Office of Science, 2018. URL `https://www.arm.gov/capabilities/instruments/skyrad`.

Andreas, E. L. , Hill, R. J. , Gosz, J. R. , Moore, D. I. , Otto, W. D. , and Sarma, A. D. . Statistics of surface-layer turbulence over terrain with metre-scale heterogeneity. *Boundary-Layer Meteorology*, 86:379–408, 1998. doi:10.1023/A:1000609131683.

Baldauf, M. , Klocke, D. , Köhler, M. , Mironov, D. , Prill, F. , Reinert, D. , and Zängl, G. . *ICON-NWP Scientific Documentation*, Nov. 2020.

Blackadar, A. K. . The vertical distribution of wind and turbulent exchange in a neutral atmosphere. *Journal of Geophysical Research*, 67(8):3095–3102, 1962. doi:10.1029/JZ067i008p03095.

Bresson, H. , Rinke, A. , Mech, M. , Reinert, D. , Schemann, V. , Ebell, K. , Maturilli, M. , Viceto, C. , Gorodetskaya, I. , and Crewell, S. . Case study of a moisture intrusion over the Arctic with the ICOsahedral Non-hydrostatic (ICON) model: resolution dependence of its representation. *Atmospheric Chemistry and Physics*, 22(1):173–196, 2022. doi:10.5194/acp-22-173-2022.

Bulatovic, I. , Savre, J. , Tjernström, M. , Leck, C. , and Ekman, A. M. . Large-eddy simulation of a two-layer boundary-layer cloud system from the arctic ocean 2018 expedition.

Atmospheric Chemistry and Physics Discussions, pages 1–29, 2022. doi:10.5194/acp-2022-809.

Businger, J. A. , Wyngaard, J. C. , Izumi, Y. , and Bradley, E. F. . Flux-profile relationships in the atmospheric surface layer. *Journal of Atmospheric Sciences*, 28(2):181–189, 1971. doi:10.1175/1520-0469(1971)028<0181:FPRITA>2.0.CO;2.

Chow, F. K. , Schär, C. , Ban, N. , Lundquist, K. A. , Schlemmer, L. , and Shi, X. . Crossing multiple gray zones in the transition from mesoscale to microscale simulation over complex terrain. *Atmosphere*, 10(5):274, 2019. doi:10.3390/atmos10050274.

Clough, S. A. , Iacono, M. J. , and Moncet, J.-L. . Line-by-line calculations of atmospheric fluxes and cooling rates: Application to water vapor. *Journal of Geophysical Research: Atmospheres*, 97(D14):15761–15785, 1992. doi:10.1029/92JD01419.

Cohen, J. , Screen, J. A. , Furtado, J. C. , Barlow, M. , Whittleston, D. , Coumou, D. , Francis, J. , Dethloff, K. , Entekhabi, D. , Overland, J. , et al. Recent Arctic amplification and extreme mid-latitude weather. *Nature geoscience*, 7(9):627–637, 2014. doi:10.1038/NGEO2234.

Cook, D. and Sullivan, R. . *Eddy Correlation Flux Measurement System (ECOR) Instrument Handbook*. U.S. Department of Energy - Office of Science, 2020. URL `https://www.arm.gov/capabilities/instruments/ecor`.

Cox, C. , Gallagher, M. , Shupe, M. , Persson, O. , Solomon, A. , Ayers, T. , Costa, D. , Hutchings, J. , Leach, J. , Morris, S. , et al. Atmospheric surface flux station# 30 measurements (level 1 raw), multidisciplinary drifting observatory for the study of arctic climate (mosaic), central arctic, october 2019–september 2020. *Arctic Data Center. DOI: http://dx. doi. org/10.18739/A20C4SM1J*, 2021a. doi:10.18739/A20C4SM1J.

Cox, C. , Gallagher, M. , Shupe, M. , Persson, O. , Solomon, A. , Ayers, T. , Costa, D. , Hutchings, J. , Leach, J. , Morris, S. , et al. Atmospheric surface flux station# 40 measurements (level 2, version 3), multidisciplinary drifting observatory for the study of arctic climate (mosaic), central arctic, october 2019–september 2020. *Arctic Data Center. DOI: http://dx. doi. org/10.18739/A20C4SM1J*, 2021b. doi:10.18739/A2CJ87M7G.

Cox, C. , Gallagher, M. , Shupe, M. , Persson, O. , Solomon, A. , Ayers, T. , Costa, D. , Hutchings, J. , Leach, J. , Morris, S. , et al. Atmospheric surface flux station# 30 measurements (level 1 raw), multidisciplinary drifting observatory for the study of arctic climate (mosaic), central arctic, october 2019–september 2020. *Arctic Data Center. DOI: http://dx. doi. org/10.18739/A20C4SM1J*, 2021c. doi:10.18739/A20C4SM1J.

Cox, C. , Gallagher, M. , Shupe, M. , Persson, O. , Solomon, A. , Blomquist, B. , Brooks, I. , Costa, D. , Gottas, D. , Hutchings, J. , et al. 10-meter (m) meteorological flux tower measurements (level 1 raw), multidisciplinary drifting observatory for the study of arctic climate (mosaic), central arctic, october 2019–september 2020. *Arctic Data Center. DOI: http://dx. doi. org/10.18739/A2VM42Z5F*, 2021d. doi:10.18739/A2VM42Z5F.

Davies, H. C. . A lateral boundary formulation for multi-level prediction models. *Quarterly Journal of the Royal Meteorological Society*, 102(432):405–418, 1976. doi:10.1002/qj.49710243210.

Davies, H. C. . Limitations of some common lateral boundary schemes used in regional NWP models. *Monthly Weather Review*, 111(5):1002–1012, 1983. doi:10.1175/1520-0493(1983)111<1002:LOSCLB>2.0.CO;2.

Dethloff, K. , Handorf, D. , Jaiser, R. , Rinke, A. , and Klinghammer, P. . Dynamical mechanisms of Arctic amplification. *Annals of the New York Academy of Sciences*, 1436 (1):184–194, 2019. doi:10.1111/nyas.13698.

Deutscher Wetterdienst. ICON - das globale Wettervorhersagemodell, änderungsmitteilungen. Technical report, 2021. URL `availableat:https://www.dwd.de/DE/fachnutzer/forschung_lehre/numerische_wettervorhersage/nwv_aenderungen/_functions/DownloadBox_modellaenderungen/icon/pdf_2021/pdf_icon_14_04_2021.html;jsessionid=FD8D222F2B83E5DDFC90A120F87BCB17.live31083?nn=346840,lastaccess:17.04.2023`.

Dimitrelos, A. , Ekman, A. M. , Caballero, R. , and Savre, J. . A Sensitivity Study of Arctic Air-Mass Transformation using Large Eddy Simulation. *Journal of Geophysical Research: Atmospheres*, 125(6):e2019JD031738, 2020. doi:10.1029/2019JD031738.

Dipankar, A. , Stevens, B. , Heinze, R. , Moseley, C. , Zängl, G. , Giorgetta, M. , and Brdar, S. . Large eddy simulation using the general circulation model ICON. *Journal of Advances in Modeling Earth Systems*, 7(3):963–986, 2015. doi:10.1002/2015MS000431.

Doms, G. , Förstner, J. , Heise, E. , Herzog, H. , Mironov, D. , Raschendorfer, M. , Reinhardt, T. , Ritter, B. , Schrodin, R. , Schulz, J.-P. , et al. *A description of the non-hydrostatic regional COSMO model*, 2021. URL `http://www.cosmo-model.org/content/model/cosmo/coreDocumentation/cosmo_physics_4.20.pdf`.

Egerer, U. , Ehrlich, A. , Gottschalk, M. , Griesche, H. , Neggers, R. A. , Siebert, H. , and Wendisch, M. . Case study of a humidity layer above arctic stratocumulus and potential turbulent coupling with the cloud top. *Atmospheric Chemistry and Physics*, 21(8):6347–6364, 2021. doi:10.5194/acp-21-6347-2021.

Fahrmeir, L. , Heumann, C. , Künstler, R. , Pigeot, I. , and Tutz, G. . *Statistik: Der weg zur Datenanalyse*, volume 8. Springer-Verlag, 2016. doi:10.1007/978-3-662-50372-0.

Favre, A. . Statistical equations of turbulent gases (Statistical equations for compressible gas, discussing turbulent quantities separated into fluctuating and macroscopic parts). *Problems of hydrodynamics and continuum mechanics*, pages 231–266, 1969. doi:10.1007/978-1-4612-2792-2_23.

Feltz, M. , Borbas, E. , Knuteson, R. , Hulley, G. , and Hook, S. . The combined ASTER and MODIS emissivity over land (CAMEL) global broadband infrared emissivity product. *Remote Sensing*, 10(7):1027, 2018. doi:10.3390/rs10071027.

Foken, T. and Napo, C. J. . *Closure Techniques, In: Micrometeorology*, volume 2. Springer Berlin, Heidelberg, 2008. doi:10.1007/978-3-540-74666-9.

Gassmann, A. . A global hexagonal C-grid non-hydrostatic dynamical core (ICON-IAP) designed for energetic consistency. *Quarterly Journal of the Royal Meteorological Society*, 139(670):152–175, 2013. doi:10.1002/qj.1960.

Gassmann, A. and Herzog, H.-J. . Towards a consistent numerical compressible non-hydrostatic model using generalized Hamiltonian tools. *Quarterly Journal of the Royal Meteorological Society*, 134(635):1597–1613, 2008. doi:10.1002/qj.297.

Giorgetta, M. A. , Brokopf, R. , Crueger, T. , Esch, M. , Fiedler, S. , Helmert, J. , Hohenegger, C. , Kornblueh, L. , Köhler, M. , Manzini, E. , et al. Icon-a, the atmosphere component of the icon earth system model: I. model description. *Journal of Advances in Modeling Earth Systems*, 10(7):1613–1637, 2018. doi:10.1029/2017MS001233.

Glendening, J. W. and Burk, S. D. . Turbulent transport from an arctic lead: A large-eddy simulation. *Boundary-layer meteorology*, 59(4):315–339, 1992. doi:10.1007/BF02215457.

Goessling, H. F. , Jung, T. , Klebe, S. , Baeseman, J. , Bauer, P. , Chen, P. , Chevallier, M. , Dole, R. , Gordon, N. , Ruti, P. , et al. Paving the way for the year of polar prediction. *Bulletin of the American Meteorological Society*, 97(4):ES85–ES88, 2016. doi:10.1175/BAMS-D-15-00270.1.

Goger, B. , Rotach, M. W. , Gohm, A. , Fuhrer, O. , Stiperski, I. , and Holtslag, A. A. . The impact of three-dimensional effects on the simulation of turbulence kinetic energy in a major alpine valley. *Boundary-layer meteorology*, 168:1–27, 2018. doi:10.1007/s10546-018-0341-y.

Goger, B. , Rotach, M. W. , Gohm, A. , Stiperski, I. , Fuhrer, O. , and De Morsier, G. . A new horizontal length scale for a three-dimensional turbulence parameterization in mesoscale atmospheric modeling over highly complex terrain. *Journal of Applied Meteorology and Climatology*, 58(9):2087–2102, 2019. doi:10.1175/JAMC-D-18-0328.1.

Grachev, A. A. , Andreas, E. L. , Fairall, C. W. , Guest, P. S. , and Persson, P. O. G. . The critical Richardson number and limits of applicability of local similarity theory in the stable boundary layer. *Boundary-layer meteorology*, 147(1):51–82, 2013. doi:10.1007/s10546-012-9771-0.

Gryanik, V. M. and Lüpkes, C. . An efficient non-iterative bulk parametrization of surface fluxes for stable atmospheric conditions over polar sea-ice. *Boundary-layer meteorology*, 166(2):301–325, 2018. doi:10.1007/s10546-017-0302-x.

Gryanik, V. M. and Lüpkes, C. . A Package of Momentum and Heat Transfer Coefficients for the Stable Surface Layer Extended by New Coefficients over Sea Ice. *Boundary-Layer Meteorology*, pages 1–32, 2022. doi:10.1007/s10546-022-00730-9.

Gryanik, V. M. , Lüpkes, C. , Grachev, A. , and Sidorenko, D. . New modified and extended stability functions for the stable boundary layer based on SHEBA and parametrizations of bulk transfer coefficients for climate models. *Journal of the Atmospheric Sciences*, 77(8):2687–2716, 2020. doi:10.1175/JAS-D-19-0255.1.

Gryanik, V. M. , Lüpkes, C. , Sidorenko, D. , and Grachev, A. . A universal approach for the non-iterative parametrization of near-surface turbulent fluxes in climate and weather prediction models. *Journal of Advances in Modeling Earth Systems*, page e2021MS002590, 2021. doi:10.1029/2021MS002590.

Gryschka, M. , Fricke, J. , and Raasch, S. . On the impact of forced roll convection on vertical turbulent transport in cold air outbreaks. *Journal of Geophysical Research: Atmospheres*, 119(22):12–513, 2014. doi:10.1002/2014JD022160.

Hastings, D. A. and Dunbar, P. . Development & assessment of the global land one-km base elevation digital elevation model (GLOBE). *Group*, 4(6):218–221, 1998. doi:10.7289/V52R3PMS.

Heinemann, G. , Willmes, S. , Schefczyk, L. , Makshtas, A. , Kustov, V. , and Makhotina, I. . Observations and simulations of meteorological conditions over Arctic thick sea ice in late winter during the Transarktika 2019 expedition. *Atmosphere*, 12(2):174, 2021. doi:10.3390/atmos12020174.

Heinemann, G. , Schefczyk, L. , Willmes, S. , and Shupe, M. D. . Evaluation of simulations of near-surface variables using the regional climate model cclm for the mosaic winter period. *Elementa*, 10(1), 2022. doi:10.1525/elementa.2022.00033.

Heinze, R. , Dipankar, A. , Henken, C. C. , Moseley, C. , Sourdeval, O. , Trömel, S. , Xie, X. , Adamidis, P. , Ament, F. , Baars, H. , et al. Large-eddy simulations over Germany using ICON: A comprehensive evaluation. *Quarterly Journal of the Royal Meteorological Society*, 143(702):69–100, 2017. doi:10.1002/qj.2947.

Hellsten, A. , Ketelsen, K. , Sühring, M. , Auvinen, M. , Maronga, B. , Knigge, C. , Barmpas, F. , Tsegas, G. , Moussiopoulos, N. , and Raasch, S. . A Nested Multi-Scale System Implemented in the Large-Eddy Simulation Model PALM model system 6.0. *Geoscientific Model Development Discussions*, pages 1–45, 2020. doi:10.5194/gmd-2020-222.

Hesselberg, T. . Die Gesetze der ausgeglichenen atmosphärischen Bewegungen. *Beiträge zur Physik der Atmosphäre*, 12:141–160, 1926. URL `http://www.ngfweb.no/docs/NGF_GP_Vol05_no4.pdf`.

Hogan, R. J. and Bozzo, A. . *ECRAD: A new radiation scheme for the IFS*. European Centre for Medium-Range Weather Forecasts, 2016. URL `https://www.ecmwf.int/sites/default/files/elibrary/2016/16901-ecrad-new-radiation-scheme-ifs.pdf`.

Hogan, R. J. and Bozzo, A. . A Flexible and Efficient Radiation Scheme for the ECMWF model. *Journal of Advances in Modeling Earth Systems*, 10(8):1990–2008, 2018. doi:10.1029/2018MS001364.

Hunke, E. , Allard, R. , Blain, P. , Blockley, E. , Feltham, D. , Fichefet, T. , Garric, G. , Grumbine, R. , Lemieux, J.-F. , Rasmussen, T. , et al. Should sea-ice modeling tools designed for climate research be used for short-term forecasting? *Current Climate Change Reports*, 6(4):121–136, 2020. doi:10.1007/s40641-020-00162-y.

IPCC. *Summary for Policymakers*, book section Possible Climate Futures. Cambridge University Press, Cambridge, United Kingdom and New York, NY, USA, 2021. doi:10.1017/9781009157896.001.

King, J. , Howell, S. , Brady, M. , Toose, P. , Derksen, C. , Haas, C. , and Beckers, J. . Local-scale variability of snow density on arctic sea ice. *The Cryosphere*, 14(12): 4323–4339, 2020. doi:10.5194/tc-14-4323-2020.

Kiszler, T. , Ebell, K. , and Schemann, V. . A performance baseline for the representation of clouds and humidity in cloud-resolving icon-lem simulations in the arctic. *Journal of Advances in Modeling Earth Systems*, 15(5):e2022MS003299, 2023. doi:10.1029/2022MS003299.

Klaus, D. , Dethloff, K. , Dorn, W. , Rinke, A. , and Wu, D. . New insight of Arctic cloud parameterization from regional climate model simulations, satellite-based, and drifting station data. *Geophysical research letters*, 43(10):5450–5459, 2016. doi:10.1002/2015GL067530.

Knust, R. . Polar research and supply vessel POLARSTERN operated by the Alfred-Wegener-Institute. *Journal of large-scale research facilities*, 3:119, 2017. doi:10.17815/jlsrf-3-163.

Kolmogorov, A. N. and Tikhomirov, V. M. . ε-entropy and ε-capacity of sets in function spaces. *Uspekhi Matematicheskikh Nauk*, 14(2):3–86, 1959. URL `https://www.mathnet.ru/php/getFT.phtml?jrnid=rm&paperid=7289&what=fullt&option_lang=eng`.

Kosović, B. and Curry, J. A. . A large eddy simulation study of a quasi-steady, stably stratified atmospheric boundary layer. *Journal of the atmospheric sciences*, 57(8):1052–1068, 2000. doi:10.1175/1520-0469(2000)057<1052:ALESSO>2.0.CO;2.

Krumpen, T. , von Albedyll, L. , Goessling, H. F. , Hendricks, S. , Juhls, B. , Spreen, G. , Willmes, S. , Belter, H. J. , Dethloff, K. , Haas, C. , et al. MOSAiC drift expedition from October 2019 to July 2020: Sea ice conditions from space and comparison with previous years. *The Cryosphere*, 15(8):3897–3920, 2021. doi:10.5194/tc-15-3897-2021.

Lee, S. S. and Donner, L. J. . Effects of cloud parameterization on radiation and precipitation: A comparison between single-moment microphysics and double-moment microphysics. *TAO: Terrestrial, Atmospheric and Oceanic Sciences*, 22(4):4, 2011. doi:10.3319/TAO.2011.03.03.01(A).

Leuenberger, D. , Koller, M. , Fuhrer, O. , and Schär, C. . A generalization of the SLEVE vertical coordinate. *Monthly Weather Review*, 138(9):3683–3689, 2010. doi:10.1175/2010MWR3307.1.

Lilly, D. K. . On the numerical simulation of buoyant convection. *Tellus*, 14(2):148–172, 1962. doi:10.1111/j.2153-3490.1962.tb00128.x.

Lohmann, G. . Temperatures from energy balance models: the effective heat capacity matters. *Earth System Dynamics*, 11(4):1195–1208, 2020. doi:10.5194/esd-11-1195-2020.

Louis, J.-F. . A parametric model of vertical eddy fluxes in the atmosphere. *Boundary-Layer Meteorology*, 17(2):187–202, 1979. doi:10.1007/BF00117978.

Lüpkes, C. , Gryanik, V. M. , Witha, B. , Gryschka, M. , Raasch, S. , and Gollnik, T. . Modeling convection over arctic leads with les and a non-eddy-resolving microscale model. *Journal of Geophysical Research: Oceans*, 113(C9), 2008a. doi:10.1029/2007JC004099.

Lüpkes, C. , Vihma, T. , Birnbaum, G. , and Wacker, U. . Influence of leads in sea ice on the temperature of the atmospheric boundary layer during polar night. *Geophysical Research Letters*, 35(3), 2008b. doi:10.1029/2007GL032461.

Mann, H. B. and Whitney, D. R. . On a Test of Whether one of Two Random Variables is Stochastically Larger than the Other. *The Annals of Mathematical Statistics*, 18(1): 50 – 60, 1947. doi:10.1214/aoms/1177730491.

Maronga, B. , Gryschka, M. , Heinze, R. , Hoffmann, F. , Kanani-Sühring, F. , Keck, M. , Ketelsen, K. , Letzel, M. O. , Sühring, M. , and Raasch, S. . The Parallelized Large-Eddy Simulation Model (PALM) version 4.0 for atmospheric and oceanic flows: model formulation, recent developments, and future perspectives. *Geoscientific Model Development*, 8(8):2515–2551, 2015. doi:10.5194/gmd-8-2515-2015.

Maronga, B. , Knigge, C. , and Raasch, S. . An improved surface boundary condition for large-eddy simulations based on Monin-Obukhov similarity theory: Evaluation and consequences for grid convergence in neutral and stable conditions. *Boundary-Layer Meteorology*, 174(2):297–325, 2020. doi:10.1007/s10546-019-00485-w.

Maturilli, M. , Holdridge, D. J. , Dahlke, S. , Graeser, J. , Sommerfeld, A. , Jaiser, R. , Deckelmann, H. , and Schulz, A. . Initial radiosonde data from 2019-10 to 2020-09 during project MOSAiC. 2021. doi:10.1594/PANGAEA.928656.

Mauritsen, T. . *On the Arctic Boundary Layer : From Turbulence to Climate*. PhD thesis, Department of Meteorology, Stockholm University, 2007. URL `http://su.diva-portal.org/smash/record.jsf?pid=diva2:196700&dswid=-8405`.

Meador, W. and Weaver, W. . Two-stream approximations to radiative transfer in planetary atmospheres: A unified description of existing methods and a new improvement. *Journal of Atmospheric Sciences*, 37(3):630–643, 1980. doi:10.1175/1520-0469(1980)037<0630:TSATRT>2.0.CO;2.

Mellor, G. L. and Yamada, T. . Development of a turbulence closure model for geophysical fluid problems. *Reviews of Geophysics*, 20(4):851–875, 1982. doi:10.1029/RG020i004p00851.

Michaelis, J. and Lüpkes, C. . The Impact of Lead Patterns on Mean Profiles of Wind, Temperature, and Turbulent Fluxes in the Atmospheric Boundary Layer over Sea Ice. *Atmosphere*, 13(1):148, 2022. doi:10.3390/atmos13010148.

Michaelis, J. , Lüpkes, C. , Schmitt, A. U. , and Hartmann, J. . Modelling and parametrization of the convective flow over leads in sea ice and comparison with airborne observations. *Quarterly Journal of the Royal Meteorological Society*, 147(735): 914–943, 2021. doi:10.1002/qj.3953.

Middlemas, E. , Kay, J. , Medeiros, B. , and Maroon, E. . Quantifying the influence of cloud radiative feedbacks on Arctic surface warming using cloud locking in an Earth system model. *Geophysical Research Letters*, 47(15):e2020GL089207, 2020. doi:10.1029/2020GL089207.

Mirocha, J. , Lundquist, J. , and Kosović, B. . Implementation of a nonlinear subfilter turbulence stress model for large-eddy simulation in the Advanced Research WRF model. *Monthly Weather Review*, 138(11):4212–4228, 2010. doi:10.1175/2010MWR3286.1.

Mironov, D. , Ritter, B. , Schulz, J.-P. , Buchhold, M. , Lange, M. , and MacHulskaya, E. . Parameterisation of sea and lake ice in numerical weather prediction models of the German Weather Service. *Tellus A: Dynamic Meteorology and Oceanography*, 64(1): 17330, 2012. doi:10.3402/tellusa.v64i0.17330@zela20.2016.68.issue-s1.

Mlawer, E. J. , Taubman, S. J. , Brown, P. D. , Iacono, M. J. , and Clough, S. A. . Radiative transfer for inhomogeneous atmospheres: RRTM, a validated correlated-k model for the longwave. *Journal of Geophysical Research: Atmospheres*, 102(D14): 16663–16682, 1997. doi:10.1029/97JD00237.

Monin, A. and Obukhov, A. . Basic laws of turbulent mixing in the surface layer of the atmosphere. *Contrib. Geophys. Inst. Acad. Sci. USSR*, 151(163):163–187, 1954.

Neggers, R. , Chylik, J. , Egerer, U. , Griesche, H. , Schemann, V. , Seifert, P. , Siebert, H. , and Macke, A. . Local and remote controls on arctic mixed-layer evolution. *Journal of Advances in Modeling Earth Systems*, 11(7):2214–2237, 2019. doi:10.1029/2019MS001671.

Neske, S. . *Towards an improved Turbulence Closure Scheme by analysing ICON Model Simulations*. PhD thesis, Universität zu Köln, 2017. URL `https://kups.ub.uni-koeln.de/7565/`.

Nicolaus, M. , Perovich, D. K. , Spreen, G. , Granskog, M. A. , von Albedyll, L. , Angelopoulos, M. , Anhaus, P. , Arndt, S. , Belter, H. J. , Bessonov, V. , et al. Overview of the MOSAiC expedition: Snow and sea ice. *Elem Sci Anth*, 10(1):000046, 2022. doi:10.1525/elementa.2021.000046.

Ori, D. , Schemann, V. , Karrer, M. , Dias Neto, J. , von Terzi, L. , Seifert, A. , and Kneifel, S. . Evaluation of ice particle growth in icon using statistics of multi-frequency doppler cloud radar observations. *Quarterly Journal of the Royal Meteorological Society*, 146(733):3830–3849, 2020. doi:10.1002/qj.3875.

Petty, A. A. , Kurtz, N. T. , Kwok, R. , Markus, T. , and Neumann, T. A. . Winter arctic sea ice thickness from icesat-2 freeboards. *Journal of Geophysical Research: Oceans*, 125(5):e2019JC015764, 2020. doi:10.1029/2019JC015764.

Pincus, R. , Barker, H. W. , and Morcrette, J.-J. . A fast, flexible, approximate technique for computing radiative transfer in inhomogeneous cloud fields. *Journal of Geophysical Research: Atmospheres*, 108(D13), 2003. doi:10.1029/2002JD003322.

Pithan, F. , Svensson, G. , Caballero, R. , Chechin, D. , Cronin, T. W. , Ekman, A. M. , Neggers, R. , Shupe, M. D. , Solomon, A. , Tjernström, M. , et al. Role of air-mass transformations in exchange between the Arctic and mid-latitudes. *Nature Geoscience*, 11(11):805–812, 2018. doi:10.1038/s41561-018-0234-1.

Prein, A. F. , Langhans, W. , Fosser, G. , Ferrone, A. , Ban, N. , Goergen, K. , Keller, M. , Tölle, M. , Gutjahr, O. , Feser, F. , et al. A review on regional convection-permitting climate modeling: Demonstrations, prospects, and challenges. *Reviews of Geophysics*, 53(2):323–361, 2015. doi:10.1002/2014RG000475.

Prill, F. , Reinert, D. , Rieger, D. , and Zängl, G. . *ICON Tutorial - Working with the ICON Model*, 2020. URL `https://www.dwd.de/DE/leistungen/nwv_icon_tutorial/pdf_einzelbaende/icon_tutorial2020.html`.

Rabe, B. , Heuzé, C. , Regnery, J. , Aksenov, Y. , Allerholt, J. , Athanase, M. , Bai, Y. , Basque, C. , Bauch, D. , Baumann, T. M. , et al. Overview of the MOSAiC expedition: Physical oceanography. *Elementa: Science of the Anthropocene*, 10(1), 2022. doi:10.1525/elementa.2021.00062.

Raschendorfer, M. . The new turbulence parameterization of LM. Technical report, 2001. URL `https://www.cosmo-model.org/content/model/documentation/newsLetters/newsLetter01/newsLetter_01.pdf`.

Rauterkus, R. and Maronga, B. . Large-eddy simulations analyzing the impact of rv polarstern on surrounding measurements during mosaic. 2023. doi:10.5194/egusphere-egu23-14855.

Richardson, H. , Basu, S. , and Holtslag, A. . Improving stable boundary-layer height estimation using a stability-dependent critical bulk richardson number. *Boundary-layer meteorology*, 148(1):93–109, 2013. doi:10.1007/s10546-013-9812-3.

Rieger, D. , Köhler, M. , Hogan, R. J. , Schäfer, S. A. K. , Seifert, A. , de Lozar, A. , and Zängl, G. . ecRad in ICON - Implementation Overview. *Reports on ICON*, 2019. doi:10.5676/DWD.

Rinke, A. , Dethloff, K. , Cassano, J. J. , Christensen, J. , Curry, J. A. , Du, P. , Girard, E. , Haugen, J.-E. , Jacob, D. , Jones, C. , et al. Evaluation of an ensemble of Arctic regional climate models: spatiotemporal fields during the SHEBA year. *Climate dynamics*, 26(5):459–472, 2006. doi:10.1007/s00382-005-0095-3.

Rinke, A. , Ma, Y. , Bian, L. , Xin, Y. , Dethloff, K. , Persson, P. O. G. , Lüpkes, C. , and Xiao, C. . Evaluation of atmospheric boundary layer-surface process relationships in a regional climate model along an East Antarctic traverse. *Journal of Geophysical Research: Atmospheres*, 117(D9), 2012. doi:10.1029/2011JD016441.

Rinke, A. , Cassano, J. J. , Cassano, E. N. , Jaiser, R. , and Handorf, D. . Meteorological conditions during the MOSAiC expedition: Normal or anomalous? *Elem Sci Anth*, 9 (1):00023, 2021. doi:10.1525/elementa.2021.00023.

Rotta, J. . Beitrag zur Berechnung der turbulenten Grenzschichten. *Ingenieur-Archiv*, 19 (1):31–41, 1951. doi:10.1007/BF00534668.

Ruxton, G. D. . The unequal variance t-test is an underused alternative to student's t-test and the mann–whitney u test. *Behavioral Ecology*, 17(4):688–690, 2006. doi:10.1093/beheco/ark016.

Rybka, H. . The behavior of high-cape summer convection in large-domain large-eddy simulations with icon. 2020. doi:10.5194/acp-21-4285-2021.

Schäfer, S. A. , Hogan, R. J. , Klinger, C. , Chiu, J. C. , and Mayer, B. . Representing 3-d cloud radiation effects in two-stream schemes: 1. longwave considerations and effective cloud edge length. *Journal of Geophysical Research: Atmospheres*, 121(14):8567–8582, 2016. doi:10.1002/2016JD024875.

Schär, C. , Leuenberger, D. , Fuhrer, O. , Lüthi, D. , and Girard, C. . A new terrain-following vertical coordinate formulation for atmospheric prediction models. *Monthly Weather Review*, 130(10):2459–2480, 2002. doi:10.1175/1520-0493(2002)130<2459:ANTFVC>2.0.CO;2.

Schemann, V. , Ebell, K. , Pospichal, B. , Neggers, R. , Moseley, C. , and Stevens, B. . Linking Large-Eddy Simulations to Local Cloud Observations. *Journal of Advances in Modeling Earth Systems*, 12(12):e2020MS002209, 2020. doi:10.1029/2020MS002209.

Schneider, T. , Lüpkes, C. , Dorn, W. , Chechin, D. , Handorf, D. , Khosravi, S. , Gryanik, V. M. , Makhotina, I. , and Rinke, A. . Sensitivity to changes in the surface-layer turbulence parameterization for stable conditions in winter: A case study with a regional climate model over the Arctic. *Atmospheric Science Letters*, page e1066, 2021. doi:10.1002/asl.1066.

Schnierstein, N. , Chylik, J. , and Neggers, R. . Impacts of arctic leads on clouds and humidity inversions in large-eddy simulations constrained by mosaic data. In *AGU Fall Meeting Abstracts*, volume 2021, pages C55C–0602, 2021. doi:2021AGUFM.C55C0602S.

Seifert, A. . A revised cloud microphysical parameterization for cosmo-lme. *COSMO News Letter*, (7):25–28, 2008. URL `https://www.cosmo-model.org/content/model/documentation/newsLetters/newsLetter07/cnl7_seifert.pdf`.

Seifert, A. and Beheng, K. D. . A two-moment cloud microphysics parameterization for mixed-phase clouds. part 1: Model description. *Meteorology and atmospheric physics*, 92(1):45–66, 2006. doi:10.1007/s00703-005-0112-4.

Serreze, M. , Barrett, A. , Stroeve, J. , Kindig, D. , and Holland, M. . The emergence of surface-based Arctic amplification. *The Cryosphere*, 3(1):11–19, 2009. doi:10.5194/tc-3-11-2009.

Serreze, M. C. and Barry, R. G. . Processes and impacts of Arctic amplification: A research synthesis. *Global and planetary change*, 77(1-2):85–96, 2011. doi:10.3402/tellusa.v64i0.17330@zela20.2016.68.issue-s1.

Shonk, J. K. and Hogan, R. J. . Tripleclouds: An efficient method for representing horizontal cloud inhomogeneity in 1d radiation schemes by using three regions at each height. *Journal of Climate*, 21(11):2352–2370, 2008. doi:10.1175/2007JCLI1940.1.

Shupe, M. , Rex, M. , Dethloff, K. , Damm, E. , Fong, A. , Gradinger, R. , Heuzé, C. , Loose, B. , Makarov, A. , Maslowski, W. , Nicolaus, W. , Perovich, M. , Rabe, B. , Rinke, A. , Sokolov, A. , and Sommerfeld, A. . Arctic report card: The MOSAiC expedition: A year drifting with the Arctic sea ice. 2020. doi:10.25923/9g3v-xh92.

Shupe, M. , Rex, M. , Blomquist, B. , Persson, P. , Schmale, J. , Uttal, T. , Althausen, D. , Angot, H. , Archer, S. , Bariteau, L. , Beck, I. , Bilberry, J. , Bucci, S. , Buck, C. , Boyer, M. , Brasseur, Z. , Brooks, I. , Calmer, R. , Cassano, J. , Castro, V. , Chu, D. , Costa, D. , Cox, C. , Creamean, J. , Crewell, S. , Dahlke, S. , Damm, E. , de Boer, G. , Deckelmann, H. , Dethloff, K. , Dütsch, M. , Ebell, K. , Ehrlich, A. , Ellis, J. , Engelmann, R. , Fong, A. , Frey, M. , Gallagher, M. , Ganzeveld, L. , Gradinger, R. , Graeser, J. , Greenamyer, V. , Griesche, H. , Griffiths, S. , Hamilton, J. , Heinemann, G. , Helmig, D. , Herber, A. , Heuzé, C. , Hofer, J. , Houchens, T. , Howard, D. , Inoue, J. , Jacobi, H.-W. , Jaiser, R. , Jokinen, T. , Jourdan, O. , Jozef, G. , King, W. , Kirchgaessner, A. , Klingebiel, M. , Krassovski, M. , Krumpen, T. , Lampert, A. , Landing, W. , Laurila, T. , Lawrence, D. , Lonardi, M. , Loose, B. , Lüpkes, C. , Maahn, M. , Macke, A. , Maslowski, W. , Marsay, C. , Maturilli, M. , Mech, M. , Morris, S. , Moser, M. , Nicolaus, M. , Ortega, P. , Osborn, J. , Pätzold, F. , Perovich, D. , Petäjä, T. , Pilz, C. , Pirazzini, R. , Posman, K. , Powers, H. , Pratt, K. , Preußer, A. , Quélever, L. , Radenz, M. , Rabe, B. , Rinke, A. , Sachs, T. , Schulz, A. , Siebert, H. , Silva, T. , Solomon, A. , Sommerfeld, A. , Spreen, G. , Stephens, M. , Stohl, A. , Svensson, G. , Uin, J. , Viegas, J. , Voigt, P. , C von der Gathen, Wehner, B. , Welker, J. , Wendisch, M. , Werner, M. , Xie, Z. , and Yue, F. . Overview of the MOSAiC expedition - Atmosphere. *Elem Sci Anth*, 10(1):00060, 2022. doi:10.1525/elementa.2021.00060.

Shupe, M. D. , Chu, D. , Costa, D. , Cox, C. , Creamean, J. , de Boer, G. , Dethloff, K. , Engelmann, R. , Gallagher, M. , Hunke, E. , et al. Multidisciplinary drifting observatory for the study of arctic climate (mosaic)(field campaign report). 2021. doi:10.2172/1787856.

Smagorinsky, J. . General circulation experiments with the primitive equations: I. the basic experiment. *Monthly weather review*, 91(3):99–164, 1963. doi:10.1175/1520-0493(1963)091<0099:GCEWTP>2.3.CO;2.

Sommeria, G. . Three-dimensional simulation of turbulent processes in an undisturbed trade wind boundary layer. *Journal of Atmospheric Sciences*, 33(2):216–241, 1976. doi:10.1175/1520-0469(1976)033<0216:TDSOTP>2.0.CO;2.

Sommeria, G. and Deardorff, J. . Subgrid-scale condensation in models of nonprecipitating clouds. *Journal of Atmospheric Sciences*, 34(2):344–355, 1977. doi:10.1175/1520-0469(1977)034<0344:SSCIMO>2.0.CO;2.

Sotiropoulou, G. , Sullivan, S. , Savre, J. , Lloyd, G. , Lachlan-Cope, T. , Ekman, A. M. , and Nenes, A. . The impact of secondary ice production on Arctic stratocumulus. *Atmospheric Chemistry and Physics*, 20(3):1301–1316, 2020. doi:10.5194/acp-20-1301-2020.

Spreen, G. , Kaleschke, L. , and Heygster, G. . Sea ice remote sensing using amsr-e 89-ghz channels. *Journal of Geophysical Research: Oceans*, 113(C2), 2008. doi:10.1029/2005JC003384.

Stackhouse Jr, P. W. and Stephens, G. L. . A theoretical and observational study of the radiative properties of cirrus: Results from fire 1986. *Journal of Atmospheric Sciences*, 48(18):2044–2059, 1991. doi:10.1175/1520-0469(1991)048<2044:ATAOSO>2.0.CO;2.

Student. The Probable Error of a Mean. *Biometrika*, 6(1):1–25, 1908. doi:10.2307/2331554.

Stull, R. B. . *An introduction to boundary layer meteorology*, volume 13. Springer Science & Business Media, 1988. doi:10.1007/978-94-009-3027-8.

Tetzlaff, A. , Lüpkes, C. , and Hartmann, J. . Aircraft-based observations of atmospheric boundary-layer modification over arctic leads. *Quarterly Journal of the Royal Meteorological Society*, 141(692):2839–2856, 2015. doi:10.1002/qj.2568.

Tjernström, M. , Žagar, M. , Svensson, G. , Cassano, J. J. , Pfeifer, S. , Rinke, A. , Wyser, K. , Dethloff, K. , Jones, C. , Semmler, T. , et al. Modelling the Arctic boundary layer: an evaluation of six ARCMIP regional-scale models using data from the SHEBA project. *Boundary-layer meteorology*, 117(2):337–381, 2005. doi:10.1007/s10546-004-7954-z.

Treffeisen, R. , Asseng, J. , Bartsch, A. , Bräuer, B. , Fritzsch, B. , Grosfeld, K. , Hendricks, S. , Hiller, W. , Heygster, G. , Krumpen, T. , et al. Online sea ice knowledge and data platform: www. meereisportal. de. 2015. doi:10.2312/polfor.2016.011.

Valkonen, T. , Vihma, T. , Johansson, M. , and Launiainen, J. . Atmosphere–sea ice interaction in early summer in the Antarctic: Evaluation and challenges of a regional atmospheric model. *Quarterly Journal of the Royal Meteorological Society*, 140(682): 1536–1551, 2014. doi:10.1002/qj.2237.

van der Linden, S. and Ansorge, C. . The coldest days of mosaic-an les study. In *EGU General Assembly Conference Abstracts*, pages EGU22–9646, 2022. doi:10.5194/egusphere-egu22-9646 10.5194/egusphere-egu22-9646.

Vihma, T. , Pirazzini, R. , Fer, I. , Renfrew, I. A. , Sedlar, J. , Tjernström, M. , Lüpkes, C. , Nygård, T. , Notz, D. , Weiss, J. , et al. Advances in understanding and parameterization of small-scale physical processes in the marine arctic climate system: a review. *Atmospheric Chemistry and Physics*, 14(17):9403–9450, 2014. doi:10.5194/acp-14-9403-2014.

Webster, M. , Gerland, S. , Holland, M. , Hunke, E. , Kwok, R. , Lecomte, O. , Massom, R. , Perovich, D. , and Sturm, M. . Snow in the changing sea-ice systems. *Nature Climate Change*, 8(11):946–953, 2018. doi:10.1038/s41558-018-0286-7.

Weinbrecht, S. and Raasch, S. . High-resolution simulations of the turbulent flow in the vicinity of an arctic lead. *Journal of Geophysical Research: Oceans*, 106(C11):27035–27046, 2001. doi:10.1029/2000JC000781.

Welch, B. L. . The generalization of students problem when several different population varlances are involved. *Biometrika*, 34(1-2):28–35, 1947. doi:10.1093/biomet/34.1-2.28.

Wilcox, D. C. . *Turbulence modeling for CFD. La Canada, CA: DCW Industries.* 2006.

Wilcoxon, F. . Individual Comparisons by Ranking Methods. *Biometrics Bulletin*, 1(6): 80–83, 1945. ISSN 00994987. doi:10.2307/3001968.

Wiscombe, W. . On initialization, error and flux conservation in the doubling method. *Journal of Quantitative Spectroscopy and Radiative Transfer*, 16(8):637–658, 1976. doi:10.1016/0022-4073(76)90056-X.

Zängl, G. . Operationelles NWV-System: ICON: Model configuration upgrade of ICON. Technical report, DWD, 2021a. URL `https://www.dwd.de/DE/fachnutzer/forschung_lehre/numerische_wettervorhersage/nwv_aenderungen/_functions/DownloadBox_modellaenderungen/nwv_aenderungen_icon_gesamt.html`.

Zängl, G. . Operationelles NWV-System: ICON: ICON upgrades (version 2.6.3-nwp1). Technical report, DWD, 2021b. URL `https://www.dwd.de/DE/fachnutzer/`